WIGNER CURRENT IN ONE-DIMENSIONAL BOUND-STATE SYSTEMS

Dimitris Kakofengitis

A thesis submitted to the
UNIVERSITY OF HERTFORDSHIRE
in partial fulfilment of the requirements of the degree of

Doctor of Philosophy

July 2018

School of Physics, Astronomy and Mathematics
University of Hertfordshire, Hatfield, AL10 9AB

Principal Supervisor: Dr Ole Steuernagel

Acknowledgements

I would like to acknowledge the advice and guidance of my supervisor Dr Ole Steuernagel. Since my final year project of my BSc degree in Physics, Dr Steuernagel has always been an inspiration and a person to look up to. Again as my supervisor, during my MRes degree in Physics, Dr Steuernagel managed to pull together some of the best ideas we had worked on, and in collaboration with Dr Georg Ritter, we published our first article on Wigner current, at the time incorrectly referred to as Wigner '*flow*'. This publication consequently lead to my reinstatement as a PhD student by the then Dean of the department, Professor Sean Ryan, and to the continuation of my collaboration with Dr Steuernagel.

I am also indebted to Professor Sean Ryan who was one of my lecturers during my BSc degree and he too had been an inspiration and a person to look up to, especially as the Dean of the School of Physics, Astronomy and Mathematics. Prof. Ryan kindly approved the funding for this PhD project but also continued providing me with extra teaching work throughout my MRes and PhD studies. Towards the end of my PhD, Prof. Sean provided a recommendation which helped me get a more stable position as a visiting lecturer at the same university. This meant that I could continue finishing my PhD without any financial stress.

I am also grateful to Dr Alan McCall for his involvement as the internal examiner of this PhD project and earlier during my MRes degree. Dr McCall introduced me to quantum mechanics as one of my lecturers; his enthusiasm was infectious!

I am also grateful to Dr Jim Collett, Dr Charles Young, Dr Benoit Vicedo and Maxime Oliva for their fruitful discussions and advice on certain parts of this PhD project.

From the university, I would like to also thank the current Dean of the school, Dr Mark Thompson and the Associate Dean of Research, Prof. Elias Brinks, whose support at the very end of my PhD project was invaluable.

I would like to also thank my parents who have always unreservedly believed in me, and have also provided me with all the support needed during my studies and were always there willing to help as much as they could. Σας ευχαριστώ πολύ!

Finally, I would like to thank my wife Dr Cecilia Nedi Gyansah for her continuous support and devotion.

This PhD project was funded by the School of Physics, Astronomy and Mathematics at the University of Hertfordshire.

Abstract

The behaviour of classical systems is characterised by their phase portraits; the collections of their trajectories. In quantum mechanics phase portraits are still considered impossible to compute due to the complexity of quantum trajectories arising from the introduction of the quantum correction terms. Instead, in this thesis, we identify the Wigner current (the rate of flow per unit area of the Wigner distribution), as the quantum analogue of the classical phase-space current, and through Wigner current's fieldline portraits we show that it reveals hidden features of quantum dynamics and extra complexity.

In our analysis, we focus on the simplest, most intuitive, and analytically accessible aspects of the Wigner current. We investigate its features for weakly-anharmonic weakly-excited bound-states of time-reversible one-dimensional quantum-mechanical systems. We establish that weakly-anharmonic potentials can be grouped into three distinct classes: hard, soft, and odd. We stress connections between each other and the harmonic case. We show that their Wigner current fieldline portraits can be characterised by the Wigner current's discrete stagnation points, how these arise and how a quantum system's dynamics is constrained by the stagnation points' topological charge conservation. We additionally demonstrate the conceptual power of the Wigner current by addressing some confusion found in the literature.

We also stress the usefulness of the integral form of Wigner's representation as an alternative to the popular Moyal bracket. The integral form brings out the symmetries between momentum and position representations of quantum mechanics, is numerically stable, and allows us to perform some calculations using elementary integrals instead of Groenewold star-products. The associated integral form of the Wigner current is used here in an elementary proof which shows that only systems up to quadratic in their potential fulfil Liouville's theorem of volume preservation in quantum mechanics.

Contents

Acknowledgements ii

Abstract iii

Contents iii

List of Figures vii

List of Tables vii

List of Symbols viii

1 Introduction 1
- 1.1 Wigner's vs Schrödinger's Representation . . . 1
- 1.2 A Hydrodynamical vs Current-based Approach . . . 2
- 1.3 Summary of Results . . . 3
- 1.4 Higher Dimensions . . . 4
- 1.5 The Structure of this Thesis . . . 5

2 Classical Phase-Space 6
- 2.1 Classical Phase Portrait . . . 6
- 2.2 Classical Phase-Space Velocity Field . . . 6
- 2.3 Liouville's Theorem on Volume Preservation . . . 7
- 2.4 Hamiltonian & Lagrangian Mechanics . . . 7
- 2.5 Stagnation Point Numerology . . . 9

3 Schrödinger's Quantum Mechanics 11
- 3.1 Wave-Particle Duality . . . 11
- 3.2 Wave Functions . . . 11
  - 3.2.1 Two-State Superpositions . . . 12
  - 3.2.2 Schrödinger Equations . . . 13
- 3.3 Probability Distributions . . . 14
  - 3.3.1 Probability Currents . . . 15
- 3.4 The Hydrodynamic Formulation . . . 16
- 3.5 The Rabi Cycle . . . 17
- 3.6 Bound-States . . . 19
  - 3.6.1 Bound-State Spectrum . . . 19

4 Wigner's Quantum Mechanics **24**
4.1 The Wigner Distribution . . . 24
4.1.1 Mathematical Properties of the Wigner Distribution . . . 25
4.1.2 The Wigner Distribution of a Two-State Superposition . . . 27
4.2 The Time Evolution of the Wigner Distribution . . . 27
4.2.1 Wigner Equation . . . 27
4.2.2 Moyal Equation . . . 28
4.3 The Wigner Current . . . 29
4.3.1 The Wigner Current of Mechanical Systems . . . 29
4.3.2 Mathematical Properties of the Wigner Current . . . 30

5 Numerical Aspects **33**
5.1 Numerical Computation of the Wigner Function . . . 33
5.2 Numerical Computation of the Wigner Current . . . 33
5.3 Consistency Checks . . . 34

6 When is Wigner's Current Liouvillian? **36**
6.1 Wigner Current's Velocity Field . . . 36
6.2 Liouvillian Wigner Current . . . 37
6.3 Liouvillian Wigner Current for Eigenfunctions . . . 38

7 Degenerate Wigner Current **42**
7.1 The Quantum Harmonic Oscillator . . . 42
7.2 The Quantum Harmonic Oscillator in Phase-Space . . . 42
7.3 The Quantum Harmonic Oscillator's Dynamics in Phase-Space . . . 46

8 Semi-Degenerate Wigner Current **48**
8.1 The Non-Linear Kerr Oscillator . . . 48
8.2 The Non-Linear Kerr Oscillator in Phase-Space . . . 48
8.3 The Non-Linear Kerr Oscillator's Dynamics in Phase Space . . . 49

9 Non-Degenerate Wigner Current **51**
9.1 Three Classes of Weakly Anharmonic Potentials . . . 51
9.2 The Wigner Functions of the Morse Potential . . . 53
9.3 Wigner Current Fieldine Portraits for Eigenfunctions . . . 54
9.4 Wigner Current Fieldine Portraits for Two-State Superpositions . . . 59

10 Conclusions and Future Work **69**
10.1 Contributions to knowledge . . . 69
10.2 Future Work . . . 70

A Functions **72**

B Published Work **74**

Index **80**

List of Figures

2.1 Potentials and their corresponding classical phase portraits 9
2.2 Characterisation of the stagnation points of phase-space 10

3.1 Time evolution of the probability of a Rabi state being found in the ground and first-excited states after measurement 18

5.1 Incorrect Wigner current fieldline portraits observed using the infinite-sum form of $\boldsymbol{J}$ 34

6.1 Divergence of Wigner current's velocity field 40

7.1 Wigner functions of the eigenfunctions of the quantum harmonic oscillator and an illustration of the trend of their zero circles Radii 44
7.2 Wigner functions of the superposition of the ground and first excited state of the quantum harmonic oscillator 45
7.3 Wigner current fieldline portraits for the quantum harmonic oscillator 47

8.1 Divergence of Wigner current's velocity field for the Kerr oscillator 50

9.1 Representatives of the three classes of weakly-anharmonic potentials and associated classical phase portraits 52
9.2 Qualitative discussion of the emergence of the Wigner current stagnation points for the first excited state of a hard potential 57
9.3 Wigner current fieldline portraits of the first and second excited states 58
9.4 Time-dependent quantum displacement of the Morse potential minimum's stagnation point along the x-axis 60
9.5 Combined Wigner current fieldline portraits for the superposition state $\Psi_{0,1}(t;\theta)$ of the Eckart, Rosen-Morse and Morse potentials 61
9.6 Wigner current fieldline portraits for the superposition state $\Psi_{0,1}(t;\theta)$ of the Eckart potential 62
9.7 Wigner current fieldline portraits for the superposition state $\Psi_{0,1}(t;\theta)$ of the Rosen-Morse potential 63
9.8 Wigner current fieldline portraits for the superposition state $\Psi_{0,1}(t;\theta)$ of the Morse potential 64
9.9 Time evolution of the Wigner current stagnation points of the superposition state $\Psi_{0,1}(\frac{\pi}{4}\cdot 0.95)$ in Eq. (3.8) 66
9.10 Rabi cycle for state (9.11) with frequency ratio $\Omega_R/\Omega^{\odot} = 1/8$. 67
9.11 Conservation of the Wigner current winding number 68
9.12 Wigner current fieldline portraits for state $\Psi_{1,2}\left(x, \frac{3T}{4}; \frac{\pi}{4}\right)$ 68

List of Tables

3.1 Shape-invariant potentials 23

7.1 Radii of the zero circles of the quantum harmonic oscillator's Wigner functions for the first, second and third excited states 43

9.1 Revised version of Table 3.1 53

A.1 Vector calculus identities in 2D phase space 73

List of Symbols

x	Position axis/variable	6
p	Momentum axis/variable	6
M	Particle mass	7
h	Planck's constant	11
$\hbar$	Planck's constant rescaled	11
H_n	Hermite polynomials	42
$L_m^{(n-m)}$	Laguerre polynomials	42
$\mathcal{L}$	A closed loop in phase-space	10
$\boldsymbol{j}$	Classical phase-space current	7
$\jmath$	Probability current in position space	15
$\tilde{\jmath}$	Probability current in momentum space	16
$\boldsymbol{J}$	Wigner current (quantum phase-space current; two-dimensional vector field)	29
δ	Dirac delta function	72
δ_{mn}	Kronecker delta	72
$\mathcal{H}$	Classical Hamiltonian	7
$\hat{\mathcal{H}}$	Hamiltonian operator	13
$\hat{\mathcal{H}}_R$	Hamiltonian of the Rabi cycle	17
$\hat{\mathcal{H}}^{\odot}$	Quantum harmonic oscillator's Hamiltonian	42
$\hat{\mathcal{H}}^{\mathcal{K}}$	Non-linear Kerr oscillator's Hamiltonian	48
$\mathcal{J}$	The Jacobian, used in a change of variables	72
V	Position space potential	14
$\tilde{V}$	Momentum space potential	14
$V^{\mathcal{A}}$	Anharmonic potential	51

$V_\nu^{\mathcal{A}}$	Truncated anharmonic potential	51
$V^{\mathcal{E}}$	Eckart potential; hard representative	52
$V^{\mathcal{R}}$	Rosen-Morse potential; soft representative	52
$V^{\mathcal{M}}$	Morse potential; odd representative	52
D	Inverse anharmonicity parameter	53
ρ	Classical probability distribution	6
W	Wigner distribution; quasi-probability distribution in phase space	24
W_{mn}	Wigner distribution terms of a two-state superposition	27
$W_{m,n}$	Wigner distribution of a two-state superposition	27
$W^{\odot}$	Quantum harmonic oscillator's Wigner function	42
P	Position probability distribution	11
$\tilde{P}$	Momentum probability distribution	11
Ψ	Position space wave function	11
$\tilde{\Psi}$	Momentum space wave function	11
$\Psi_{m,n}$	Two-state superposition	12
m, n	State indices	12
Ψ_R	Rabi state	17
E	Eigenenergy of an eigenfunction ψ	12
θ	Two-state superposition weighting angle	12
φ	Phase shift parameter	12
ΔE	Energy difference	12
T	Time period; the time it takes to complete one oscillation	12
T_R	Rabi cycle time period	18
$A^\dagger$	Creation operator	20
A	Annihilation operator	20
χ	Superpotential	20
$\mathcal{N}$	Normalisation constant	20
$\boldsymbol{A}$	Vector potential	7
$\boldsymbol{u}$	Classical phase-space velocity field	6
$\boldsymbol{w}$	Wigner current velocity field	36

"*Quantum mechanics lives and works in phase-space*"
—C. K. Zachos, Int. J. Mod. Phys. A **17**, 297 (2002).

1 Introduction

In this thesis we investigate quantum dynamics in phase-space through Wigner's representation of quantum mechanics, named after Eugene Wigner who introduced it in 1932 [1]. We use Wigner's current, also known as phase-space *flux* [2], and at times incorrectly referred to as Wigner '*flow*' [3, 4]. The term *flow* refers to the motion of, for example a fluid, whereas here we focus on the current: the *rate of flow per unit area* of the fluid. Consider this fluid to be a probability distribution. Its associated current is called the probability current. In quantum mechanics, the position and momentum probability distributions combine in phase-space to form the Wigner distribution. Its associated current is called the Wigner current. Thus, the Wigner current is the phase-space counterpart of the quantum-mechanical probability currents [5]. But the Wigner distribution is not a probability distribution in its strict mathematical sense, as it can assume negative values. Nevertheless it is a distribution function and it is the *"closest quantum analogue of the classical phase-space distribution"* [6]. Thus, Wigner's current is the closest quantum analogue of the classical phase-space current.

This alternative approach of investigating quantum dynamics through Wigner's representation, is still at the early stages of its potential and it is highly understudied. This is partly due to the great success of the path integral formulation, even though, historically speaking, Wigner's representation preceded the path integral formulation. Also, Wigner's representation, in its early formulations, had great opponents, like Paul Dirac (Wigner's brother-in-law), who had reservations about Moyal's methods [7], and was against the formulation of quantum mechanics in phase-space, due to the uncertainty principle [8]. Dirac in the end was wrong: the uncertainty principle does not preclude the existence of quantum mechanics in phase-space. In the words of Cosmas K. Zachos: "*In this logically complete and self-standing formulation, one need not choose sides — coordinate or momentum space. It works in full phase-space, accommodating the uncertainty principle*" [9]. "*Some believe it will supplant, or at least complement, the other methods in quantum mechanics and quantum field theory*"[10].

We would like to mention that Moyal worked on quantum phase-space during the 1940s, though most certainly during his spare time, as he was employed by the De Havilland Aircraft Company at Hatfield, Hertfordshire, UK, for his "*wartime research centred on electronic instrumentation and different continuous systems and their electrical analogues*" [7]. We are proud to also have worked on quantum phase-space under the same 'roof'.

Next, we discuss the motivational and historical background to the study of quantum dynamics in *phase-space*, and of our alternative approach. First we highlight the benefits of Wigner's representation against the more traditional Schrödinger's representation, in Section 1.1. Later, in Section 1.2, we compare the hydrodynamical to the current-based approach of investigating quantum mechanics. Finally, in Section 1.3, we discuss our choice of systems under consideration, and provide a summary of results. The structure of the remaining part of this thesis is outlined in Section 1.5.

1.1 Wigner's vs Schrödinger's Representation

A pure state of a quantum mechanical system is represented by a state vector or density matrix in Hilbert space. A mixed state (an ensemble of pure states) is represented as a density matrix [11]. Choosing a basis, for example position or momentum, a pure state is represented

by its wave function. The continuity equation describing the dynamics of the wave function is known as Schrödinger's equation, represented in either position or momentum space.

Choosing phase-space as the basis, both position and momentum are represented as variables, simultaneously, avoiding position and momentum operators. In phase-space, the state of the quantum system is represented by the Wigner distribution [1] (the Wigner-transform of its density matrix). The Wigner distribution *combines* in phase-space the position and momentum quantum-mechanical probability distributions, but since it can assume negative values, it is not a probability distribution. It is therefore referred to as a *quasi*-probability distribution. The continuity equation which describes the dynamics of the Wigner distribution is called the quantum Liouville or Wigner equation [1] (the Wigner-transform of the von Neumann equation). Thus, Wigner's representation applies to pure and mixed states.

The quantum Liouville equation can be resolved into kinetic and potential energy terms, giving rise to Wigner's current. This is generally true when the system under consideration has a Hamiltonian expressed as a sum of kinetic and potential energies. But for quantum systems with different Hamiltonians, for example field oscillators, like the non-linear Kerr oscillator (studied in this thesis), the quantum Liouville equation is expressed in terms of the Moyal bracket (the quantum analogue of the Poisson bracket), named after José Moyal who introduced it in 1949 [12]. For such cases, extracting the Wigner current components is non-trivial and requires a certain knowledge of the symmetries of the system. For example, it is well-known that the solutions to the eigenstates of the Kerr oscillator are the eigenstate solutions of the harmonic oscillator. Thus, the dynamics and therefore the Wigner current of the Kerr oscillator must obey similar symmetries to the harmonic oscillator.

Due to Moyal's work, the quantum Liouville equation is sometimes referred to as Moyal's equation. Its integral form was derived by George Baker in 1958 [13].

For systems governed by the classical equations of motion, such as Harmonic systems and their isomorphic partners [14] (including forced systems, and systems studied at the classical limit of $\hbar \to 0$), the quantum-mechanical phase-space formulation provides a simpler and, in this sense, even superior approach for their study of quantum dynamics compared to the standard Schrödinger wave function propagators [15], making it easier to compare quantum and classical mechanics [16].

1.2 A Hydrodynamical vs Current-based Approach

The ideas of a pilot wave theory presented by Louis De Broglie in 1927 [17] lead to the hydrodynamic formulation of quantum mechanics, also referred to as quantum hydrodynamics [18], since it resembles classical hydrodynamics. Quantum hydrodynamics was developed by Erwin Madelung in 1927 [19], and independently (following De Broglie's pilot wave theory), by David Bohm in 1952 [20, 21]. Madelung's and Bohm's quantum hydrodynamic formulations are mathematically equivalent, but Bohm's theory was more in line with De Broglie's pilot wave theory and thus it is now known as De Broglie-Bohm theory. It predicts the existence of quantum trajectories in position space. Their existence arises from the particle nature, whereas, the wave nature of the quantum system is depicted by Schrödinger's representation. As it is postulated by the pilot wave theory, the quantum particle is guided by its wave function. The path traced by the quantum particle, is its quantum trajectory.

Mathematically, Schrödinger's and Bohm's (and Madelung's) representations are equivalent and so the existence of quantum trajectories *cannot* be disputed as long as quantum mechanics is considered to be a valid theory. But rather, it is the interpretation of the quan-

tum trajectories which is in dispute and has puzzled physicists since their formulation. For example, it is believed that they were "*originally introduced with the aim of arriving at a 'realistic interpretation' of quantum theory*" [22]. Instead, one can think of the quantum trajectories as the *set of possible* paths that the quantum particle can follow. This is similar to the idea of the *set of possible* eigenvalues of an operator, e.g. the momentum operator [23]. In fact, the quantum force associated with the trajectory of the quantum particle, is the total derivative of the momentum eigenvalues [19, 20].

Although quantum trajectories do have experimental significance [24], they are considered surreal [22] due to the uncertainty principle, as one cannot *simultaneously measure* the exact position and momentum of a quantum particle [25].

The quantum hydrodynamic equations were also derived through Wigner's representation by Takabayasi in 1954 [15], and it was later shown that the De Broglie-Bohm theory is the projection of Wigner's representation onto position space [26]. Quantum trajectories have therefore also been developed in phase-space. They are of great interest in theoretical chemistry since the complexity of chemical systems forces us to find simplifications to make calculations of quantum dynamics tractable. But since the quantum phase-space velocity field, and its divergence, depend on the reciprocal of the density (the Wigner distribution) of the system, they are rendered useless as they can be singular for anharmonic systems at the zero lines of the density. Thus, quantum trajectories in phase-space cannot be defined globally, with the exception of harmonic systems [5, 27]. Efforts to overcome these singularities and analyse quantum phase-space through a trajectory-based description, have mainly been focused on semi-classical approximations [28–36], which are employed to avoid the generation of negativities of the Wigner distribution. Attempts to avoid negativities also include the use of the Husimi distribution (which is a smoothed Wigner distribution, and is everywhere positive), but then numerical and computational issues arise [37].

In this thesis, we multiply the quantum phase-space velocity field with its density, giving rise to the Wigner current. Unlike its velocity field, the Wigner current is non-singular and has a finite divergence, allowing us to carry out computational modelling of the dynamics of the system more accurately and robustly. Instead of developing quantum trajectories in phase-space, in this thesis we depict the instantaneous portraits of Wigner current's fieldlines (similar to phase-space portraits) and through their time-evolution we analyse the dynamics of quantum systems.

1.3 Summary of Results

In our attempt to investigate quantum tunnelling in phase-space using the Wigner distribution of an asymmetric double-well potential [38], we came across Wigner's current. We were intrigued by the new and interesting insights into quantum dynamics offered by the Wigner current. Even though for anharmonic potentials the Wigner current does not obey Liouville's theorem [5], we were able to demonstrate that its topological charge (the Poincaré-Hopf *index* of its stagnation points) is conserved. We also demonstrated that, just like the marginal projections of the Wigner distribution are the quantum-mechanical probability distributions, equivalently, the marginal projections of Wigner current's components are the quantum-mechanical probability currents [4].

In this thesis, we present additional symmetries and projections of the Wigner current components. We also investigate Wigner's current through anharmonic potentials, such as the Eckart, Rosen-Morse and Morse potentials [39]. The Morse potential has theoretical

significance to chemistry as it is a convenient potential energy model of a diatomic molecule. Here we focus on the simplest, most intuitive, and analytically accessible aspects of the Wigner current. This was done by utilising weakly-anharmonic weakly-excited bound-states of time-reversible one-dimensional quantum-mechanical systems. We consider eigenstates and their pure two-state superpositions, rendering the dynamics periodic. The main result of this work is that Wigner current's fieldline portraits of weakly-anharmonic potentials can be grouped into three distinct classes: hard (Eckart), soft (Rosen-Morse), and odd (Morse), which are benchmarked against the harmonic oscillator. It is shown that these three classes of weakly anharmonic potentials distort Wigner current's features in characteristic fashions. From the perspective of Wigner current's fieldline portraits and stagnation points, the odd (Morse) can be represented as a hybrid of both the hard (Eckart) and soft (Rosen-Morse). Additionally, through these fieldline portraits it is also shown that there cannot be a smooth transition between classically governed and quantum phase-space dynamics of anharmonic systems.

We also stress the usefulness of the integral form of Wigner's representation as an alternative to the popular Moyal bracket [12]. The integral form brings out the symmetries between momentum and position representations of quantum mechanics, is numerically stable, and allows us to perform some calculations using elementary integrals instead of Groenewold star-products [40]. The associated integral form of the Wigner current is used in an elementary proof which shows that only systems up to quadratic in their potential, are able fulfil Liouville's theorem of volume preservation in quantum mechanics [5]. Contrary to a recent suggestion [41], this proof shows that the non-Liouvillian nature of quantum phase-space dynamics, cannot be transformed away.

Wigner's current can provide a more intuitive approach for the study of quantum dynamics and a more accessible comparison tool between quantum and classical mechanics. This is demonstrated through Ehrenfest's theorem, which is one of the many (but arguably one of the best) examples of the correspondence principle between quantum and classical mechanics. In this thesis, it is shown that the average velocity and average force, which are part of Ehrenfest's theorem, are the average (*overall phase-space*) of Wigner current's components [5]. Being able to reformulate Ehrenfest's theorem using Wigner's current, in this simpler and mathematically more intuitive way, than it is currently taught, it is a testimony to the growing idea that "*quantum mechanics lives and works in phase-space*" [9].

1.4 Higher Dimensions

In this thesis our investigation is limited to one-dimensional (one-degree of freedom) systems. Thus, we are able to visualise Wigner current's fieldline portraits in a two-dimensional phase-space. For higher degrees of freedom, say for two-dimensions, this requires a four-dimensional phase-space, which is harder to visualise.

In order to represent a system in n-dimensions (n-degrees of freedom), the system requires at least n-constants of motion and the Poisson bracket of their pairs must also vanish. Such a system is referred to as an integrable system. If a system is non-integrable, it cannot be expressed in more than one dimensions. These systems are usually referred to as chaotic or irregular [42]. In this thesis, our systems under consideration are not chaotic, they are either harmonic or anharmonic.

To construct the eigenfunctions of the systems under consideration in this thesis, we make use of supersymmetric quantum mechanics, which utilises an integrability condition, the shape invariance condition [43, 44]. Furthermore, we focus on conservative systems (apart from

the Rabi oscillations) with time-independent potentials. This implies conservation of energy. Thus, the energy is a constant of motion. To express our findings in this thesis, to say three dimensions, one needs to determine at least two more constants of motion and together with the energy of the system, the Poisson bracket of their pairs must also vanish.

1.5 The Structure of this Thesis

Classical phase-space is discussed in Chapter 2. Schrödinger's quantum mechanics is discussed in Chapter 3. Wigner's quantum mechanics, the quantum analogue of classical phase-space is discussed in Chapter 4. The numerical aspects of this research project are discussed in Chapter 5. In Chapter 6 we investigate when Wigner's current (introduced in Section 4.3) obeys Liouville's theorem. The degenerate form of the Wigner current of the quantum harmonic oscillator is discussed in Chapter 7. The semi-degenerate Wigner current of the Kerr oscillator is discussed in Chapter 8 and the non-degenerate Wigner current of weakly anharmonic potentials is discussed in Chapter 9. We conclude in Chapter 10 where we also provide a list of contributions to knowledge achieved in this research project and an outlook for future work. Finally, Appendix A provides a list of useful functions which were used in the derivation of some of the formulae in the main text, and Appendix B provides a list of our published work.

2 Classical Phase-Space

Classical phase-space was developed in the late 19th century [45]. It consists of all possible states of a classical system with unique position and momentum coordinates. The time evolution of the system generates sharply defined and non-crossing classical phase-space trajectories allowing the viewer to characterise the system's dynamics. The collection of all the classical system's trajectories, its phase portrait, is ordered by the fact that the dynamics obey Liouville's theorem (on phase-space volume preservation), and can be analysed with powerful mathematical techniques [42, 45, 46].

This chapter provides an overview of these techniques for the analysis and visualisation of a system's classical phase-space, starting with the definition of the classical phase portrait in Section 2.1 and its associated velocity field in Section 2.2. The discussion is also extended to Liouville's theorem in Section 2.3. Finally, Section 2.5 introduces stagnation point numerology for the classification of the stagnation points formed in a phase portrait used later in this thesis.

The ideas discussed in this Chapter, do not fully carry over to quantum mechanics, since Heisenberg's uncertainty principle [25] precludes the existence of a sharply defined quantum phase-space trajectory (see Chapter 4).

2.1 Classical Phase Portrait

One-dimensional phase-space is represented by a *phase plane*; a coordinate plane with axes the position x and momentum p. A unique point with coordinates $\boldsymbol{r} = \begin{pmatrix} x \\ p \end{pmatrix}$ in this phase plane, represents the state of a classical system. The evolution of the state over time t, the state's *trajectory*, has a specific set of phase plane coordinates $\{(x(t), p(t)) \ \forall \ t\}$. For each coordinate $\boldsymbol{r}$, the state of the system has an associated *velocity field* $\boldsymbol{u} = \begin{pmatrix} \dot{x}(t) \\ \dot{p}(t) \end{pmatrix}$ [1] (discussed in Section 2.2, its quantum analogue is discussed in Chapter 4), which is tangent to the trajectory. The set of all trajectories is referred to as the *phase portrait* of the system, see Figs. 2.1 and 9.1. Hereinafter, reference to the time-dependence of x and p, is dropped.

2.2 Classical Phase-Space Velocity Field

As mentioned in Section 2.1, a unique point with coordinates $\boldsymbol{r} = (x, p)$ in the phase plane, represents the state of the classical system. The evolution of the state over time t, the state's trajectory, has an associated velocity field $\boldsymbol{u} = \begin{pmatrix} \dot{x} \\ \dot{p} \end{pmatrix}$, tangent to the trajectory. Starting with the definition of the total derivative of a classical probability distribution, this Section presents the time evolution of a conservative classical system and its phase-space velocity field $\boldsymbol{u}$.

The *total derivative*[2] of a probability distribution ρ of a conservative classical system, is

$$\frac{D\rho}{Dt} \equiv \frac{\partial \rho}{\partial t} + \boldsymbol{u} \cdot \boldsymbol{\nabla} \rho = -\rho \boldsymbol{\nabla} \cdot \boldsymbol{u} = 0 \ , \tag{2.1}$$

[1] The dot on top of a letter, such as, $\dot{x}$ and $\dot{p}$, implies the time derivative of x and p, respectively.

[2] Also known as the derivative following the motion, comoving, material, convective, advective, substantive, substantial, Lagrangian, Stokes, particle, and hydrodynamic derivative.

where we made use of the conservation equation of the probability distribution (note that $\boldsymbol{j} = \rho\boldsymbol{u}$ is the associated classical phase-space current),

$$\frac{\partial\rho}{\partial t} + \boldsymbol{\nabla}\cdot\boldsymbol{j} = \frac{\partial\rho}{\partial t} + \boldsymbol{u}\cdot\boldsymbol{\nabla}\rho + \rho\boldsymbol{\nabla}\cdot\boldsymbol{u} = 0\,. \tag{2.2}$$

The dynamics of the system are represented by the velocity field $\boldsymbol{u}$,

$$\boldsymbol{u} = \frac{\boldsymbol{j}}{\rho} = \begin{pmatrix}\dot{x}\\ \dot{p}\end{pmatrix} = \begin{pmatrix}\frac{\partial\mathcal{H}}{\partial p}\\ -\frac{\partial\mathcal{H}}{\partial x}\end{pmatrix} = \begin{pmatrix}\frac{p}{M}\\ -\frac{dV(x)}{dx}\end{pmatrix}\,,\ \text{with}\ \mathcal{H} = \frac{p^2}{2M} + V(x)\,, \tag{2.3}$$

where $\mathcal{H}$ is the classical Hamiltonian with particle mass M representing the total energy of the system. The contour lines of a plot of $\mathcal{H}$ in x and p, are the corresponding classical phase-space trajectories of the system. They represent the motion of a particle moving in one-dimension x, under the influence of, in our case, a static potential $V(x)$. Therefore, classical phase-space trajectories in conservative classical systems do not cross and are fixed; lineation in phase-space, see Figs. 2.1 and 9.1. In Eq. (2.3), $\dot{x} = \frac{\partial\mathcal{H}}{\partial p} = \frac{p}{M}$ and $\dot{p} = -\frac{\partial\mathcal{H}}{\partial x} = -\frac{dV(x)}{dx}$, are referred to as Hamilton's equations of motion, where $\dot{x}$ and $\dot{p}$ are recognised as the velocity and the force (from Newtonian mechanics), respectively, that the particle in the system is subject to.

2.3 Liouville's Theorem on Volume Preservation

As mentioned in Section 2.2, for a conservative classical system, the total derivative of its probability distribution ρ is zero, see Eq. (2.1). This implies that the system's state density remains unchanged as the system evolves in time [45]. In other words, an area of a system's classical phase portrait, remains constant as the system evolves in time. This is known as Liouville's theorem. Thus, assuming ρ is non-zero, the classical phase-space velocity field $\boldsymbol{u}$ must be divergence-free and it is since $\boldsymbol{\nabla}\cdot\boldsymbol{u} = \partial_x\left(\frac{p}{M}\right) - \partial_p\left(\frac{dV(x)}{dx}\right) = 0$, implying that $\boldsymbol{u}$ is incompressible. For the systems under consideration in this thesis, the incompressibility condition precludes the formation of sinks and sources in phase-space when visualising the fieldlines of $\boldsymbol{u}$. A velocity field with zero divergence, can also be written as the curl of a vector potential $\boldsymbol{A}$ [47]. Thus, $\boldsymbol{u} = \boldsymbol{\nabla}\times\boldsymbol{A}$ given that $\boldsymbol{\nabla}\cdot\boldsymbol{u} = 0$, and since $\boldsymbol{u}$ is a two-dimensional vector field, $\boldsymbol{A}$ is a vector perpendicular to $\boldsymbol{u}$. For classical phase-space $\boldsymbol{A}$ takes the form,

$$\boldsymbol{A} = \begin{pmatrix}0\\0\\\mathcal{H}\end{pmatrix}\ \text{since}\ \boldsymbol{u} = \begin{pmatrix}\frac{p}{M}\\ -\frac{dV(x)}{dx}\\0\end{pmatrix} = \boldsymbol{\nabla}\times\boldsymbol{A} = \begin{pmatrix}\partial_p\mathcal{H}\\ -\partial_x\mathcal{H}\\0\end{pmatrix}\,, \tag{2.4}$$

where $\mathcal{H}$ is given in Eq. (2.3). In Chapter 6, it will be shown that the quantum analogue of the classical phase-space velocity field, can be written as the curl of $\boldsymbol{A}$ in Eq. (2.4) only in special cases, namely in the absence of the quantum correction terms.

2.4 Hamiltonian & Lagrangian Mechanics

As already discussed, in conservative one-dimensional classical-mechanical systems, the energy of the system, its Hamiltonian $\mathcal{H}$, is the sum of kinetic and potential energies, as in Eq. (2.3).

For time-independent potentials, $\mathcal{H}$ does not explicitly depend on time t, i.e. $\partial_t\mathcal{H} = 0$. But $\mathcal{H}$ is implicitly time-dependent through its velocity field $\boldsymbol{u}$ defined in Eq. (2.4). The total

time derivative of $\mathcal{H}$ then takes the form,

$$\frac{d\mathcal{H}}{dt} = \partial_t \mathcal{H} + \boldsymbol{u} \cdot \nabla \mathcal{H} = -\mathcal{H} \nabla \cdot \boldsymbol{u} \,, \tag{2.5}$$

which vanishes ($\frac{dH}{dt} = 0$) in conservative systems with time-independent potentials, as the energy of the system is a constant of motion.

Alternatively, the implicit time-dependence of the Hamiltonian $\mathcal{H}$ can be demonstrated as follows. The force of the system can be derived starting from the velocity of the system ($\dot{x} = p/M = \partial_p \mathcal{H}$), where the momentum p can be written in terms of the Hamiltonian $\mathcal{H}$ and potential V, as

$$p = M\dot{x} = \pm\sqrt{2M(\mathcal{H} - V)} \,. \tag{2.6}$$

Differentiating p in Eq. (2.6) with respect to t, (where $\frac{dV}{dt} = \frac{dV}{dx}\dot{x}$),

$$\dot{p} = \mp \frac{dV}{dt} \sqrt{\frac{M}{2(\mathcal{H} - V)}} = -\frac{dV}{dx} = -\partial_x \mathcal{H} \,. \tag{2.7}$$

The implicit time-dependence of $\mathcal{H}$, is illustrated by multiplying both sides of Eq. (2.7) with the velocity $\dot{x} = \frac{p}{M}$, and integrating in t ($\int \frac{p}{M}\dot{p}\, dt = -\int \frac{dV}{dx}\dot{x}\, dt$). This calculation takes us back to the Hamiltonian $\mathcal{H}$ of the system,

$$\int \frac{p}{M}\, dp = -\int \frac{dV}{dx}\, dx \rightarrow \mathcal{H} = \frac{p^2}{2M} + V \,, \tag{2.8}$$

where $\mathcal{H}$ appears as an integration constant.

The Lagrangian of a conservative system is defined as

$$\mathcal{L} = \frac{p^2}{M} - \mathcal{H} = \frac{p^2}{2M} - V = \frac{dS}{dt} \,, \tag{2.9}$$

where S is Hamilton's principal function [48]. Therefore, the Lagrangian is the total derivative of Hamilton's principal function. Note that the total derivative of S, is

$$\frac{dS}{dt} = \partial_t S + \dot{x}\partial_x S \,. \tag{2.10}$$

Comparing Eqs. (2.9) and (2.10), one will see a connection between the $\mathcal{H}$ and S. In fact, $\mathcal{H} = -\partial_t S$ and the gradient of S, $\partial_x S$, is the momentum p.

Going from the classical to the quantum mechanical description of a system, the potential V which appears in $\mathcal{H}$ and $\mathcal{L}$, in the equations above, includes a quantum term, the quantum potential [18], and S is the phase of the quantum mechanical wave function in polar form [20]. In the following parts of this thesis, we will not refer to Hamilton's principal function S again. It is only mentioned here because in the hydrodynamic formulation of quantum mechanics, David Bohm in his 1952 papers [20, 21], he used Hamilton's principal function S. But this can be avoided noting that the gradient of S, $\partial_x S$, is the momentum p, as we will see next in Chapter 3.

2.5 Stagnation Point Numerology

The trajectories formed in classical phase-space, discussed so far in this Chapter, reveal stagnation points[3] where the system's underlying phase-space velocity field stops completely. For classical systems, these stagnation points appear on the position axis ($p = 0$) and whenever the force is zero ($-\frac{dV(x)}{dx} = 0$), see Eq. (2.3). Therefore, formation of stagnation points away from the position axis is prohibited in classical phase-space. The velocity field $\boldsymbol{u}$ in Eq. (2.3) forms stagnation points of a vortex, separatrix and saddle at the potential's minima, maxima and saddle points, respectively. Saddle points of the potential are a combination of a vortex and a separatrix phase portrait. Fig. 2.1 demonstrates this merging of a vortex and a separatrix to form a saddle through changes of the potential. Going from panel (A) to (C) of Fig. 2.1, the central minimum in panel (A) is shifted towards the right getting closer to one of its neighbouring maximums in panels (B). The minimum and maximum of the potential, are located at the same point on the x-axis in panel (C), effectively merging and forming a saddle phase portrait.

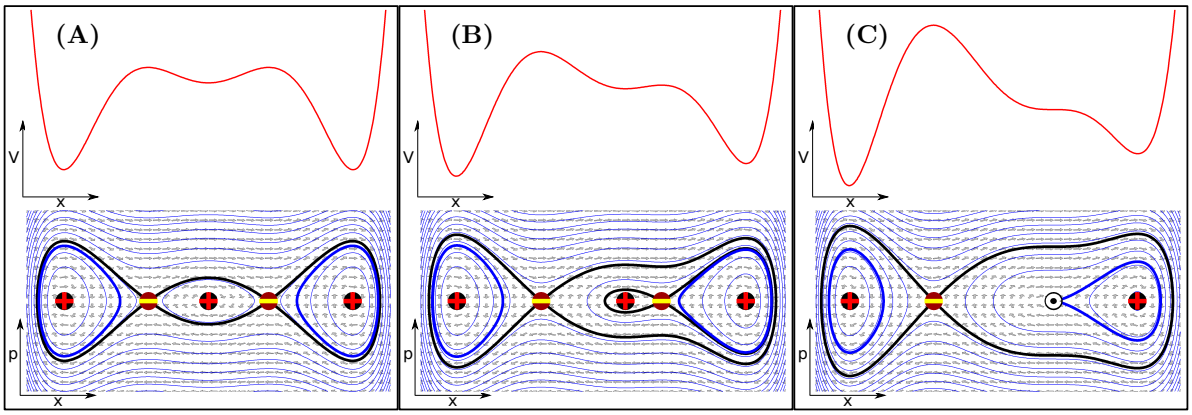

Figure 2.1 The top half of each panel ((A) to (C)), depicts a potential V, and the bottom half the potential's corresponding classical phase portrait presented as a selection of phase-space trajectories (or contour lines of its Hamiltonian $\mathcal{H}$ in Eq. (2.3), blue and black lines), presented together with the associated velocity field $\boldsymbol{u}$ in Eq. (2.3) (grey thick arrows). Thick blue lines represent the trajectories at the isosurface value of the Hamiltonian corresponding to the central minimum for panel (A), which is then shifted towards the right in panels (B) and (C) where in panel (C) it merges with its neighbouring maximum on its right. Note that at the location of the potential's minimums, the stagnation point of a vortex is formed. Similarly, thick black lines correspond to the trajectories at the two maximum points of the potential with the formation of a separatrix at these points. On the right-hand-side of panel (C), one set of thick black and blue lines appear on top of each other forming a saddle point. The stagnation points of each phase portrait carries a flow orientation winding number ω, and is labelled as in Fig. 2.2.

In this thesis, apart from the quantum harmonic oscillator (Chapter 7) and the non-linear Kerr oscillator (Chapter 8), the three classes of weakly anharmonic potentials are also under

[3] In classical physics, they are also referred to as *equilibrium, stationary, fixed, critical, invariant and rest points* [46], and in the field of singular optics, they are called singular points because the direction of the velocity field changes discontinuously in their immediate neighbourhood; passing from one side, through the singular point, to the other side, the velocity field's direction jumps discontinuously, i.e. exhibits a singularity [49].

investigation (Chapter 9); see Fig. 9.1 where they are presented together with their classical phase portraits. For their respective equations see Tables 3.1 and 9.1.

The topological nature of stagnation points orders the corresponding velocity field in large surrounding sectors of phase-space. They carry a conserved topological charge of the surrounding velocity field's orientation winding number ω [4], also known as the stagnation point's Poincaré-Hopf *index*. This is making their appearance robust to perturbations of the potential (see Fig. 2.1).

The orientation winding number ω [4], of the velocity field

$$\omega(\mathcal{L}, t) = \frac{1}{2\pi} \oint_{\mathcal{L}} d\varphi \tag{2.11}$$

tracks the orientation angle φ of the velocity field along continuous, closed, self-avoiding loops $\mathcal{L}$ in phase-space. The components of the velocity field are continuous functions, and so ω is zero except for the case where the loop contains stagnation points, such as those sketched in Fig. 2.2, for which a non-zero value of ω can occur. The value of ω stays constant unless the system's dynamics transports a stagnation point across $\mathcal{L}$ [4].

For infinitely high (or closed) potentials, like in Fig. 2.1, its overall orientation winding number is $+1$, according to the definition of Eq. (2.11). That is, if one places a large enough loop in phase-space to enclose all possible stagnation points, Eq. (2.11) yields the value $+1$. In other words, for closed potentials, if one adds together all the winding numbers corresponding to each stagnation point (refer to Fig. 2.2), the net value will be $+1$. As an example, see Fig. 2.1.

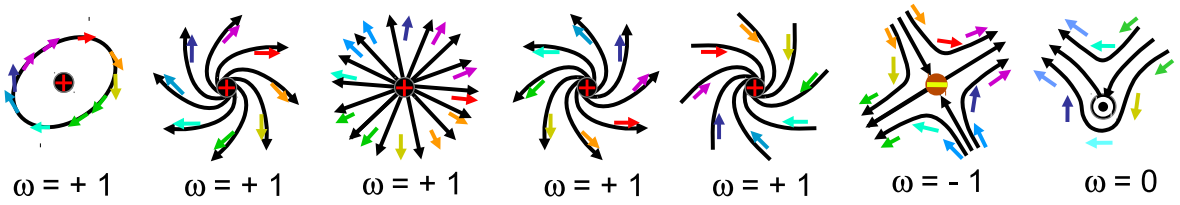

Figure 2.2 Phase-space velocity field stagnation points are characterised by their integer orientation winding number (or topological charge [49]) ω in Eq. (2.11), of the velocity field around them. The red plus sign is used for stagnation points with charge $\omega = +1$, a yellow minus sign for $\omega = -1$, and a white circle for $\omega = 0$. Notably, the velocity field near stagnation points can be skewed in phase-space, can feature skewed separatrices, and saddles oriented in any direction. The topological charges [49] can be combined or split through the system's time evolution while their sum remains conserved [4].

3 Schrödinger's Quantum Mechanics

The wave-particle duality concept (see Section 3.1), has lead to the development of quantum mechanics and the description of the quantum state of a system using the wave function (see Section 3.2), and its probability distribution which provides physical information about the quantum state of a system (see Section 3.3). In this thesis we also investigate the Rabi cycle which exhibits reversible dynamics (see Section 3.5). Finally, Section 3.6 provides an analytical method for the construction of bound-states of a static potential used in this thesis.

As mentioned in the introduction (see Chapter 1), in this thesis we only consider one-dimensional conservative bound-state quantum-mechanical systems. Hereinafter, any reference to quantum-mechanical systems, implies the use of the Hamiltonians expressed as a sum of kinetic and potential energies as in Eq. (3.11), but in general, quantum systems include field oscillators like the non-linear Kerr oscillator (see Chapter 8), also studied in this thesis.

3.1 Wave-Particle Duality

The photon is a wave packet that displays particle-like behaviour in interactions like the photoelectric effect, whereas in experiments like the Young's double-slit experiment the photon behaves like a wave. The energy E of each photon of light is proportional to its frequency f with a proportionality constant h known as Planck's constant, $E = hf = \hbar\omega$, where $\hbar = h/(2\pi)$ is Planck's constant rescaled, and $\omega = 2\pi f$ is the angular frequency (from Chapter 7 onwards $\hbar = 1$ for simplicity). Also, the relativistic energy equation of a particle of rest mass m_0 is given by $E^2 = p^2c^2 + m_0^2c^4$ where c is the speed of light and p is the momentum of the particle. Thus, treating photons as relativistic 'particles' of zero rest mass moving at the speed of light, their energy is $E = pc = hf = h\frac{c}{\lambda}$, where λ is the photon wavelength. This implies that $\lambda = \frac{h}{p}$, which is known as the de Broglie wavelength. Conversely, an electron is a point-like particle, but when travelling with speed $v = \frac{p}{m}$ it behaves like a wave with a wavelength $\lambda = \frac{h}{p}$.

Generally, quantum mechanics predicts that both the wave and particle model apply to all objects whatever their size [50] with wave-like behaviour that is represented by a complex-valued wave function $\Psi(x,t)$ which has a probabilistic interpretation.

3.2 Wave Functions

For a single particle system, this complex-valued wave function $\Psi(x,t)$, is a mathematical representation in position space of the physical state of a quantum system. Its mathematical representation in momentum space is described by the associated wave function $\tilde{\Psi}(p,t)$, defined as the Fourier transform of $\Psi(x,t)$ while $\Psi(x,t)$ is the inverse Fourier transform of $\tilde{\Psi}(p,t)$ [51],

$$\tilde{\Psi}(p,t) = \frac{1}{\sqrt{2\pi\hbar}}\int_{-\infty}^{\infty}\Psi(x,t)e^{-\frac{i}{\hbar}px}\,dx \iff \Psi(x,t) = \frac{1}{\sqrt{2\pi\hbar}}\int_{-\infty}^{\infty}\tilde{\Psi}(p,t)e^{+\frac{i}{\hbar}px}\,dp\,. \tag{3.1}$$

The wave function contains all the information of the system.

Being complex, the wave function itself cannot be identified with a single physical property of the system [50]. Instead, it can be used to obtain physical information, such as the probability $P(x,t)$ of finding the particle at a given position x or probability $\tilde{P}(p,t)$ of finding

the particle with a given momentum p, discussed further in Section 3.3,

$$P(x,t) = |\Psi(x,t)|^2 = \Psi^*(x,t)\Psi(x,t) \text{ and } \tilde{P}(p,t) = \left|\tilde{\Psi}(p,t)\right|^2 = \tilde{\Psi}^*(p,t)\tilde{\Psi}(p,t) \ , \tag{3.2}$$

where asterisk (*) denotes complex conjugation.

The following conditions are imposed on the wave functions Ψ and $\tilde{\Psi}$:

- The wave function must be a continuous, single-valued function.
- The first derivative of the wave function must be continuous everywhere except where there is an infinite discontinuity in the potential.
- The integral of the probability distribution of the wave function over x, must be one,

$$\int_{-\infty}^{\infty} P(x,t)\,dx = 1 \text{ and } \int_{-\infty}^{\infty} \tilde{P}(p,t)\,dp = 1 \ . \tag{3.3}$$

Hereinafter, eigenstate wave functions (or eigenfunctions), are denoted as $\psi_m(x)$ and $\psi_n(x)$, and are solutions to the Schrödinger equation in Eq. (3.10). Their two-state superpositions and probability distributions are denoted as $\Psi_{m,n}(x,t)$ and $P_{m,n}(x,t)$, respectively.

3.2.1 Two-State Superpositions

For the investigation of quantum dynamics we utilise in this thesis the two-state superposition $\Psi_{m,n}$, which is simultaneously described by two states denoted by the state indices m, n,

$$\Psi_{m,n}(x,t) = e^{-i\frac{E_m}{\hbar}t}\cos(\theta)\psi_m(x) + e^{-i\varphi}e^{-i\frac{E_n}{\hbar}t}\sin(\theta)\psi_n(x) \ , \tag{3.4}$$

where E_m and E_n are the corresponding eigenenergies of ψ_m and ψ_n, respectively; $\theta \in [0, \pi/2]$ is the weighting angle, and $\varphi \in [0, 2\pi)$ is the phase shift. Rearranging Eq. (3.4), yields

$$\Psi_{m,n}(x,t) = e^{-i\frac{E_m}{\hbar}t}\left(\cos(\theta)\psi_m(x) + e^{-i\frac{\Delta E}{\hbar}\left(t+\frac{\varphi\hbar}{\Delta E}\right)}\sin(\theta)\psi_n(x)\right) \ , \tag{3.5}$$

where $\Delta E = |E_n - E_m|$ is the energy difference between the two states, which determines the time it takes for the wave function in Eq. (3.5) to complete one oscillation, its period T,

$$T_{m,n} = \frac{2\pi\hbar}{\Delta E} = \frac{2\pi}{|E_n - E_m|} \ . \tag{3.6}$$

The overall phase factor in Eq. (3.5) is eliminated due to the complex conjugate in Eq. (3.2),

$$\Psi_{m,n}(x,t) = \cos(\theta)\psi_m(x) + e^{-i\frac{\Delta E}{\hbar}\left(t+\frac{\varphi\hbar}{\Delta E}\right)}\sin(\theta)\psi_n(x) \ , \tag{3.7}$$

The phase shift φ in Eq. (3.7) has the effect of only shifting the time, and therefore for simplicity we always set φ equal to zero in Eq. (3.7), reducing it to

$$\Psi_{m,n}(x,t;\theta) = \cos(\theta)\psi_m(x) + e^{-i\frac{\Delta E}{\hbar}t}\sin(\theta)\psi_n(x) \ , \tag{3.8}$$

with probability distribution (see Eq. (3.2)),

$$P_{m,n}(x,t;\theta) = \cos^2(\theta)\psi_m^2(x) + \sin^2(\theta)\psi_n^2(x) + \cos\left(\Delta E t/\hbar\right)\sin(2\theta)\psi_m(x)\psi_n(x) \ . \tag{3.9}$$

For eigenfunctions, probability distributions are time-independent due to the complex conjugate in Eq. (3.2), which eliminates the time dependence in Eq. (3.12).

3.2.2 Schrödinger Equations

The time evolution of the wave function described by a pure state, is determined by a wave equation known as Schrödinger's equation. Its position space form is presented first, followed by its momentum space counterpart. Position and momentum space in Schrödinger's representation are related through Fourier transforms, see Eq. (3.1).

Schrödinger Equation In Position Space

The non-relativistic Schrödinger equation in position space which determines the time evolution of a *pure* state $\Psi(x,t)$, of a single particle constrained to move along a straight line (the x-axis), under the influence of a time-independent potential $V(x)$, is [50]

$$i\hbar\partial_t\Psi(x,t) = \hat{\mathcal{H}}\Psi(x,t) = \left[-\frac{\hbar^2}{2M}\partial_x^2 + V(\hat{x})\right]\Psi(x,t)\ , \tag{3.10}$$

where $\hat{\mathcal{H}}$ is the Hamiltonian operator

$$\hat{\mathcal{H}} = -\frac{\hbar^2}{2M}\partial_x^2 + V(\hat{x})\ . \tag{3.11}$$

The Hamiltonian operator is related to the classical Hamiltonian $\mathcal{H} = \frac{p^2}{2M} + V(x)$ (discussed in Section 2.2), via operators in quantum mechanics, not discussed in this thesis.

Since the potential V is time-independent, applying the 'separation of variables' technique to Eq. (3.10), by substituting $\Psi_n(x,t) = \psi_n(x)T_n(t)$, yields

$$\Psi_n(x,t) = \psi_n(x)e^{-\frac{iE_n}{\hbar}t}\ . \tag{3.12}$$

Note that $\psi_n(x)$ in Eq. (3.12) is the solution of the time-independent Schrödinger equation,

$$E_n\psi_n(x) = \hat{\mathcal{H}}\psi_n(x) = \left[-\frac{\hbar^2}{2M}\frac{d^2}{dx^2} + V(\hat{x})\right]\psi_n(x)\ , \tag{3.13}$$

where E_n is the corresponding eigenenergy. The bound-state solutions (see Section 3.6), of the time-independent Schrödinger equation of Eq. (3.13), form a discrete set of eigenfunctions ψ_n with a corresponding set of eigenenergies E_n.

If the spatial part $\psi_n(x)$ of the time-dependent wave function in Eq. (3.12), is normalised, then the time-dependent wave function, $\Psi_n(x,t)$, is also normalised, since,

$$|\Psi_n(x,t)|^2 = \Psi_n(x,t)\Psi_n^*(x,t) = \psi_n(x)e^{-\frac{iE_n}{\hbar}t}\psi_n^*(x)e^{\frac{iE_n}{\hbar}t} = |\psi_n(x)|^2\ . \tag{3.14}$$

The Hamiltonian in Eq. (3.11) is a Hermitian operator. An important property of the eigenfunctions of a Hermitian operator is known as orthonormality,

$$\int \psi_m^*(x)\psi_n(x)dx = \delta_{mn}\ , \tag{3.15}$$

where δ_{mn} is the Kronecker delta. Orthonormality means that the individual eigenfunctions of a Hermitian operator are both, normalised and non-overlapping.

Schrödinger Equation In Momentum Space

To derive the Schrödinger equation in momentum space [52, 53], one can take the Fourier transform to momentum of the position space Schrödinger equation in Eq. (3.10),

$$\frac{1}{\sqrt{2\pi\hbar}}\int_{-\infty}^{\infty}\left[i\hbar\frac{\partial\Psi(x,t)}{\partial t}=-\frac{\hbar^2}{2M}\frac{\partial^2\Psi(x,t)}{\partial x^2}+V(x)\Psi(x,t)\right]e^{-\frac{i}{\hbar}px}\,dx\;. \tag{3.16}$$

The total energy term of Eq. (3.16), according to Eq. (3.1), is

$$\frac{1}{\sqrt{2\pi\hbar}}\int_{-\infty}^{\infty}i\hbar\frac{\partial\Psi(x,t)}{\partial t}e^{-\frac{i}{\hbar}px}\,dx=i\hbar\frac{\partial\tilde{\Psi}(p,t)}{\partial t}\;. \tag{3.17}$$

The kinetic energy term of Eq. (3.16), when integrated by parts twice, becomes

$$\frac{1}{\sqrt{2\pi\hbar}}\int_{-\infty}^{\infty}-\frac{\hbar^2}{2M}\frac{\partial^2\Psi(x,t)}{\partial x^2}e^{-\frac{i}{\hbar}px}\,dx=\frac{p^2}{2M}\frac{1}{\sqrt{2\pi\hbar}}\int_{-\infty}^{\infty}\Psi(x,t)e^{-\frac{i}{\hbar}px}\,dx=\frac{p^2}{2M}\tilde{\Psi}(p,t)\;. \tag{3.18}$$

For the potential term of Eq. (3.16), substitute the Fourier transform of Ψ in Eq. (3.1) and V as the inverse Fourier transform of the momentum space potential $\tilde{V}$, defined as,

$$V(x)=\frac{1}{\sqrt{2\pi\hbar}}\int_{-\infty}^{\infty}\tilde{V}(p)e^{\frac{i}{\hbar}px}\,dp\iff\tilde{V}(p)=\frac{1}{\sqrt{2\pi\hbar}}\int_{-\infty}^{\infty}V(x)e^{-\frac{i}{\hbar}px}\,dx\;, \tag{3.19}$$

and performing a change of variables, $p_1=p''-p'$ and $p_2=p'$, with the absolute of the Jacobian $|\mathcal{J}|=1$, and using the Dirac δ function, yields

$$\begin{aligned}\frac{1}{\sqrt{2\pi\hbar}}\int_{-\infty}^{\infty}V(x)\Psi(x,t)e^{-\frac{i}{\hbar}px}\,dx&=\frac{1}{(2\pi\hbar)^{\frac{3}{2}}}\iiint_{-\infty}^{\infty}\tilde{V}(p_1)\tilde{\Psi}(p_2,t)e^{\frac{i}{\hbar}x(p_1+p_2-p)}\,dp_1\,dp_2\,dx\\&=\frac{1}{(2\pi\hbar)^{\frac{3}{2}}}\iiint_{-\infty}^{\infty}\tilde{V}(p''-p')\tilde{\Psi}(p',t)e^{\frac{i}{\hbar}x(p''-p)}\,dp''\,dp'\,dx\\&=\frac{1}{\sqrt{2\pi\hbar}}\iint_{-\infty}^{\infty}\tilde{V}(p''-p')\tilde{\Psi}(p',t)\delta(p''-p)\,dp''\,dp'\\&=\frac{1}{\sqrt{2\pi\hbar}}\int_{-\infty}^{\infty}\tilde{V}(p-p')\tilde{\Psi}(p',t)\,dp'\;,\end{aligned} \tag{3.20}$$

known as the convolution Eq. (A.7) of $\tilde{V}$ and Ψ. Thus, the Fourier transform to momentum of the position space Schrödinger equation in Eq. (3.16), yields

$$i\hbar\frac{\partial\tilde{\Psi}(p,t)}{\partial t}=\frac{p^2}{2M}\tilde{\Psi}(p,t)+\frac{1}{\sqrt{2\pi\hbar}}\int_{-\infty}^{\infty}\tilde{V}(p-p')\tilde{\Psi}(p',t)\,dp'\;. \tag{3.21}$$

For simplicity, hereinafter, reference to time t is dropped, unless necessary.

3.3 Probability Distributions

In this Section we reformulate P and $\tilde{P}$ in Eq. (3.2), and also reformulate their respective probability currents. These reformulations show how Wigner's representation of quantum mechanics naturally arises from Schrödinger's representation using Fourier transforms.

Substituting for $\tilde{\Psi}$ in Eq. (3.1), into $\tilde{P}$ in Eq. (3.2), and performing a change of variables, $x_1 = x + y$ and $x_2 = x - y$ (with the absolute of the Jacobian $|\mathcal{J}| = 2$), yields

$$\tilde{P}(p) = \tilde{\Psi}^*(p)\tilde{\Psi}(p) = \frac{1}{2\pi\hbar}\iint_{-\infty}^{\infty} \Psi^*(x_1)\Psi(x_2)e^{\frac{i}{\hbar}p(x_1-x_2)}\,dx_1\,dx_2 = \frac{1}{\pi\hbar}\iint_{-\infty}^{\infty} \Psi^*(x+y)\Psi(x-y)e^{\frac{2i}{\hbar}py}\,dy\,dx\ . \tag{3.22}$$

A similar derivation obtains the following for the probability distribution P of Eq. (3.2),

$$P(x) = \Psi^*(x)\Psi(x) = \frac{1}{\pi\hbar}\iint_{-\infty}^{\infty} \tilde{\Psi}^*(p+s)\Psi(p-s)e^{-\frac{2i}{\hbar}xs}\,ds\,dp\ . \tag{3.23}$$

The $\int dy$ of (3.22) is equal to the $\int ds$ of (3.23), known as the Wigner function (see Chapter 4).

3.3.1 Probability Currents

Here we discuss the probability currents which describe the transport of the probability distribution in either the position or momentum space. For eigenfunctions, since their probability distributions are time-independent, their corresponding probability currents are zero.

Similar to the probability distributions, shown in Eqs. (3.22) and (3.23) that can be written as the projections of the Wigner function W of Eq. (4.1), here we also show that the probability currents can be written as the projections of the Wigner current $\boldsymbol{J}$ of Eq. (4.16).

The reader is reminded that for simplicity, hereinafter, reference to time t is dropped, unless necessary.

Probability Current In Position Space

The continuity equation in position space is

$$\partial_t P(x) + \partial_x \jmath(x) = 0\ , \tag{3.24}$$

where $\jmath$ is the probability current in position space, derived by rewriting Eq. (3.24) and substituting the Schrödinger equation in position space Eq. (3.10),

$$\begin{aligned}
\jmath(x) &= -\int_{-\infty}^{x} \partial_t P(x')\,dx' = -\int_{-\infty}^{x} \Psi(x')\partial_t\Psi^*(x') + \Psi^*(x')\partial_t\Psi(x')\,dx' \\
&= \frac{\hbar}{2iM}\int_{-\infty}^{x} \Psi^*(x')\partial_{x'}^2\Psi(x') - \Psi(x')\partial_{x'}^2\Psi^*(x')\,dx' \\
&= \frac{\hbar}{2iM}\left(\Psi^*(x)\partial_x\Psi(x) - \Psi(x)\partial_x\Psi^*(x)\right)\ .
\end{aligned} \tag{3.25}$$

Substituting Ψ of Eq. (3.1) into Eq. (3.25), and performing a change of variables, $p_1 = p + s$ and $p_2 = p - s$ (with the absolute of the Jacobian $|\mathcal{J}| = 2$), yields

$$\begin{aligned}
\jmath(x) &= \frac{1}{4\pi\hbar M}\iint_{-\infty}^{\infty} \tilde{\Psi}^*(p_1)\tilde{\Psi}(p_2)e^{\frac{ix}{\hbar}(p_2-p_1)}(p_1+p_2)e^{\frac{ix}{\hbar}(p_2-p_1)}\,dp_1\,dp_2 \\
&= \frac{1}{\pi\hbar M}\iint_{-\infty}^{\infty} \tilde{\Psi}^*(p+s)\tilde{\Psi}(p-s)pe^{-\frac{2i}{\hbar}xs}\,ds\,dp = \int_{-\infty}^{\infty} J_x\,dp\ ,
\end{aligned} \tag{3.26}$$

where J_x is the position component of Wigner current $\mathbf{J}$ of Eq. (4.16).

For the superposition state $\Psi_{m,n}$ in Eq. (3.8), the probability current $\jmath$ takes the form (where $\Psi = \Psi_{m,n}$ in Eq. (3.25)),

$$\jmath(x) = -\frac{\hbar}{2M}\sin(2\theta)\sin(\Delta E t/\hbar)\left(\psi_m \partial_x \psi_n - \psi_n \partial_x \psi_m\right) \ . \tag{3.27}$$

Therefore, for a two-state superposition, at any point on the x-axis, the probability current has a sinusoidal form in time t (refer to panel (b) of Fig.2. in [4]).

Probability Current In Momentum Space

The continuity equation in momentum space is

$$\partial_t \tilde{P}(p) + \partial_p \tilde{\jmath}(p) = 0 \ , \tag{3.28}$$

where $\tilde{\jmath}$ is the probability current in momentum space, derived by rewriting Eq. (3.28) and substituting the Schrödinger equation in momentum space Eq. (3.21),

$$\begin{aligned}\tilde{\jmath}(p) &= -\int_{-\infty}^{p} \partial_t \tilde{P}(p'')\, dp'' = -\int_{-\infty}^{p} \tilde{\Psi}(p'')\partial_t \tilde{\Psi}^*(p'') + \tilde{\Psi}^*(p'')\partial_t \tilde{\Psi}(p'')\, dp'' \\ &= \frac{1}{i\sqrt{2\pi\hbar^3}}\int_{-\infty}^{p} dp'' \int_{-\infty}^{\infty} dp'\ \tilde{\Psi}(p'')\tilde{V}^*(p''-p')\tilde{\Psi}^*(p') - \tilde{\Psi}^*(p'')\tilde{V}(p''-p')\tilde{\Psi}(p') \ .\end{aligned} \tag{3.29}$$

Using Eq. (3.20) and substituting for $\tilde{\Psi}$ of Eq. (3.1) into Eq. (3.29), and performing a change of variables, $x_1 = x - y$ and $x_2 = x + y$ (with the absolute of the Jacobian $|\mathcal{J}| = 2$), yields

$$\begin{aligned}\tilde{\jmath}(p) &= \frac{1}{i2\pi\hbar^2}\int_{-\infty}^{p} dp'' \iint_{-\infty}^{\infty} dx_1\, dx_2\ \left[\Psi(x_1)V(x_2)\Psi^*(x_2) - \Psi^*(x_2)V(x_1)\Psi(x_1)\right] e^{\frac{i}{\hbar}p''(x_2-x_1)} \\ &= \frac{1}{i\pi\hbar^2}\iint_{-\infty}^{\infty} dy\, dx\ \left[V(x+y) - V(x-y)\right]\Psi^*(x+y)\Psi(x-y)\int_{-\infty}^{p} dp'' e^{\frac{2i}{\hbar}p''y} \\ &= -\frac{1}{\pi\hbar}\iint_{-\infty}^{\infty}\left[\frac{V(x+y)-V(x-y)}{2y}\right]\Psi^*(x+y)\Psi(x-y)e^{\frac{2i}{\hbar}py}\, dy\, dx \\ &= \int_{-\infty}^{\infty} J_p\, dx \ ,\end{aligned} \tag{3.30}$$

where J_p is the momentum component of Wigner current $\mathbf{J}$ of Eq. (4.16).

3.4 The Hydrodynamic Formulation

In 1927, Erwin Madelung developed the hydrodynamic equations of quantum mechanics [19]. Independently, in 1952, following De Broglie's pilot wave theory, David Bohm developed what we now call the De Broglie-Bohm theory [20, 21]. The basic equations behind this theory, are equivalent to Madelung's equations.

Starting from the definition of momentum in position space [23],

$$p(x) = \hbar\,\mathrm{Im}\left(\frac{\partial_x \psi}{\psi}\right) \ , \tag{3.31}$$

the quantum force is the total derivative of $p(x)$ in Eq. (3.31),

$$\begin{aligned}\frac{dp}{dt} &= \partial_t p + \dot{x}\partial_x p = \partial_t p + \partial_x\left(\frac{p^2}{2M}\right) = -\frac{dV}{dx} + \frac{\hbar^2}{2M}\partial_x\left[\mathrm{Re}\left(\frac{\partial_x^2\psi}{\psi}\right) + \mathrm{Im}^2\left(\frac{\partial_x\psi}{\psi}\right)\right] \\ &= -\frac{dV}{dx} + \frac{\hbar^2}{4M}\partial_x\left[\frac{\partial_x^2 P}{P} - \frac{1}{2}\left(\frac{\partial_x P}{P}\right)^2\right] = -\frac{dV}{dx} + \frac{\hbar^2}{4M}\frac{1}{P}\partial_x\left(P\partial_x\left(\frac{\partial_x P}{P}\right)\right) \\ &= -\frac{dV}{dx} - \partial_x Q = -\partial_x U\ . \end{aligned} \tag{3.32}$$

The potential term Q is the quantum potential, thus, $U = V + Q$ is the overall potential in quantum mechanics. For eigenfunctions, U represents the eigenvalue energy of the state.

In Chapter 2, we discussed that the momentum p Eq. (3.31) is the gradient of Hamilton's principal function S. It is also worth noting that Eq. (3.31) can also be expressed as [23]

$$p(x) = \frac{M\jmath(x)}{P(x)} = \frac{M\int_{-\infty}^{\infty} dp\, J_x(x,p)}{\int_{-\infty}^{\infty} dp\, W(x,p)}\ , \tag{3.33}$$

where the probability current $\jmath(x) = \hbar\,\mathrm{Im}\left(\psi^*\partial_x\psi\right)/M = \int_{-\infty}^{\infty} dp\, J_x(x,p)$ as it was already defined in Eq. (3.26), and $P(x) = \int_{-\infty}^{\infty} dp\, W(x,p)$, also shown in Eq. (3.23). The function W is the phase-space Wigner distribution, and J_x is the position component of Wigner's current. Both of these functions belong in Wigner's representation of quantum mechanics discussed next in Chapter 4. It is well-known that the projection onto position space of Wigner's representation, gives rise to the hydrodynamic formulation of quantum mechanics [15, 26], already discussed in this section.

3.5 The Rabi Cycle

In this Section we briefly discuss the reversible dynamics of the non-conservative but non-decoherent (and therefore non-dissipative), Rabi cycle [54, 55] of an atom driven *on resonance* by incident radiation. In Chapter 9 this on resonance Rabi cycle is used for the study of Wigner current's features.

For the superposition of the ground and first-excited states,

$$\Psi_0(x,t) = e^{-i\frac{E_0}{\hbar}t}\psi_0(x) \text{ and } \Psi_1(x,t) = e^{-i\frac{E_1}{\hbar}t}\psi_1(x)\ , \tag{3.34}$$

with eigenenergies, E_0 and E_1, respectively, the Rabi state Ψ_R takes the form

$$\Psi_R(x,t) = \cos\left(\frac{\Omega_R}{2}t\right)\Psi_0(x,t) - i\sin\left(\frac{\Omega_R}{2}t\right)\Psi_1(x,t) \tag{3.35}$$

$$= \cos\left(\frac{\Omega_R}{2}t\right)e^{-i\frac{E_0}{\hbar}t}\psi_0(x) - i\sin\left(\frac{\Omega_R}{2}t\right)e^{-i\frac{E_1}{\hbar}t}\psi_1(x)\ , \tag{3.36}$$

(with initial condition: $\Psi_R(x,0) = \psi_0(x)$), where Ω_R is called the Rabi frequency which is proportional to the amplitude of the incident electromagnetic field. In the rotating wave approximation [55], the Hamiltonian $\hat{\mathcal{H}}_R$ of this Rabi state Ψ_R in Eq. (3.36) is given by

$$\hat{\mathcal{H}}_R = \begin{pmatrix} E_0 & \frac{\Omega_R\hbar}{2}e^{i\frac{\Delta E}{\hbar}t} \\ \frac{\Omega_R\hbar}{2}e^{-i\frac{\Delta E}{\hbar}t} & E_1 \end{pmatrix}\ , \tag{3.37}$$

where the energy difference $\Delta E = E_1 - E_0 = \omega\hbar$ and $\omega = \frac{\Delta E}{\hbar}$ is the natural frequency of the system. In this discussion we only consider a Rabi cycle on resonance, therefore ω is also the driving frequency of the incident radiation.

Discarding: i) the overall phase factor $e^{-i\frac{E_0}{\hbar}t}$ (which does not affect the corresponding probability distribution), and ii) the phase shift $-i$, the Rabi state Ψ_R in Eq. (3.36) becomes

$$\Psi_R(x,t) = \cos\left(\frac{\Omega_R}{2}t\right)\psi_0(x) + \sin\left(\frac{\Omega_R}{2}t\right)e^{-i\frac{\Delta E}{\hbar}t}\psi_1(x)\,. \tag{3.38}$$

The probabilities of the Rabi state Ψ_R in Eq. (3.38) being in the ground and first-excited states, $\Psi_0(x,t)$ and $\Psi_1(x,t)$ given in Eq. (3.34), are

$$|\langle\Psi_0|\Psi_R\rangle|^2 = \left|\int_{-\infty}^{\infty}\Psi_0^*(x,t)\Psi_R(x,t)\,dx\right|^2 = \cos^2\left(\frac{\Omega_R}{2}t\right) \tag{3.39}$$

and

$$|\langle\Psi_1|\Psi_R\rangle|^2 = \left|\int_{-\infty}^{\infty}\Psi_1^*(x,t)\Psi_R(x,t)\,dx\right|^2 = \sin^2\left(\frac{\Omega_R}{2}t\right)\,, \tag{3.40}$$

respectively. Plots of Eqs. (3.39) and (3.40) are shown in Fig. 3.1 for $\Omega_R = \frac{1}{8}$. This Rabi state Ψ_R in Eq. (3.38) is employed in Chapter 9 for the investigation of Wigner current's features.

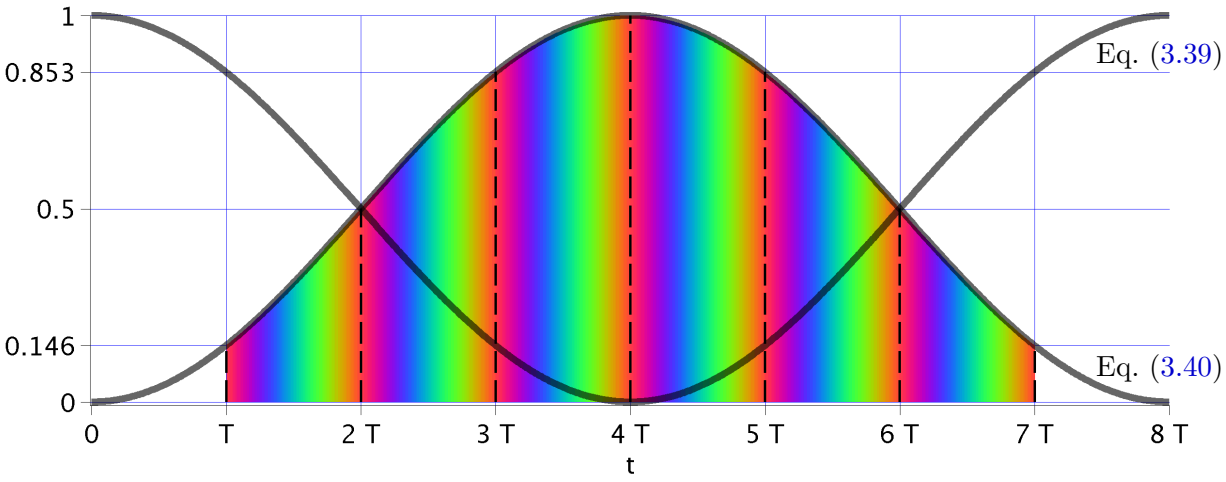

Figure 3.1 Plots of Eqs. (3.39) and (3.40) depicting the time evolution of the probability of the Rabi state $\Psi_R(x,t)$ in Eq. (3.38) being in the ground and first-excited states, $\Psi_0(x,t)$ and $\Psi_1(x,t)$ in Eq. (3.34), respectively, with Rabi frequency $\Omega_R = \frac{1}{8}$ and $\Delta E = \hbar = 1$. Since the system is on resonance, the natural frequency of the system $\omega = \frac{\Delta E}{\hbar} = 1$ is also the driving frequency of the incident radiation. The natural period of the system $T = \frac{2\pi}{\omega} = 2\pi$ and the time period of this Rabi cycle $T_R = \frac{2\pi}{\Omega_R} = 8T$. The periodic colour scheme, which runs between T and $7T$ and has a period of T, highlights the portion of the time evolution of the Rabi cycles depicted in Fig. 3.1. The grid lines indicate values of the probability at the passing of each natural period T (vertical black dash lines) of the system.

3.6 Bound-States

Here we discuss the analytical method used in this thesis for the construction of bound-states of a static potential which are solutions to the time-independent Schrödinger equation,

$$\hat{\mathcal{H}}\psi(x) = \left[-\frac{\hbar^2}{2M}\frac{d^2}{dx^2} + V(x)\right]\psi(x) = E\psi(x)\ . \tag{3.41}$$

First we consider the appropriate boundary conditions that the wave function $\psi(x)$ in Eq. (3.41), is constrained to satisfy. For example, consider a potential $V(x)$ which goes to a constant value V_{max} at $x \to \pm\infty$ and is less than V_{max} everywhere on the x-axis. A continuous potential of this type with minimum value V_{min} is shown in Fig. 9.1 (middle top panel). For $E < V_{\text{min}}$, there are no normalisable solutions of Eq. (3.41). For $V_{\text{min}} < E < V_{\text{max}}$, there are discrete values of E for which normalisable solutions exist. These values $\{E_0, E_1, ...\}$, are eigenenergies and the corresponding eigenfunctions are $\{\psi_0, \psi_1, \ldots\}$. For $E \geq V_{\text{max}}$, there is a continuum of energy levels with the wave functions having the behaviour of a plane wave, $e^{\pm ikx}$ for $x \to \pm\infty$. This thesis only takes into consideration discrete bound-states which are in the range $V_{\text{min}} < E < V_{\text{max}}$ and for which the following main properties apply:

- The eigenfunctions $\{\psi_0, \psi_1, \ldots\}$ can all be chosen to be real.
- Since the Hamiltonian is a Hermitian operator, the eigenenergies $\{E_0, E_1, \ldots\}$ are necessarily real. Furthermore, for one-dimensional problems, the eigenenergies are non-degenerate, i.e. each eigenenergy does not correspond to more than one eigenfunction.
- The eigenfunctions are normalisable (see Eq. (3.3)), i.e. vanish fast enough as $x \to \pm\infty$.
- The eigenfunctions are orthogonal Eq. (3.15).
- If the eigenfunctions are ordered according to increasing energy, i.e., $\{E_0 < E_1 < E_2, \ldots\}$, then the corresponding eigenfunctions are automatically ordered in the number of nodes, with the eigenfunction ψ_n having n nodes.
- ψ_{n+1} has a node located between each pair of consecutive zeros of the ψ_n (including the zeros at $x \to \pm\infty$).

3.6.1 Bound-State Spectrum

The ideas introduced here are based on supersymmetry in quantum mechanics which refers to the application of supersymmetry algebra to quantum mechanics [44]. They constitute a powerful tool for deriving the eigenfunctions and eigenenergies of the one-dimensional potentials studied in this thesis.

Starting from a single particle Hamiltonian (superscript (1), links the potential to its corresponding Hamiltonian),

$$\hat{\mathcal{H}}^{(1)} \equiv -\frac{\hbar^2}{2M}\frac{d^2}{dx^2} + V^{(1)}(x)\ , \tag{3.42}$$

the Scrödinger equation for the ground state wave function ψ_0 is

$$\hat{\mathcal{H}}^{(1)}\psi_0(x) = -\frac{\hbar^2}{2M}\frac{d^2\psi_0}{dx^2} + V^{(1)}(x)\psi_0(x) = E_0\psi_0(x) = 0\ , \tag{3.43}$$

where the ground state eigenenergy $E_0 = 0$, so that,

$$V^{(1)}(x) = \frac{\hbar^2}{2M}\frac{\psi_0''(x)}{\psi_0(x)} \,. \tag{3.44}$$

This provides knowledge of the potential from the knowledge of its ground state wave function.

The Hamiltonian is factorized using the creation $A^\dagger$ and annihilation A operators,

$$\hat{\mathcal{H}}^{(1)} = A^\dagger A \,, \quad A^\dagger = \chi(x) - \frac{\hbar}{\sqrt{2M}}\frac{d}{dx} \,, \quad A = \chi(x) + \frac{\hbar}{\sqrt{2M}}\frac{d}{dx} \,. \tag{3.45}$$

The potential $V^{(1)}$ is then recognised as

$$V^{(1)} = \frac{\hbar^2}{2M}\frac{\psi_0''}{\psi_0} = \chi^2 - \frac{\hbar}{\sqrt{2M}}\frac{d\chi}{dx} \tag{3.46}$$

since

$$\hat{\mathcal{H}}^{(1)}\psi_0 = A^\dagger A\psi_0 = -\frac{\hbar^2}{2M}\frac{d^2\psi_0}{dx^2} + \chi^2\psi_0 - \frac{\hbar}{\sqrt{2M}}\psi_0\frac{d\chi}{dx} = 0 \,. \tag{3.47}$$

where the function χ is referred to as the superpotential [39, 43]. Recognising that $A\psi_0 = 0$, the superpotential is written as,

$$\chi(x) = -\frac{\hbar}{\sqrt{2M}}\frac{\psi_0'(x)}{\psi_0(x)} = -\frac{\hbar}{\sqrt{2M}}\frac{d(\ln\psi_0)}{dx} \,. \tag{3.48}$$

Given the superpotential χ, the ground state wave function is obtained using,

$$\psi_0(x) = \mathcal{N}\exp\left(-\frac{\sqrt{2M}}{\hbar}\int^x \chi(x')dx'\right) \,, \tag{3.49}$$

where $\mathcal{N}$ is the normalisation constant.

By reversing the order of A and $A^\dagger$, we obtain the operator $\hat{\mathcal{H}}^{(2)}$,

$$\hat{\mathcal{H}}^{(2)} = AA^\dagger = -\frac{\hbar^2}{2M}\frac{d^2}{dx^2} + V^{(2)}(x) \,, \tag{3.50}$$

which is the Hamiltonian corresponding to a new potential $V^{(2)}$,

$$V^{(2)}(x) = \chi^2(x) + \frac{\hbar}{\sqrt{2M}}\frac{d\chi(x)}{dx} \,. \tag{3.51}$$

The potentials $V^{(1)}$ and $V^{(2)}$, Eqs. (3.46) and (3.51), respectively, are known as supersymmetric partner potentials.

For $n > 0$, using the Schrödinger equation for $\hat{\mathcal{H}}^{(1)}$,

$$\hat{\mathcal{H}}^{(1)}\psi_n^{(1)} = A^\dagger A\psi_n^{(1)} = E_n^{(1)}\psi_n^{(1)} \,, \tag{3.52}$$

which implies

$$\hat{\mathcal{H}}^{(2)}A\psi_n^{(1)} = AA^\dagger A\psi_n^{(1)} = E_n^{(1)}A\psi_n^{(1)} \,. \tag{3.53}$$

Similarly, using the Schrödinger equation for $\hat{\mathcal{H}}^{(2)}$,

$$\hat{\mathcal{H}}^{(2)}\psi_n^{(2)} = AA^\dagger\psi_n^{(2)} = E_n^{(2)}\psi_n^{(2)} \,, \tag{3.54}$$

which implies

$$\hat{\mathcal{H}}^{(1)}A^{\dagger}\psi_n^{(2)} = A^{\dagger}AA^{\dagger}\psi_n^{(2)} = E_n^{(2)}A^{\dagger}\psi_n^{(2)} \,. \tag{3.55}$$

From Eqs. (3.52) to (3.55), and the fact that $E_0^{(1)} = 0$, the eigenenergies and eigenfunctions of the two Hamiltonians $\hat{\mathcal{H}}^{(1)}$ and $\hat{\mathcal{H}}^{(2)}$ are related by,

$$E_n^{(2)} = E_{n+1}^{(1)} \,, \quad E_0^{(1)} = 0 \,, \tag{3.56}$$

$$\psi_n^{(2)} = \left[E_{n+1}^{(1)}\right]^{-1/2} A\psi_{n+1}^{(1)} \,, \tag{3.57}$$

$$\psi_{n+1}^{(1)} = \left[E_n^{(2)}\right]^{-1/2} A^{\dagger}\psi_n^{(2)} \,. \tag{3.58}$$

It is therefore possible to obtain the eigenfunctions and eigenenergies of Hamiltonian $\hat{\mathcal{H}}^{(2)}$ if we are already familiar with the corresponding set of solutions of Hamiltonian $\hat{\mathcal{H}}^{(1)}$. An illustration of this result in shown as Fig.1. of [39].

The supersymmetric potentials $V^{(1)}$ and $V^{(2)}$, Eqs. (3.46) and (3.51), respectively, are said to be shape invariant. Shape invariance refers to the shape of the potentials. The term is a bit misleading as the infinite square well potential and the Eckart potential are very different in shape even though they fulfil the shape-invariance condition [39]

$$V^{(2)}(x;a_1) = V^{(1)}(x;a_2) + R(a_1) \,, \tag{3.59}$$

where a_1 is a set of parameters and a_2 is a function of a_1, and the remainder $R(a_1)$ is independent of x. In Eq. (3.59), the potentials $V^{(1)}(x;a_2)$ and $V^{(2)}(x;a_1)$ are said to be shape invariant. A beautiful simplification for a special class of solvable shape-invariant potentials has been formed by Gendenshtein [43]. Table 3.1 presents the shape invariant solvable potentials under consideration in this thesis. In the following derivation, for simplicity we will assume that $2M$ and $\hbar$ are both equal to unity.

Let us now construct a series of Hamiltonians $\hat{\mathcal{H}}^{(s)}$, where $s = 1, 2, 3, \ldots$, as

$$\hat{\mathcal{H}}^{(s)} = -\frac{d^2}{dx^2} + V^{(1)}(x;a_s) + \sum_{k=1}^{s-1} R(a_k) \,, \tag{3.60}$$

where $a_s = f^{(s-1)}(a_k)$, i.e., a_s is a function with respect to a_k, which is applied $(s-1)$ times. By comparing the spectrum of $\hat{\mathcal{H}}^{(s)}$ and $\hat{\mathcal{H}}^{(s+1)}$, and using Eq. (3.59),

$$\hat{\mathcal{H}}^{(s+1)} = -\frac{d^2}{dx^2} + V^{(1)}(x;a_{s+1}) + \sum_{k=1}^{s} R(a_k) \tag{3.61}$$

$$= -\frac{d^2}{dx^2} + V^{(2)}(x;a_s) + \sum_{k=1}^{s-1} R(a_k) \,. \tag{3.62}$$

Thus, $\hat{\mathcal{H}}^{(s)}$ and $\hat{\mathcal{H}}^{(s+1)}$ are supersymmetric partner Hamiltonians and hence have identical bound-state spectra except for the ground state of $\hat{\mathcal{H}}^{(s)}$ whose energy is,

$$E_0^{(s)} = \sum_{k=1}^{s-1} R(a_k) \,. \tag{3.63}$$

This follows from Eq. (3.60) and the fact that $E_0^{(1)} = 0$. On going back from $\hat{\mathcal{H}}^{(s)}$ to $\hat{\mathcal{H}}^{(s-1)}$, etc, and finally reaching $\hat{\mathcal{H}}^{(1)}$, the complete eigenenergy spectrum of $\hat{\mathcal{H}}^{(1)}$ is given by

$$E_n^{(1)}(a_1) = \sum_{k=1}^{n} R(a_k) \; , \quad E_0^{(1)}(a_1) = 0 \; , \tag{3.64}$$

and using Eq. (3.56) it is also clear that the n'th unnormalised eigenfunction $\psi_n^{(1)}(x; a_1)$ for the original Hamiltonian $\hat{\mathcal{H}}^{(1)}(x; a_1)$ is given by,

$$\psi_n^{(1)}(x; a_1) \propto A^\dagger(x; a_1) A^\dagger(x; a_2) \ldots A^\dagger(x; a_n) \psi_0^{(1)}(x; a_{n+1}) \; , \tag{3.65}$$

which is clearly a generalisation of the operator method of constructing the eigenfunctions for the one-dimensional quantum harmonic oscillator potential discussed in Chapter 7. A more convenient way of expressing Eq. (3.65) is the following identity,

$$\psi_n^{(1)}(x; a_1) = A^\dagger(x; a_1) \psi_{n-1}^{(1)}(x; a_2) \; , \tag{3.66}$$

where $\psi_n^{(1)}(x; a_1)$ are the eigenfunctions corresponding to the first partner Hamiltonian and $\psi_{n-1}^{(1)}(x; a_2)$ are the eigenfunctions corresponding to the second partner Hamiltonian. Eq. (3.66) allows us to construct the entire family of solutions.

Potential	Harmonic Oscillator	Eckart	Rosen-Morse	Morse
$\chi(x)$	$\sqrt{\frac{M}{2}}\Omega^{\odot}x - B$	$A\tan(\alpha x) + B\sec(\alpha x)$	$A\tanh(\alpha x) + \frac{B}{A}$	$A - Be^{-\alpha x}$
$V^{(1)}(x;\alpha_1)$	$\frac{M}{2}\Omega^{\odot 2}\left(x-\sqrt{\frac{2}{M}}\frac{B}{\Omega^{\odot}}\right)^2$ $-\frac{\hbar\Omega^{\odot}}{2}$	$\left(B^2+A^2-\frac{\alpha\hbar A}{\sqrt{2M}}\right)\times$ $\left(\tan(\alpha x)+\frac{\left(A-\frac{\alpha\hbar}{2\sqrt{2M}}\right)B\sec(\alpha x)}{B^2+A^2-\frac{\alpha\hbar A}{\sqrt{2M}}}\right)^2$ $-\frac{\left(A-\frac{\alpha\hbar}{2\sqrt{2M}}\right)^2 B^2\sec^2(\alpha x)}{\left(B^2+A^2-\frac{\alpha\hbar A}{\sqrt{2M}}\right)}-\frac{\alpha\hbar A}{\sqrt{2M}}-B^2$	$\left(A^2+\frac{\alpha\hbar A}{\sqrt{2M}}\right)\times$ $\left(\tanh(\alpha x)+\frac{B}{\left(A^2+\frac{\alpha\hbar A}{\sqrt{2M}}\right)}\right)^2$ $+\frac{B^2}{A^2}-\frac{\alpha\hbar A}{\sqrt{2M}}-\frac{B^2}{\left(A^2+\frac{\alpha\hbar A}{\sqrt{2M}}\right)}$	$B^2\left(\frac{2\sqrt{2}A+\alpha}{2\sqrt{2}B}-e^{-\alpha x}\right)^2$ $+A^2-\left(A+\frac{\alpha}{2\sqrt{2}}\right)^2$
a_1	$\Omega^{\odot}$	A	A	A
a_2	$\Omega^{\odot}$	$A+\frac{n\alpha\hbar}{\sqrt{2M}}$	$A-\frac{n\alpha\hbar}{\sqrt{2M}}$	$A-\frac{n\alpha\hbar}{\sqrt{2M}}$
$R(a_1)$	$\hbar\Omega^{\odot}$	$a_2^2-a_1^2$	$a_1^2-a_2^2$ $+B^2\left[\frac{1}{a_1^2}-\frac{1}{a_2^2}\right]$	$a_1^2-a_2^2$
Eigenenergy	$n\hbar\Omega^{\odot}$	$\left(A+\frac{n\alpha\hbar}{\sqrt{2M}}\right)^2-A^2$	$A^2-\left(A-\frac{n\alpha\hbar}{\sqrt{2M}}\right)^2$ $+B^2\left[\frac{1}{A^2}-\frac{1}{\left(A-\frac{n\alpha\hbar}{\sqrt{2M}}\right)^2}\right]$	$A^2-\left(A-\frac{n\alpha\hbar}{\sqrt{2M}}\right)^2$
Groundstate (unnormalized)	$e^{\left[-\frac{M\Omega^{\odot}}{2\hbar}\left(x-\sqrt{\frac{2}{M}}\frac{B}{\Omega^{\odot}}\right)^2\right]}$	$(\cos(\alpha x))^{\frac{\sqrt{2M}(A+B)}{\alpha\hbar}}$ $\times(1+\sin(\alpha x))^{-\frac{\sqrt{2M}B}{\alpha\hbar}}$	$(\mathrm{sech}(\alpha x))^{\frac{\sqrt{2M}A}{\alpha\hbar}}\, e^{\left[-\frac{\sqrt{2M}}{\hbar A}Bx\right]}$	$e^{\left[-\frac{\sqrt{2M}}{\hbar}\left(Ax+\frac{B}{\alpha}e^{-\alpha x}\right)\right]}$

Table 3.1 The shape-invariant potentials studied in this thesis and their respective parameters necessary for the construction of their eigenenergies and eigenfunctions. This table is a shorter and modified version of Table. 1 in [39]. This table is revised in Table 9.1 where the parameters A, B, α and $\Omega^{\odot}$ are given a constrained form defined by the anharmonicity parameter D (see Chapter 9).

4 Wigner's Quantum Mechanics

Quantum mechanics is usually introduced using Schrödinger's representation (see Chapter 3), in either position or momentum space, mainly in position space. In contrast, classical mechanics is mainly studied in phase-space, representing the motion of particles simultaneously in position and momentum (see Chapter 2). It is therefore natural to wonder whether quantum mechanics can also be represented in phase-space. This is achieved using Wigner's quantum mechanics which is "*a reformulation of Schrödinger's quantum mechanics*" [56], in phase-space. Just like Schrödinger's representation is based on the wave function (in either position or momentum space) to describe the quantum state of a system, Wigner's representation is based on the Wigner distribution discussed in Section 4.1, which describes the quantum state of a system in phase-space [57, 58]. The corresponding continuity equation which describes the time evolution of the Wigner distribution, is called the Wigner equation discussed in Section 4.2. The Wigner equation gives rise to the Wigner current $\boldsymbol{J}$ discussed in Section 4.3, which is the quantum analogue of the classical phase-space current $\boldsymbol{j}$ in Eq. (2.3).

4.1 The Wigner Distribution

In this Section we introduce the Wigner distribution, discuss some of its mathematical properties and define the Wigner distribution of a particular two-state superposition which will be used in later Chapters of this thesis to characterise quantum phase-space dynamics.

According to Heisenberg's uncertainty principle [25], $\Delta x \Delta p_x \geq \frac{1}{2}\hbar$, where Δx and Δp are the standard deviations of the probability distributions P and $\tilde{P}$ in Eqs. (3.23) and (3.22), respectively, we cannot *simultaneously measure* the precise position and momentum of a quantum particle. Therefore we *cannot* assign a probability distribution to it referring to its exact position and momentum, but there does exist a quantum phase-space distribution, the Wigner distribution, first introduced by Eugene Wigner in 1932 [1]. The Wigner distribution is set apart from other quantum phase-space distributions [56] by the fact that it simultaneously yields the projections (probability distributions P and $\tilde{P}$), and overlap between two distinct states in Eq. (4.4), while maintaining its form in Eq. (4.1) when evolved in time. It therefore joins P and $\tilde{P}$, into phase-space. "*Of course, [the Wigner distribution] cannot be really interpreted as the simultaneous probability for coordinates and momenta*" [1], due to the uncertainty principle (discussed above) and also since it can assume negative values. Also, only the Wigner distribution's averages and uncertainties evolve *momentarily* classically [59, 60]. This is why we consider the Wigner distribution as the *"closest quantum analogue of the classical phase-space distribution"* [6], and is therefore also referred to as a quantum phase-space *quasi*-probability distribution.

The Wigner distribution W [1] (first discussed in this thesis in Section 3.3),

$$W(x,p,t) = \frac{1}{\pi\hbar}\int_{-\infty}^{\infty} \langle x-y|\hat{\varrho}(t)|x+y\rangle e^{\frac{2i}{\hbar}py}\,dy = \frac{1}{\pi\hbar}\int_{-\infty}^{\infty} \langle p-s|\hat{\tilde{\varrho}}(t)|p+s\rangle e^{-\frac{2i}{\hbar}xs}\,ds\,, \quad (4.1)$$

is defined as the Wigner transform of the density operator $\hat{\varrho}$ of the position space density function $\langle x-y|\hat{\varrho}(t)|x+y\rangle = \Psi^*(x+y,t)\Psi(x-y,t)$ for pure states, where asterisk (*) denotes complex conjugation, rendering it time-independent for eigenfunctions. An equivalent Wigner transform applies for the momentum space density operator $\hat{\tilde{\varrho}}$ in the second expression of

W in Eq. (4.1). Conversely, the density operators $\hat{\varrho}$ and $\hat{\tilde{\varrho}}$ are the Weyl transforms of the Wigner distribution. This invertible mapping between quantum phase-space functions and operators in the Schrödinger representation, is known as the Wigner-Weyl transform [40, 61–63]. Throughout this thesis we only consider pure states.

The two expressions of W in Eq. (4.1) are related by Fourier transforms, shown below by substituting for $\tilde{\Psi}$ the Fourier transform of Ψ in Eq. (3.1), and then performing a change of variables, $x_1 = X + y$ and $x_2 = X - y$ (with the absolute of the Jacobian $|\mathcal{J}| = 2$),

$$\begin{aligned} W(x,p,t) &= \frac{1}{\pi\hbar}\int_{-\infty}^{\infty} \tilde{\Psi}^*(p+s)\tilde{\Psi}(p-s)e^{-\frac{2i}{\hbar}xs}\,ds \\ &= \frac{1}{2\pi^2\hbar^2}\iiint_{-\infty}^{\infty} \Psi^*(x_1)\Psi(x_2)e^{\frac{i}{\hbar}\{[x_1(p+s)-x_2(p-s)]-2xs\}}\,dx_1\,dx_2\,ds \\ &= \frac{1}{\pi^2\hbar^2}\iiint_{-\infty}^{\infty} \Psi^*(X+y)\Psi(X-y)e^{\frac{2i}{\hbar}(py+Xs-xs)}\,dy\,dX\,ds \\ &= \frac{1}{\pi\hbar}\iint_{-\infty}^{\infty} \Psi^*(X+y)\Psi(X-y)e^{\frac{2i}{\hbar}py}\delta(X-x)\,dy\,dX \\ &= \frac{1}{\pi\hbar}\int_{-\infty}^{\infty} \Psi^*(x+y)\Psi(x-y)e^{\frac{2i}{\hbar}py}\,dy\,. \end{aligned} \tag{4.2}$$

4.1.1 Mathematical Properties of the Wigner Distribution

Hereinafter, reference to variables, such as the position x, the momentum p, the time t, etc., is dropped, unless necessary.

The Wigner distribution is a real-valued phase-space function:

This is demonstrated by using the fact that the Wigner distribution's Fourier transform integrands in Eq. (4.1) are Hermitian functions in y and s, respectively, hence,

$$W = \frac{2}{\pi\hbar}\,\mathrm{Re}\left(\int_0^{\infty} \Psi^*(x+y)\Psi(x-y)e^{\frac{2i}{\hbar}py}\,dy\left\{= \int_0^{\infty} \Psi^*(p+s)\Psi(p-s)e^{-\frac{2i}{\hbar}xs}\,ds\right\}\right)\,. \tag{4.3}$$

The marginal projections of the Wigner distribution:

The main property of the Wigner distribution distinguishing it from other quantum phase-space distributions [11, 56], is its projections along p and x, which are the probability distributions of position and momentum, $\int_{-\infty}^{\infty} W(x,p,t)\,dp = P(x,t)$ and $\int_{-\infty}^{\infty} W(x,p,t)\,dx = \tilde{P}(p,t)$, respectively (see Section 3.3). It follows that for normalised wave functions, the Wigner distribution is also normalised, since $\int_{-\infty}^{\infty} P(x,t)\,dx = \int_{-\infty}^{\infty} \tilde{P}(p,t)\,dp = 1$.

The overlap of two distinct Wigner distributions:

The overlap of two distinct Wigner distributions is the scalar product of their wave functions, $\iint_{-\infty}^{\infty} dp\,dx\,W_\Psi W_\Phi = \frac{1}{2\pi\hbar}\,|\langle\Psi|\Phi\rangle|^2$. This is shown below by recognising the integral over p as the Dirac δ function. Then evaluating the integral over y_2, and performing a change of

variables, $x' = x + y$ and $x'' = x - y$ (with the absolute of the Jacobian $|\mathcal{J}| = \frac{1}{2}$), yields [6, 11]

$$\begin{aligned}\iint_{-\infty}^{\infty} W_\Psi W_\Phi \, dp\, dx &= \frac{1}{\pi\hbar} \iiint_{-\infty}^{\infty} dy_1\, dy_2\, dx\ \Psi^*(x+y_1)\Psi(x-y_1)\Phi^*(x+y_2)\Phi(x-y_2) \frac{1}{\pi\hbar}\int_{-\infty}^{\infty} dp\, e^{\frac{2i}{\hbar}p(y_1+y_2)} \\ &= \frac{1}{\pi\hbar} \iiint_{-\infty}^{\infty} dy_1\, dy_2\, dx\ \Psi^*(x+y_1)\Psi(x-y_1)\Phi^*(x+y_2)\Phi(x-y_2)\delta(y_1+y_2) \\ &= \frac{1}{\pi\hbar} \iint_{-\infty}^{\infty} dy\, dx\ \Psi^*(x+y)\Psi(x-y)\Phi^*(x-y)\Phi(x+y) \\ &= \frac{1}{2\pi\hbar} \iint_{-\infty}^{\infty} dx'\, dx''\ \Psi^*(x')\Psi(x'')\Phi^*(x'')\Phi(x') \\ &= \frac{1}{2\pi\hbar} \left| \int_{-\infty}^{\infty} dx\ \Psi^*(x)\Phi(x) \right|^2 = \frac{1}{2\pi\hbar} |\langle\Psi|\Phi\rangle|^2 \ , \end{aligned} \tag{4.4}$$

The Wigner distribution can go negative:

If Ψ and Φ are orthogonal states, Eq. (4.4) is zero. Thus, either W_Ψ or W_Φ, or both, must assume negative values; the only non-negative Wigner distributions are Gaussian distributions [64]. The occurrence of negative values in the Wigner distribution is known to be one of the very hallmarks of the fact that a system is quantum-mechanical in nature, i.e. defies description in terms of classical probability theory [11].

Spatial and time inversions:

A spatial inversion of the wave function, $\Psi(x) \to \Psi(-x)$, and of its associated Hamiltonian, $\mathcal{H}(x,p)\left\{= \frac{p^2}{2M} + V(x)\right\} \to \mathcal{H}(-x,p)\left\{= \frac{p^2}{2M} + V(-x)\right\}$ (assuming $\mathcal{H}$ is time-independent and real-valued), transforms W in Eq. (4.1) as follows:
for superpositions like in Eq. (3.8) where $\Psi^*(x,t) = \Psi(x,-t)$,

$$\begin{aligned} W(x,p,t) \to W(-x,p,-t) &= \frac{1}{\pi\hbar}\int_{-\infty}^{\infty} \Psi^*(-x-y)\Psi(-x+y)e^{\frac{2i}{\hbar}py}\, dy \\ &= \frac{1}{\pi\hbar}\int_{-\infty}^{\infty} \Psi^*(-x+y)\Psi(-x-y)e^{-\frac{2i}{\hbar}py}\, dy = W(-x,-p,t) \end{aligned} \tag{4.5}$$

and for eigenfunctions where $\psi^* = \psi$,

$$W(x,p,t) \to W(-x,p) = W(-x,-p) = \frac{1}{\pi\hbar}\int_{-\infty}^{\infty} \psi(-x-y)\psi(-x+y)\cos\left(\frac{2}{\hbar}py\right) dy\ . \tag{4.6}$$

Thus, with z being perpendicular to the xp-plane (right-handed system; $\boldsymbol{x} \times \boldsymbol{p} = \boldsymbol{z}$), a spatial inversion on the system reflects W about the xz- and pz-plane, which amounts to an even parity transformation $(x,p) \to (-x,-p)$. As indicated in Eq. (4.5), this parity transformation is equivalent to a reflection of a time-inverted W about the pz-plane.

For eigenfunctions, a spatial inversion on the system only amounts to a reflection of W about the pz-plane since for eigenfunctions W has a reflectional symmetry about the xz-plane, as indicated in Eq. (4.6).

Applying both spatial and time inversions reflects W about the pz-plane,

$$W(x,p,t) \to W(-x,-p,-t) = W(-x,p,t)\ . \tag{4.7}$$

4.1.2 The Wigner Distribution of a Two-State Superposition

We use the following definition of the Wigner distribution W_{mn} to define the Wigner distribution terms of a two-state superposition, as

$$W_{mn} = \frac{1}{\pi\hbar}\int_{-\infty}^{\infty} \psi_m^*(x+y)\psi_n(x-y)e^{\frac{2i}{\hbar}py}\,dy = \begin{cases} m \neq n \text{ for off-diagonal terms} \\ m = n \text{ for eigenfunctions} \end{cases} . \tag{4.8}$$

Thus, the Wigner distribution $W_{m,n}$ of $\Psi_{m,n}$ in Eq. (3.8), is defined as

$$W_{m,n} = \cos^2(\theta)W_{mm} + \sin^2(\theta)W_{nn} + \sin(2\theta)\,\mathrm{Re}\left(e^{-\frac{i\Delta E}{\hbar}t}W_{mn}\right) . \tag{4.9}$$

Note that $W_{mn} = W_{nm}^*$ (asterisk (*) denotes complex conjugation).

If the eigenfunctions ψ_m and ψ_n are orthogonal,

$$\iint_{-\infty}^{\infty} W_{mn}(x,p)\,dp\,dx = \iint_{-\infty}^{\infty} W_{nm}^*(x,p)\,dp\,dx = \int_{-\infty}^{\infty} \psi_m(x)\psi_n(x)\,dx = 0 , \tag{4.10}$$

which implies that both W_{mn} and W_{nm} have equal parts of negative and positive values, and that the Wigner distribution $W_{m,n}$ in Eq. (4.9) is normalised $\int_{-\infty}^{\infty} W_{m,n}\,dx\,dp = 1$.

4.2 The Time Evolution of the Wigner Distribution

Just like the Schrödinger equation determines the time evolution of a wave function, equivalently, the Wigner distribution's time evolution is determined by the Wigner equation, introduced alongside the Wigner distribution by Eugene Wigner in 1932 [1]. In 1949 [12], José Moyal generalised the Wigner equation to the Moyal equation which applies to any Hamiltonian. The Moyal equation is the Wigner-transform of the von Neumann equation which applies to pure and mixed states, unlike Schrödinger's equation which only applies to pure states [62].

Wigner's equation and its infinite-sum form, commonly referred to as the quantum Liouville equation, are presented in this Section together with Moyal's equation and its integral form.

4.2.1 Wigner Equation

For mechanical systems with Hamiltonians of the form $\mathcal{H} = \frac{p^2}{2M} + V(x)$ (i.e., as a sum of kinetic and potential energies), the time evolution of W of Eq. (4.1), was first derived by Eugene Wigner in 1932 [1], as described below.

Differentiating W of Eq. (4.1) with respect to t, then rearranging using Schrödinger's equation (3.10), and replacing differentiations with respect to x with differentiations with

respect to y, and finally integrating by parts, yields

$$\begin{aligned}
\partial_t W &= \frac{1}{\pi\hbar}\int_{-\infty}^{\infty} dy\ \left[\Psi(x-y,t)\partial_t\Psi^*(x+y,t)+\Psi^*(x+y,t)\partial_t\Psi(x-y,t)\right] e^{\frac{2i}{\hbar}py} \\
&= \frac{1}{\pi\hbar}\int_{-\infty}^{\infty} dy\ \left\{\frac{i\hbar}{2M}\left[\Psi^*(x+y)\partial_x^2\Psi(x-y)-\Psi(x-y)\partial_x^2\Psi^*(x+y)\right]\right. \\
&\quad \left.+\frac{i}{\hbar}\left[V(x+y)-V(x-y)\right]\Psi^*(x+y)\Psi(x-y)\right\} e^{\frac{2i}{\hbar}py} \\
&= \frac{1}{\pi\hbar}\int_{-\infty}^{\infty} dy\ \left\{-\frac{p}{m}\partial_x\left[\Psi^*(x+y,t)\Psi(x-y,t)\right]\right. \\
&\quad \left.+\frac{i}{\hbar}\left[V(x+y)-V(x-y)\right]\Psi^*(x+y,t)\Psi(x-y,t)\right\} e^{\frac{2i}{\hbar}py} \\
&= -\frac{p}{M}\partial_x W+\frac{i}{\pi\hbar^2}\int_{-\infty}^{\infty} dy\ \left[V(x+y)-V(x-y)\right]\Psi^*(x+y,t)\Psi(x-y,t)e^{\frac{2i}{\hbar}py}\ , \qquad (4.11)
\end{aligned}$$

known as the Wigner equation. Due to its form, the Wigner equation is also valid for piecewise potentials (apart from infinite square-wells), and it is numerically more accurate, unlike its infinite-sum form in Eq. (4.12), see Chapter 5.

The Quantum Liouville Equation

Expanding $V(x+y)$ and $V(x-y)$ in Eq. (4.11), in Taylor series with respect to y, yields

$$\partial_t W = -\frac{p}{M}\partial_x W+\sum_{l=0}^{\infty}\frac{(i\hbar/2)^{2l}}{(2l+1)!}\partial_p^{2l+1}W\partial_x^{2l+1}V\ , \qquad (4.12)$$

known as the quantum Liouville equation. This form of Wigner's equation shows the presence of the quantum correction terms ($l\geq 1$), which in the classical limit of $\hbar\to 0$ vanish reducing Eq. (4.12) to its classical form: $\partial_t W=-\frac{p}{M}\partial_x W+\partial_p W\partial_x V$. This preserves the kinetic term, unlike in Schrödinger's equation of Eq. (3.10) where the kinetic term vanishes in this limit [62].

4.2.2 Moyal Equation

Wigner's equation only applies to mechanical systems with Hamiltonians of the form $\mathcal{H}=\frac{p^2}{2M}+V(x)$ (i.e., as a sum of kinetic and potential energies). For a general Hamiltonian the time evolution of the Wigner distribution is described by the Moyal equation

$$\partial_t W=-\left\{\{W,\mathcal{H}\}\right\}=-\frac{2}{\hbar}W(x,p,t)\sin\left(\frac{\hbar}{2}\left(\overleftarrow{\partial_x}\overrightarrow{\partial_p}-\overleftarrow{\partial_p}\overrightarrow{\partial_x}\right)\right)\mathcal{H}(x,p)\ , \qquad (4.13)$$

named after José Moyal for his 1949 work [12]. The Moyal equation in is the Wigner transform [8, 12, 40, 61–63] of the von Neumann equation $\frac{\partial\hat{\varrho}}{\partial t}=-\frac{i}{\hbar}\left[\hat{\mathcal{H}},\hat{\varrho}\right]$. Thus, the Wigner transform maps the commutator $[\bullet,\bullet]$ in the von Neumann equation to the Moyal bracket $\{\{\bullet,\bullet\}\}$ in Eq. (4.13), which is the quantum analogue of the Poisson bracket $\{\bullet,\bullet\}$.

Baker Equation

The Moyal equation of Eq. (4.13) is only true for Taylor-expandable Hamiltonians (in both x and p). Thus, a general integral form of Moyal's equation is [13, 56]

$$\partial_t W = -\frac{2}{\pi^2\hbar^3}\iiiint_{-\infty}^{\infty} dx'\,dx''\,dp'\,dp''\,W(x+x',p+p') \times \mathcal{H}(x+x'',p+p'')\sin\left(\frac{2}{\hbar}(x'p''-x''p')\right) . \quad (4.14)$$

4.3 The Wigner Current

In this Section we will introduce the concept of the Wigner current $\boldsymbol{J}$ [2], at times incorrectly referred to in literature as Wigner "*flow*" [3, 4]. It is the quantum analogue of the classical phase-space current $\boldsymbol{j}$ in Eq. (2.3), and it is derived from Wigner's representation of quantum mechanics. Just as the probability currents in position and momentum space in Schrödinger's representation fulfil their respective continuity equations (see Section 3.3.1), the Wigner current $\boldsymbol{J}$ fulfils its own continuity equation [2–4, 30],

$$\partial_t W + \boldsymbol{\nabla}\bullet\boldsymbol{J} = \partial_t W + \partial_x J_x + \partial_p J_p = 0\ ,\ \text{where}\ \boldsymbol{J} = \begin{pmatrix} J_x \\ J_p \end{pmatrix} . \quad (4.15)$$

Different formulations of the quantum phase-space continuity equation were discussed in Section 4.2. For one-dimensional systems, the Wigner current $\boldsymbol{J}$ in Eq. (4.15) is a vector field with two components, its position component J_x and its momentum component J_p.

The explicit form of the Wigner current's components is presented for the quantum-mechanical case in this Section, for the quantum harmonic oscillator in Chapter 7, and for the non-linear Kerr oscillator case in Chapter 8. In this Section we also discuss some of the mathematical properties of the Wigner current.

The Wigner current will be used in later Chapters of this thesis to characterise quantum phase-space dynamics. We will integrate the Wigner current in phase-space, at a fixed time, and therefore generate its *momentary* fieldlines. Note that these fieldlines are somewhat unphysical in two main regards. Firstly, they are not trajectories [27], and secondly, since they portray a momentary snapshot of Wigner current's structure, they do not depict the transport of quantum phase-space features *over long times*. The structure of Wigner current fieldline portraits, particularly near its stagnation points, can more easily be discerned visually when using fieldlines (from now on we drop the term 'momentary'), rather than looking at depictions of its field arrows alone. Wigner current fieldlines also depict the quantum analogue of classical phase portraits; they are a valuable visualisation tool. In comparison, classical phase portrait trajectories in conservative systems are fixed (foliation in phase-space) and only depend on the potential, see Chapter 2. In quantum phase-space, Wigner current fieldlines can change over time and depend on the quantum state of the system.

4.3.1 The Wigner Current of Mechanical Systems

The Wigner current $\boldsymbol{J}$ of mechanical systems is determined by comparing the abstract form of $\boldsymbol{J}$'s continuity equation of Eq. (4.15) with Eq. (4.11) which yields the integral form of $\boldsymbol{J}$,

or with Eq. (4.12) which yields infinite-sum form of $\boldsymbol{J}$,

$$\boldsymbol{J} = \begin{pmatrix} \frac{p}{M}\frac{1}{\pi\hbar}\int_{-\infty}^{\infty}\Psi^*(x+y)\Psi(x-y)e^{\frac{2i}{\hbar}py}\,dy \\ -\frac{1}{\pi\hbar}\int_{-\infty}^{\infty}\left[\frac{V(x+y)-V(x-y)}{2y}\right]\Psi^*(x+y)\Psi(x-y)e^{\frac{2i}{\hbar}py}\,dy \end{pmatrix} = \begin{pmatrix} \frac{p}{M}W \\ -\sum_{l=0}^{\infty}\frac{(i\hbar/2)^{2l}}{(2l+1)!}\partial_p^{2l}W\partial_x^{2l+1}V \end{pmatrix} . \tag{4.16}$$

Note that this form of $\boldsymbol{J}$ is specific to mechanical systems with Hamiltonians of the form $\mathcal{H} = \frac{p^2}{2M} + V(x)$ (i.e., as a sum of kinetic and potential energies). For field oscillators, like the Kerr oscillator discussed in Chapter 8, $\boldsymbol{J}$ is determined using the Moyal equation of Eq. (4.13).

For numerical reasons, we truncate the infinite-sum expression of the J_p component in Eq. (4.16) after L terms yielding the *truncated current* with cutoff L,

$$\boldsymbol{J}_{[L]} = \begin{pmatrix} J_x \\ J_{p,[L]} \end{pmatrix} = \begin{pmatrix} \frac{p}{M}W \\ \sum_{l=0}^{L} J_{p,l} \end{pmatrix} , \text{ where } J_{p,l} = -\frac{(i\hbar/2)^{2l}}{(2l+1)!}\partial_p^{2l}W\partial_x^{2l+1}V\,. \tag{4.17}$$

According to the continuity equation Eq. (4.15), J_p can also take the form

$$J_p = -\int \partial_t W + \partial_x J_x\,dp\,. \tag{4.18}$$

For the quantum-mechanical case, the form of J_p in Eq. (4.18) does not depend explicitly on the potential. For eigenfunctions, due to the time-independence of the associated Wigner distribution (see Section 4.1), J_p in Eq. (4.18) becomes $J_p = -\int \partial_x J_x\,dp$.

4.3.2 Mathematical Properties of the Wigner Current

Just like the Wigner distribution discussed in 4.1.1, the components of the Wigner current in Eq. (4.15) are also real-valued phase-space functions which can also go negative and their marginal projections are the probability currents in position and momentum space. These mathematical properties of the Wigner current are presented here together with its time reversal and parity transformations.

The Wigner current's components are real-valued phase-space functions:

This is demonstrated by using the fact that the Fourier transform integrands of the components of $\boldsymbol{J}$ in Eq. (4.16) are Hermitian functions in y, hence,

$$\boldsymbol{J} = \begin{pmatrix} \frac{p}{M}\frac{2}{\pi\hbar}\,\mathrm{Re}\left(\int_0^{\infty}\Psi^*(x+y)\Psi(x-y)e^{\frac{2i}{\hbar}py}\,dy\right) \\ -\frac{2}{\pi\hbar}\,\mathrm{Re}\left(\int_0^{\infty}\left[\frac{V(x+y)-V(x-y)}{2y}\right]\Psi^*(x+y)\Psi(x-y)e^{\frac{2i}{\hbar}py}\,dy\right) \end{pmatrix} . \tag{4.19}$$

The marginal projections of the Wigner current's components:

Just like the projections of W are the probability distributions (see Section 4.1.1), equivalently, the projections of W's continuity equation in Eq. (4.11), reduce to the continuity equations,

$$\int_{-\infty}^{\infty}(\partial_t W + \partial_x J_x + \partial_p J_p)\,dp = \partial_t P(x,t) + \partial_x \jmath(x,t) = 0 \tag{4.20}$$

$$\text{and } \int_{-\infty}^{\infty}(\partial_t W + \partial_x J_x + \partial_p J_p)\,dx = \partial_t \tilde{P}(p,t) + \partial_p \tilde{\jmath}(p,t) = 0\,. \tag{4.21}$$

Thus, the marginal projections, $\int_{-\infty}^{\infty} J_x\, dp$ in Eq. (4.20) and $\int_{-\infty}^{\infty} J_p\, dx$ in Eq. (4.21), yield

$$\int_{-\infty}^{\infty} J_x\, dp = \frac{1}{\pi\hbar M} \iint_{-\infty}^{\infty} \Psi^*(x+y)\Psi(x-y) p e^{\frac{2i}{\hbar}py}\, dy\, dp \tag{4.22}$$
$$= \frac{\hbar}{2iM} \iint_{-\infty}^{\infty} \Psi^*(x+y)\Psi(x-y)\partial_y\delta(y)\, dy = \frac{\hbar}{2iM}\left(\Psi^*\partial_x\Psi - \Psi\partial_x\Psi^*\right) = \jmath(x,t)$$

$$\text{and} \int_{-\infty}^{\infty} J_p\, dx = -\frac{1}{\pi\hbar} \iint_{-\infty}^{\infty} \left[\frac{V(x+y)-V(x-y)}{2y}\right] \Psi^*(x+y)\Psi(x-y) e^{\frac{2i}{\hbar}py}\, dy\, dx \tag{4.23}$$
$$= \frac{1}{i\sqrt{2\pi\hbar^3}} \int_{-\infty}^{p}\int_{-\infty}^{\infty} \tilde{\Psi}(\mathcal{P})U^*(\mathcal{P}-p')\tilde{\Psi}^*(p') - \tilde{\Psi}^*(\mathcal{P})U(\mathcal{P}-p')\tilde{\Psi}(p')\, dp'\, d\mathcal{P} = \tilde{\jmath}(p,t)\ ,$$

which are the probability currents in position and momentum space, respectively. Additionally, the marginal projections $\int_{-\infty}^{\infty} J_x\, dx$ in Eq. (4.21) and $\int_{-\infty}^{\infty} J_p\, dp$ in Eq. (4.20), yield

$$\int_{-\infty}^{\infty} J_x\, dx = \frac{p}{\pi\hbar M} \iint_{-\infty}^{\infty} \tilde{\Psi}^*(p+s)\tilde{\Psi}(p-s) e^{-\frac{2i}{\hbar}xs}\, ds\, dx \tag{4.24}$$
$$= \frac{p}{M} \int_{-\infty}^{\infty} \tilde{\Psi}^*(p+s)\tilde{\Psi}(p-s)\delta(s)\, ds = \tilde{P}(p,t)\frac{p}{M}$$

$$\text{and} \int_{-\infty}^{\infty} J_p\, dp = -\frac{1}{\pi\hbar} \iint_{-\infty}^{\infty} \left[\frac{V(x+y)-V(x-y)}{2y}\right] \Psi^*(x+y)\Psi(x-y) e^{\frac{2i}{\hbar}py}\, dy\, dp \tag{4.25}$$
$$= -\int_{-\infty}^{\infty} \left[\frac{V(x+y)-V(x-y)}{2y}\right] \Psi^*(x+y)\Psi(x-y)\delta(y)\, dy = -P(x,t)\frac{dV}{dx}\ .$$

The Wigner current's components can go negative:

Integrating overall phase-space each component of $\boldsymbol{J}$ yields Ehrenfest's theorem [59],

$$\iint_{-\infty}^{\infty} J_x\, dx\, dp = \frac{\langle p\rangle}{M} = \frac{d\langle x\rangle}{dt} \text{ and } \iint_{-\infty}^{\infty} J_p\, dx\, dp = -\left\langle \frac{dV}{dx}\right\rangle = \frac{d\langle p\rangle}{dt}\ . \tag{4.26}$$

As mentioned in Section 4.1, the Wigner distribution of an eigenfunction is time-independent. This time-independence also applies to the Wigner current's components due to their form in Eq. (4.16). Thus, the average velocity and average force in Eq. (4.26), reduce to zero for eigenfunctions, hence, the Wigner current's components have equal parts of negative and positive values; $\iint_{-\infty}^{\infty} J_x\, dx\, dp = 0$ and $\iint_{-\infty}^{\infty} J_p\, dx\, dp = 0$. For superpositions, the average velocity and average force are time-dependent, hence, the Wigner current's components for superpositions do acquire negative values but not in equal parts; $\iint_{-\infty}^{\infty} J_x\, dx\, dp \neq 0$ and $\iint_{-\infty}^{\infty} J_p\, dx\, dp \neq 0$. These negativities of the Wigner current's components invert the direction of the current, causing formation of vortices and separatrices, but maintaining conservation of the current's winding number, which "*reveals fundamental topological order in quantum dynamics*" [4], as it is implied by the Poincaré-Hopf theorem (see Section 2.5). This translates to the following observation: vortices and separatrices in phase-space must be created or annihilated together while quantum dynamics evolves (see Fig. 9.11 and Figs. 4 and 5 of [4]).

Spatial and time inversions:

A spatial inversion of the wave function, $\Psi(x) \to \Psi(-x)$, and of its associated Hamiltonian, $\mathcal{H}(x,p)\left\{= \frac{p^2}{2M} + V(x)\right\} \to \mathcal{H}(-x,p)\left\{= \frac{p^2}{2M} + V(-x)\right\}$ (assuming $\mathcal{H}$ is time-independent and

real-valued), transforms $\boldsymbol{J}(x,p,t)$ in Eq. (4.16) as follows:
for superpositions like in Eq. (3.8) where $\Psi^*(x,t)=\Psi(x,-t)$,

$$\begin{aligned}\boldsymbol{J}(x,p,t)\to\begin{pmatrix}J_x(-x,p,-t)\\-J_p(-x,p,-t)\end{pmatrix}&=\begin{pmatrix}\frac{p}{M}\frac{1}{\pi\hbar}\int_{-\infty}^{\infty}\Psi^*(-x-y)\Psi(-x+y)e^{\frac{2i}{\hbar}py}\,dy\\ \frac{1}{\pi\hbar}\int_{-\infty}^{\infty}\left[\frac{V(-x+y)-V(-x-y)}{2y}\right]\Psi^*(-x-y)\Psi(-x+y)e^{\frac{2i}{\hbar}py}\,dy\end{pmatrix}\\&=\begin{pmatrix}\frac{p}{M}\frac{1}{\pi\hbar}\int_{-\infty}^{\infty}\Psi^*(-x+y)\Psi(-x-y)e^{-\frac{2i}{\hbar}py}\,dy\\ \frac{1}{\pi\hbar}\int_{-\infty}^{\infty}\left[\frac{V(-x+y)-V(-x-y)}{2y}\right]\Psi^*(-x+y)\Psi(-x-y)e^{-\frac{2i}{\hbar}py}\,dy\end{pmatrix}=\begin{pmatrix}-J_x(-x,-p,t)\\-J_p(-x,-p,t)\end{pmatrix}\end{aligned}\tag{4.27}$$

and for eigenfunctions where $\psi^*=\psi$,

$$\begin{aligned}\boldsymbol{J}(x,p,t)\to\begin{pmatrix}J_x(-x,p)\\-J_p(-x,p)\end{pmatrix}&=\begin{pmatrix}-J_x(-x,-p)\\-J_p(-x,-p)\end{pmatrix}\\&=\begin{pmatrix}\frac{p}{M}\frac{1}{\pi\hbar}\int_{-\infty}^{\infty}\psi(-x-y)\psi(-x+y)\cos\left(\frac{2}{\hbar}py\right)\,dy\\ \frac{1}{\pi\hbar}\int_{-\infty}^{\infty}\left[\frac{V(-x+y)-V(-x-y)}{2y}\right]\psi(-x-y)\psi(-x+y)\cos\left(\frac{2}{\hbar}py\right)\,dy\end{pmatrix}.\end{aligned}\tag{4.28}$$

Thus, a spatial inversion on the system reflects $\boldsymbol{J}$ over the x- and p-axis and also changes the sign of $\boldsymbol{J}$, as indicated in Eq. (4.27), which amounts to an odd parity transformation. Whereas, for eigenfunctions, a spatial inversion on the system reflects $\boldsymbol{J}$ over the p-axis and rotates it by π radians. A time inversion on the superposition, $\Psi(x,t)\to\Psi(x,-t)=\Psi^*(x,t)$, reflects $\boldsymbol{J}$ over the x-axis and rotates it by π radians (see Eq. (4.27)).

Applying both space and time inversions reflects $\boldsymbol{J}$ over the p-axis and rotates it by π radians,

$$\boldsymbol{J}(x,p,t)\to\begin{pmatrix}-J_x(-x,-p,-t)=J_x(-x,p,t)\\-J_p(-x,-p,-t)=-J_p(-x,p,t)\end{pmatrix}.\tag{4.29}$$

5 Numerical Aspects

This Chapter discusses the numerical aspects of the work presented in later Chapters of this thesis. Specifically, Section 5.1 and 5.2 discusses the numerical computation of the Wigner functions and associated Wigner current's fieldline portraits presented in Chapters 7, 8 and 9. Section 5.3 also highlights key points on how the results presented in this thesis were checked.

5.1 Numerical Computation of the Wigner Function

Analytical closed-form expressions of the Wigner function are known for harmonic systems (and their isomorphic partners [14]), see Section 7.2), and for the Morse oscillator (see Section 9.2). Even for the Morse oscillator, it is time consuming to compute the Wigner function for high anharmonicities [65]. Thus, in this thesis, for anharmonic potentials, W in Eq. (4.1) is determined using the midpoint Riemann sum with integration limits $[-Y, Y]$,

$$W(x,p,t) \approx \frac{\Delta Y}{\pi\hbar} \sum_{r=1}^{N_y} \Psi^*(x+y_r)\Psi(x-y_r) e^{\frac{2i}{\hbar}\frac{n\pi}{2Y}y_r} \ , \ \text{for } y_r = -Y + (r-\frac{1}{2})\Delta Y \ , \tag{5.1}$$

where N_y is an even number of partitions of width $\Delta Y = \frac{2Y}{N_y}$. The substitution $p = \frac{n\pi}{2Y}$ follows from the Nyquist–Shannon sampling theorem [66] with $\left\{ n \in \mathbb{Z} : -\frac{N_y}{2} \leq n \leq \frac{N_y}{2} \right\}$. Thus, the p-axis domain of the numerical integration in Eq. (5.1) is $p \in \left[-\frac{\pi N_y}{4Y}, \frac{\pi N_y}{4Y} \right]$. Note that y_r in Eq. (5.1), ranges from $y_1 = -Y + \frac{Y}{N_y}$ to $y_{N_y} = Y - \frac{Y}{N_y}$. Therefore, the values of y_r represent the values of y in Eq. (4.1) and appear within the integration limits $[-Y, Y]$. We also make sure that $\Psi^*(x+y)\Psi(x-y) \approx 0$ at the integration limits for all values of x. For a sufficiently high value of N_y, the numerically integrated Wigner function in Eq. (5.1), must satisfy the Wigner function projections, Eqs. (3.22) and (3.23), together with the normalisation condition,

$$\iint_{-\infty}^{\infty} dp\, dx\, W(x,p,t) = 1 \ . \tag{5.2}$$

For a two-state superposition $\Psi_{m,n}$ Eq. (3.8), the corresponding Wigner function in Eq. (4.9) includes the diagonal terms, W_{mm} and W_{nn} (see Section 4.1.2), which must satisfy Eq. (4.4).

5.2 Numerical Computation of the Wigner Current

The method described in the previous Section for the numerical computation of the Wigner function, was also employed for the numerical computation of the Wigner Current $\boldsymbol{J}$. In our early attempts we made use of the infinite-sum form of $\boldsymbol{J}$ which lead to the respective continuity equation, the quantum Liouville equation in Eq. (4.12) diverging (instead of converging to zero), when more quantum correction terms were included. This divergence was only observed in open potentials like the Rosen-Morse potential (see Fig. 5.1) and was avoided with the use of the integral form of $\boldsymbol{J}$ in Eq. (4.16) and the use its respective continuity equation, the Wigner equation in Eq. (4.11). This also meant that the variables which controlled the accuracy of our results, were reduced to the number of digits (decimal places) used by the program and the number of partitions N_y in the numerical integration of Eq. (5.1).

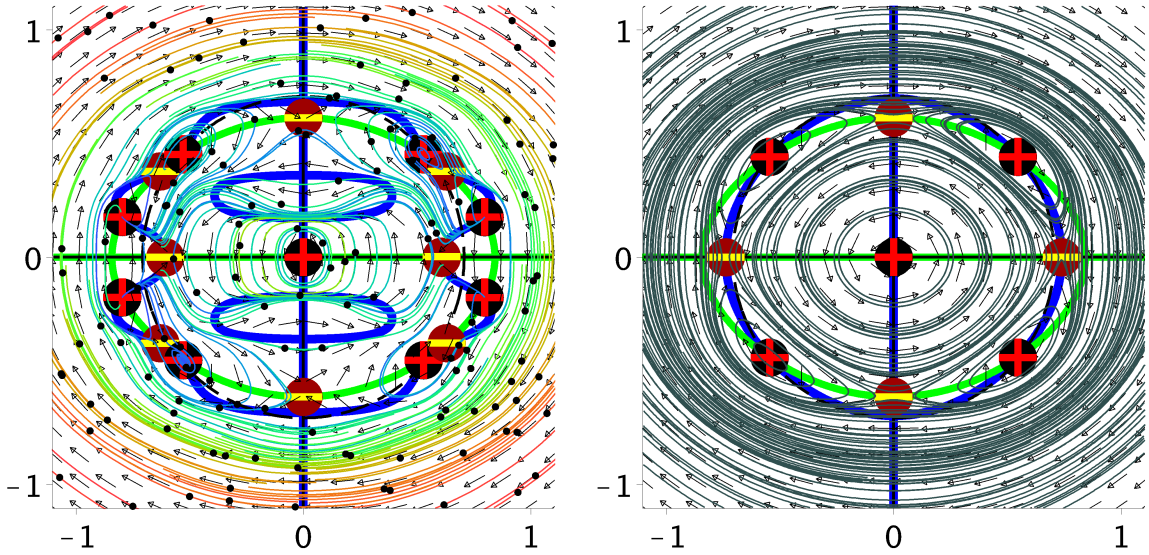

Figure 5.1 Left panel: Incorrect Wigner current fieldline portraits $\boldsymbol{J}_{[5]}$ in Eq. (4.17) for the first excited state of the Rosen-Morse potential. **Right panel:** Correct Wigner current fieldline portraits (same case as left panel) with the use of the integral form of $\boldsymbol{J}$ in Eq. (4.16). The stagnation points of $\boldsymbol{J}$ at the crossings of $J_x = 0$ and $J_p = 0$ (thick green and blue lines, respectively) are labelled as in Fig. 2.2. The left panel clearly demonstrates incorrect formation of spirals (sources and sinks) in phase-space, which are forbidden by the Wigner current fieldline portraits of eigenfunctions. The incorrect fieldline portraits of the left panel are due to the poor convergence of the infinite-sum form of $\boldsymbol{J}$ in Eq. (4.16). Attempts to use a cutoff for the infinite-sum, high enough for the series to converge, were in vain as the infinite-sum was diverging.

The Wigner current fieldline portraits presented in Chapters 7, 8 and 9, were produced with the use of the following equations of motion,

$$\begin{pmatrix} x(t') = J_x(x(t'), p(t'), t) \\ p(t') = J_p(x(t'), p(t'), t) \end{pmatrix} . \tag{5.3}$$

Note that, even though $\boldsymbol{J}$ is time-dependent for superposition states, its time t was set to a constant value while the $\boldsymbol{J}$ fieldlines were integrated for $t' \in [-\mathcal{T}, \mathcal{T}]$ using the Runge–Kutta–Fehlberg method (also known as the RKF45 method) [67]. Therefore, these $\boldsymbol{J}$ fieldlines are the *momentary* fieldlines depicting the dynamics of the system as a snapshot in phase-space.

By switching from the infinite-sum to the integral form of $\boldsymbol{J}$ in Eq. (4.16), our results improved dramatically, see Fig. 5.1.

5.3 Consistency Checks

The list below summarises some of the reasons as to why we feel confident with the results presented in this thesis:

1. It is well-known that if the divergence of a vector field is zero, such a vector can be written as the curl of a vector potential, see Chapter 2. Such a divergence-less vector

field is referred to as a solenoidal vector field, as it forms closed loops. For the Wigner current of eigenfunctions, $\boldsymbol{\nabla} \bullet \boldsymbol{J} = 0$, since the Wigner function is time independent. This translates to closed fieldlines of $\boldsymbol{J}$ in Fig. 9.3.

2. $\boldsymbol{J}$'s field arrows are tangent to its respective fieldlines, see Figs. 9.3, 9.6, 9.7 and 9.8.

3. $J_x = 0$ at $p = 0$ (see Eq. (4.16)), and since $d^{(2l+1)}V = 0$ for even potentials, so $J_p = 0$ at $x = 0$, see Figs. 9.3, 9.6 and 9.7.

4. The J_x and J_p components in Eq. (4.16) are well behaved functions with no singularities.

5. Field arrows and fieldlines follow the symmetries of Wigner current for eigenfunctions summarised in Section 4.3.2.

6 When is Wigner's Current Liouvillian?

In Chapter 4 we discussed Wigner's phase-space representation of quantum mechanics. We introduced the Wigner function, its continuity equation and the Wigner current, the quantum analogue of the classical phase-space current. The Wigner current will be used from this Chapter onwards as a tool for the study of quantum dynamics in phase-space.

Unlike in classical mechanics (see Chapter 2), quantum mechanics precludes the existence of phase-space trajectories due to Heisenberg's uncertainty principle [25]. The concept of trajectories, instead of $\boldsymbol{J}$-fieldlines (studied in this thesis), originates from the phase-space transport in Lagrangian form using the total (or comoving) derivative $\frac{dW}{dt}$ in Eq. (6.2) [27, 30, 31, 41]. But Heisenberg demonstrated that the concept of a sharply defined phase-space trajectory is incompatible with the uncertainty principle. Instead, a quantum description (with the use of the Wigner function), describes the motion of a single system which fundamentally entails variance in position and momentum and thus uncertainty about its center-of-mass movement. This in itself has not stopped us from describing quantum systems using trajectories:

- The field of quantum-characteristics studies a system's center-of-mass motion in phase-space and its higher order moments.
- The concept of paths (unlike trajectories, paths do not have to conform with the equations of motion) has been fruitful in path-integral formalisms applied to configuration or phase-space.
- Configuration space trajectories are used in Bohm's version of quantum theory and have experimental relevance [24].
- Semi-classical methods employ classical trajectories along which quantum objects are carried [28, 68, 69].

Also, techniques employing trajectories in quantum phase-space [28–33], are of great interest in theoretical chemistry since the great complexity of chemical systems forces us to find simplifications to make calculations of quantum dynamics tractable.

For reasons stated above, in this thesis we do not take the trajectory approach to our investigation of quantum dynamics. Instead, we make use of the $\boldsymbol{J}$-fieldlines.

In this Chapter we define Wigner current's velocity field, and we address the following question: When does the Wigner current obey Liouville's theorem on volume preservation? We are therefore looking to find for which cases the divergence of Wigner current's velocity field vanishes overall phase-space. We find that the Wigner current obeys Liouville's theorem only for potentials up to the second order in position, like for the quantum harmonic oscillator in Chapter 7 and for eigenfunctions of the Kerr oscillator in Chapter 8, or when the Wigner function approaches zero, like in very high temperatures of the thermal state [1], where the quantum correction terms ($l \geq 1$ in Eq. (4.16)), vanish.

6.1 Wigner Current's Velocity Field

Just like the Wigner current $\boldsymbol{J}$ is the quantum analogue of the classical phase-space current $\boldsymbol{j}$, the Wigner current velocity field $\boldsymbol{w}$ is the quantum analogue of the classical phase-space

velocity field $\boldsymbol{u}$ (see Chapter 2), which fulfils its own continuity equation [2, 30],

$$\partial_t W + W\boldsymbol{\nabla} \bullet \boldsymbol{w} + \boldsymbol{w} \bullet \boldsymbol{\nabla} W = 0 \ , \ \text{where } \boldsymbol{w} = \begin{pmatrix} w_x \\ w_p \end{pmatrix} = \frac{\boldsymbol{J}}{W} = \frac{1}{W}\begin{pmatrix} J_x \\ J_p \end{pmatrix} \ , \tag{6.1}$$

which, for the *total derivative*[1] of W, yields

$$\frac{D\,W}{Dt} = \partial_t W + \boldsymbol{w} \bullet \boldsymbol{\nabla} W = -W\boldsymbol{\nabla} \bullet \boldsymbol{w} \ . \tag{6.2}$$

Rearranging Eq. (6.2), the divergence of $\boldsymbol{w}$ takes the form

$$\boldsymbol{\nabla} \cdot \boldsymbol{w} = -\frac{\partial_t W + \boldsymbol{w} \cdot \boldsymbol{\nabla} W}{W} = -\frac{W\partial_t W + \boldsymbol{J} \cdot \boldsymbol{\nabla} W}{W^2} = \frac{W\boldsymbol{\nabla} \cdot \boldsymbol{J} - \boldsymbol{J} \cdot \boldsymbol{\nabla} W}{W^2} \ , \tag{6.3}$$

which is singular at zeros of W, since generally zeros of W do not coincide with zeros of its derivatives [27].

6.2 Liouvillian Wigner Current

If the total derivative of W in Eq. (6.2) is zero (assuming $W \neq 0$), the divergence of its velocity field $\boldsymbol{\nabla} \bullet \boldsymbol{w}$ must be zero overall phase-space. This implies that $\boldsymbol{w}$ obeys Liouville's theorem and that it can be written as the curl of a vector potential $\boldsymbol{A}$, $\boldsymbol{w} = \boldsymbol{\nabla} \times \boldsymbol{A}$ (see Chapter 2). For the quantum-mechanical $\boldsymbol{J}$ in Eq. (4.16), $\boldsymbol{w}$ in Eq. (6.1) becomes

$$\boldsymbol{w} = \begin{pmatrix} w_x \\ w_p \end{pmatrix} = \begin{pmatrix} \frac{p}{M} \\ \frac{J_p}{W} \end{pmatrix} \ \text{which implies } \boldsymbol{\nabla} \bullet \boldsymbol{w} = \partial_p w_p = \partial_p \left(\frac{J_p}{W} \right) \ , \tag{6.4}$$

which obeys Liouville's theorem only when $J_p = w_p(x)W$ where $w_p(x)$ is a function in x only. To determine the form of $w_p(x)$, one can substitute the integral form of J_p of Eq. (4.16), and taking projections in p on both sides, one finds

$$\begin{aligned} \int_{-\infty}^{\infty} J_p \, dp &= -\frac{1}{\pi\hbar} \iint_{-\infty}^{\infty} \left[\frac{V(x+y) - V(x-y)}{2y} \right] \Psi^*(x+y)\Psi(x-y) e^{\frac{2i}{\hbar} py} \, dy \, dp \\ &= -\int_{-\infty}^{\infty} \left[\frac{V(x+y) - V(x-y)}{2y} \right] \Psi^*(x+y)\Psi(x-y)\delta(y) \, dy \\ &= w_p(x) \int_{-\infty}^{\infty} W \, dp = -P(x,t)\frac{dV}{dx} = w_p(x)P(x,t) \ . \end{aligned} \tag{6.5}$$

This implies $w_p(x) = -\frac{dV}{dx}$. Thus, for $\boldsymbol{w}$ in Eq. (6.4), to obey Liouville's theorem,

$$\boldsymbol{J} = \begin{pmatrix} \frac{p}{M} W \\ -W\frac{dV}{dx} \end{pmatrix} \ \text{and} \ \boldsymbol{w} = \frac{\boldsymbol{J}}{W} = \begin{pmatrix} \frac{p}{M} \\ -\frac{dV}{dx} \end{pmatrix} \ , \tag{6.6}$$

reducing the associated continuity equation to the total derivative of W in Eq. (6.2),

$$\frac{D\,W}{Dt} = \partial_t W + \frac{p}{M}\partial_x W - \partial_x V \partial_p W = \partial_t W + \boldsymbol{w} \bullet \boldsymbol{\nabla} W = 0 \ . \tag{6.7}$$

[1] Also known as the derivative following the motion, comoving, material, convective, advective, substantive, substantial, Lagrangian, Stokes, particle, and hydrodynamic derivative.

From the infinite-sum form of J_p in Eq. (4.16), Eq. (6.6) is true only for the $l = 0$ term, i.e., when the quantum correction terms ($l \geq 1$) vanish. This is known to be true for the thermal state at infinitely high temperatures [1], for the quantum harmonic oscillator potential (see Chapter 7), and for eigenfunctions of the non-linear Kerr oscillator (see Chapter 8).

Due to its form, the zeros of $\boldsymbol{J}$'s components in Eq. (6.6) coincide with the zeros of W, apart from the x-axis ($p = 0$) and when the force is zero ($-\frac{dV}{dx} = 0$). This implies the formation of stagnation lines of $\boldsymbol{J}$ at the location of the zero lines of W, rendering $\boldsymbol{J}$'s components *degenerate*, i.e., $\boldsymbol{J}$ is governed by Hamilton's equations of motion (see Chapter 2).

Hereinafter, any reference to degenerate and semi-degenerate cases of the Wigner current, refers to the case of the zeros of J_x and J_p coinciding in phase-space (apart from the x- and p-axis). For the degenerate case this includes the zeros of W.

A quantum mechanical $\boldsymbol{w}$ which does not obey Liouville's theorem ($\boldsymbol{\nabla} \bullet \boldsymbol{w} \neq 0$ overall phase-space), its w_p component will have to assume a form which is inversely proportional to W as in Eq. (6.4). This implies that at the location of the zeros of W, $\boldsymbol{w}$ and its divergence will go to infinity (see Figs 8.1 and 6.1). As it was proven here, this only occurs in the presence of the quantum correction terms ($l \geq 1$ in Eq. (4.16)), otherwise only in their absence will $\boldsymbol{w}$ obey Liouville's theorem. This was missed by Daligault as in [41] was stated that:

> "*... the definition of [$\boldsymbol{J}$] has inherently some arbitrariness in the sense that [the continuity equation Eq. (4.15)] remains valid when a divergenceless field [$\delta\boldsymbol{J}$] is added to it, [$\partial_t W = -\boldsymbol{\nabla} \bullet (\boldsymbol{J} + \delta\boldsymbol{J}) = -\boldsymbol{\nabla} \bullet \boldsymbol{J}$]. It implies that for each suitable divergenceless field a trajectory method can be devised, which leads, in principle, to the exact distribution function [W]. One can, for example, wonder if [$\boldsymbol{J} + \delta\boldsymbol{J}$] exists, that would render Hamiltonian quantum fluid dynamics in phase space. This amounts to the existence of a divergecenless [$\delta\boldsymbol{J}$]...*" [41]

Given that we have proven here that the only divergence-less velocity field $\boldsymbol{w}$ is of the form in Eq. (6.6), Daligault in [41] is effectively referring to a $\delta\boldsymbol{J}$ which cancels the quantum correction terms ($l \geq 1$ in Eq. (4.16)). Therefore $\delta\boldsymbol{J}$ has to take the form

$$\delta\boldsymbol{J} = \begin{pmatrix} \delta J_x \\ \delta J_p \end{pmatrix} = \begin{pmatrix} 0 \\ + \sum_{l=1}^{\infty} \frac{(i\hbar/2)^{2l}}{(2l+1)!} \partial_p^{2l} W \partial_x^{2l+1} V \end{pmatrix} , \tag{6.8}$$

which is a *not* a divergence-less field ($\boldsymbol{\nabla} \bullet \delta\boldsymbol{J} = \partial_p \delta J_p \neq 0$), unless $\delta J_p = 0$. Thus, Daligault's attempt to "*render Hamiltonian quantum fluid dynamics in phase space*" in [41], is ill-defined.

6.3 Liouvillian Wigner Current for Eigenfunctions

In this Section we discuss the concept of *Wigner trajectories* [70] and *quantal force* [71], and show that these are unphysical.

Wigner Trajectories

For eigenfunctions, the Wigner function W in Eq. (4.1), is time-independent and therefore the continuity equation Eq. (4.15), takes the form

$$\boldsymbol{\nabla} \bullet \boldsymbol{J} = \partial_x J_x + \partial_p J_p = 0 \text{ (only true for eigenfunctions).} \tag{6.9}$$

This implies that $\boldsymbol{J}$ for eigenfunctions is a solenoidal vector field; it does not feature formation of vortices in the form of spirals (no expansion or contraction of the current in phase-space, see Figs. 7.3, and 9.3).

A divergence-less $\boldsymbol{J}$ does *not* imply a divergence-less $\boldsymbol{w}$, because, since for eigenfunctions $\partial_t W = 0$, the total derivative of W in Eq. (6.2) becomes

$$\frac{D\,W}{Dt} = \boldsymbol{w} \bullet \boldsymbol{\nabla} W = -W \boldsymbol{\nabla} \bullet \boldsymbol{w} \; . \tag{6.10}$$

Thus, for eigenfunctions of the quantum mechanical case, the velocity field $\boldsymbol{w}$ in Eq. (6.4) obeys Liouville's theorem ($\boldsymbol{\nabla} \bullet \boldsymbol{w} = 0$ overall phase-space) only when $\boldsymbol{w} \bullet \boldsymbol{\nabla} W = 0$, i.e., when $\boldsymbol{w}$ is perpendicular to the gradient of W. This occurs when the contours of W are collinear with $\boldsymbol{w}$'s streamlines. The condition imposed on $\boldsymbol{J}$ so that $\boldsymbol{w}$ obeys Liouville's theorem, was given in Eq. (6.6). As it was discussed, the implication of this condition is that the zeros of W coincide with the zeros of $\boldsymbol{J}$'s components, apart from the x-axis ($p = 0$) and when the force is zero ($-\frac{dV}{dx} = 0$). This implies the formation of stagnation lines of $\boldsymbol{J}$ at the location of the zero lines of W. Therefore, for any other form of the Wigner current $\boldsymbol{J}$ in Eq. (4.16), which are not of the simple form in Eq. (6.6), the contours of W are *not* collinear with $\boldsymbol{w}$'s streamlines, see Figs. 6.1 and 9.3. This statement is in contradiction with reference [70], where Lee and Scully consider energy eigenfunctions of the Morse oscillator. They seem to assume that $\frac{D\,W}{Dt} = 0$ as they argue:

> "*... the oscillator should remain in the same eigenstate throughout. In terms of the Wigner distribution, it means that each phase-space point should move in such a way that the Wigner distribution function does not change in time. This consideration leads to the concept of "Wigner trajectories," trajectories along which phase-space points of the Wigner distribution function move. For the case under consideration, Wigner trajectories must be trajectories along the surfaces on which the Wigner distribution function takes on the same value, i.e., trajectories along the equi-Wigner surfaces. These Wigner trajectories are "quantum-mechanical" trajectories in the sense that they represent paths of phase-space points that move according to the quantum-mechanical equation of motion*" [70]

Since the total derivative of W is not equal to zero (see Eq. (6.10), except for harmonic systems), Lee and Scully are wrong.

The concept of Wigner trajectories was also criticised [32, 41]. Specifically, Dittrich *et al.* consider it meaningless because their semi-classical integration method [32] did not produce 'Wigner trajectories'. They find their own semi-classical trajectories, starting from classical trajectories, when increasingly refined, at first approach the

> "*Wigner contour [...]. However, they do not approach it asymptotically but continue shifting further past the Wigner contour, indicating that it plays no particular role for quantum time evolution in phase space, not even of eigenstates.*"[32]

But Dittrich *et al.* did not disprove Lee and Scully's misconceptions.

Quantum Force

The concept of Wigner trajectories was also used for the introduction of the concept of "*quantal force*" by Razavy [71, 72] who incorrectly assumed that $\boldsymbol{\nabla} \bullet \boldsymbol{w} = 0$ for anharmonic potentials,

see Eq. (1) and (3) of [71]. Razavy defines $\dot{p} = F_n = -\partial_x V_{\text{eff}} = \frac{J_p}{\partial_p W}$ but this is wrong because according to Eq. (6.4), $\dot{p} = \frac{J_p}{W} \neq \frac{J_p}{\partial_p W}$ and generally $\boldsymbol{\nabla} \bullet \boldsymbol{w} \neq 0$ [27]. Only harmonic systems have a divergence-less velocity field, as discussed earlier in Section 6.2.

Inspired by the classical expression for $\boldsymbol{j}$ (see Chapter 2 and specifically Eq. (2.4)), one finds in the quantum case that

$$\boldsymbol{J} = \begin{pmatrix} J_x \\ J_p \\ 0 \end{pmatrix} = \begin{pmatrix} \partial_p \mathcal{Q} \\ -\partial_x \mathcal{Q} \\ 0 \end{pmatrix} = \boldsymbol{\nabla} \times \begin{pmatrix} 0 \\ 0 \\ \mathcal{Q} \end{pmatrix} \text{ where } \mathcal{Q} = \int_{-\infty}^{p} dp'\, J_x = -\int_{-\infty}^{x} dx'\, J_p \,, \tag{6.11}$$

Therefore, a quantum force can be defined as $\mathcal{F} = -\partial_x \mathcal{Q} = J_p$. Then, $\mathcal{Q}$ could be referred to as a quasi-Hamiltonian, but since it only applies to eigenfunctions this does not appear to be a useful concept.

For superpositions, where $\boldsymbol{\nabla} \bullet \boldsymbol{J} \neq 0$, Eq. (6.11) does not apply since it only applies in the case of $\boldsymbol{\nabla} \bullet \boldsymbol{J} = 0$. For superpositions, $\boldsymbol{J}$'s fieldline portraits feature formation of vortices in the form of spirals (expansion or contraction of the current in phase-space), see e.g. Fig. 9.11.

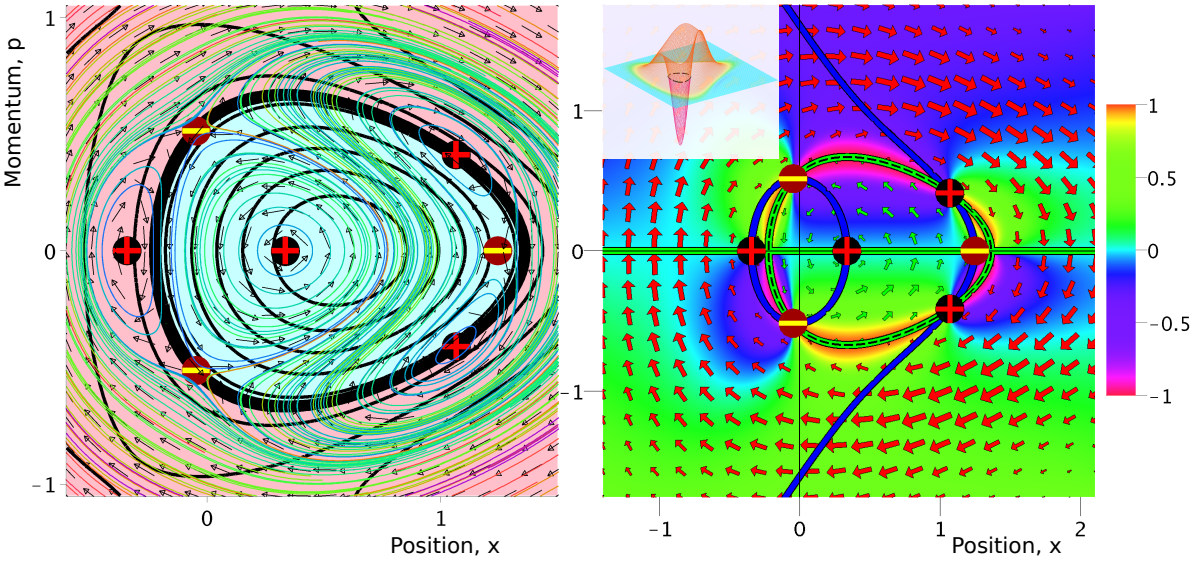

Figure 6.1 **Left panel:** Integrated fieldlines of $\boldsymbol{J}$ cross Wigner function contours. Thin coloured lines display fieldlines of $\boldsymbol{J}$, displayed together with normalized current $\boldsymbol{J}/||\boldsymbol{J}||$ (black arrows), and its stagnation points, for the same state as depicted on the right panel. W's zero contour, around the negative (light cyan-coloured) patch at the centre, is highlighted by a thick black line. Many fieldlines, for this first excited state, cut across the Wigner function's contours and enter and leave the negative area. **Right panel:** Singularities of $\boldsymbol{\nabla} \cdot \boldsymbol{w}$ coincide with zeros of W. $\boldsymbol{J}$ depicted by arrows (red for clockwise and green for inverted flow [4]), together with the zeros of the J_x and J_p components (green and blue lines, respectively), is superimposed on top of a colourplot of $\frac{2}{\pi} \arctan(\boldsymbol{\nabla} \cdot \boldsymbol{w})$. The inset shows the corresponding Wigner function for the first excited state of an anharmonic Morse oscillator [65] with potential $V(x) = 3(1 - \exp(-x/\sqrt{6}))^2$. The red crosses and yellow bars mark the locations of the current's stagnation points, with Poincaré-Hopf indices [4] $\omega = +1$ and -1. Parameters: $\hbar = 1$ and $M = 1$. The black dashed line marks the zero-contour of the Wigner function (compare inset), here the divergence $\boldsymbol{\nabla} \cdot \boldsymbol{w}$ is singular [27].

Instead, inspiration for the formulation of a quantum force in phase-space could be found in the hydrodynamic formulation of quantum mechanics, discussed in Chapter 3. As a reminder, in the hydrodynamic formulation of quantum mechanics, Erwin Madelung in 1927 [19] and independently David Bohm in 1952 [20], formulated the quantum force, as the total derivative of the momentum $p(x) = Mu(x)$. Similarly, one could write in phase-space, the rate of change of the quantum phase-space velocity field, as

$$\dot{\boldsymbol{w}} = \frac{d}{dt}\left(\frac{\boldsymbol{J}}{W}\right) = \begin{pmatrix} \frac{\dot{p}}{M} \\ \frac{d}{dt}\left(\frac{J_p}{W}\right) \end{pmatrix} \tag{6.12}$$

and introduce and quantum phase-space force, or call it Wigner force, as

$$\mathcal{F}_{\mathcal{W}} = M\dot{\boldsymbol{w}} = M\frac{d}{dt}\left(\frac{\boldsymbol{J}}{W}\right) = \begin{pmatrix} \dot{p} \\ M\frac{d}{dt}\left(\frac{J_p}{W}\right) \end{pmatrix} \tag{6.13}$$

Note that $\dot{p}$ in Eq. (6.13) is $\frac{J_p}{W}$, i.e. $J_p = \dot{p}W$. As a proof, we have already shown that the projection of the J_p component onto momentum space, is the probability current, $\tilde{j}(p) = \dot{p}P(p)$ in Eq. (4.23), where $\dot{p}$ is the force in momentum space.

7 Degenerate Wigner Current

The Wigner current is rendered degenerate for vanishing quantum correction terms, see Section 6.1. Examples include the classical limit of $\hbar \to 0$ [11], the thermal state at infinitely high temperatures [1], the quantum harmonic oscillator potential, and for eigenfunctions *only* of the non-linear Kerr oscillator (see Chapter 8). In this Chapter, we present, analyse and visualise the characteristics of quantum phase-space dynamics using the degenerate Wigner current of the quantum harmonic oscillator.

7.1 The Quantum Harmonic Oscillator

The features of the quantum harmonic oscillator's dynamics discussed in this Chapter, are used as a reference for comparison with the three classes of weakly-anharmonic oscillators discussed in Chapter 9. Therefore, for simplicity, we set the quantum harmonic oscillator's curvature (its spring constant), $\partial_x^2\left(\frac{kx^2}{2}\right) = k = M\Omega^2 = 1$ and angular frequency $\Omega = \frac{2\pi}{T} = 1$ (with oscillating period $T = 2\pi$). In this reference form, the quantum harmonic oscillator features *circular* (rather than elliptical [65]) fieldlines in both classical and quantum phase-space (see Figs. 9.1 and 7.3), since its velocity field assumes identical form (in both classical and quantum) as its dynamics are governed by Hamilton's equations of motion, see Section 7.3, which is not obvious from Schrödinger's equation [62].

The dynamics of the quantum harmonic oscillator are described by the time-independent Schrödinger equation of the form (with $\hbar = 1$ and state index $n = 0, 1, 2, \ldots$),

$$\hat{\mathcal{H}}^{\odot}\psi_n = \left[-\frac{1}{2}\frac{d^2}{dx^2} + \frac{\hat{x}^2}{2}\right]\psi_n = E_n\psi_n \,, \tag{7.1}$$

where $\hat{\mathcal{H}}^{\odot}$ is the quantum harmonic oscillator's Hamiltonian, and E_n and ψ_n are its corresponding eigenfunctions and eigenenergies (H_n are the Hermite polynomials of degree n),

$$\psi_n = \frac{1}{\sqrt{2^n n!}}\left(\frac{1}{\pi}\right)^{1/4} e^{-\frac{x^2}{2}} H_n\left(x\right), \; H_n(x) = (-1)^n e^{x^2}\frac{d^n}{dx^n}\left(e^{-x^2}\right), \; E_n = n + \frac{1}{2} \,. \tag{7.2}$$

7.2 The Quantum Harmonic Oscillator in Phase-Space

In phase-space, the quantum harmonic oscillator in its reference form (see Section 7.1), is described by its associated Wigner functions $W^{\odot}$ expressed as [8],

$$W^{\odot}_{mn} = \begin{cases} \sqrt{\frac{m!}{n!}}\frac{(-1)^m}{\pi}\left(4\mathcal{H}^{\odot}\right)^{(n-m)/2} L_m^{(n-m)}\left(4\mathcal{H}^{\odot}\right) e^{-2\mathcal{H}^{\odot}+i(m-n)\arctan\left(\frac{p}{x}\right)} & m \neq n \text{ for off-diagonal terms} \\ \\ \frac{(-1)^n}{\pi} L_n^{(0)}\left(4\mathcal{H}^{\odot}\right) e^{-2\mathcal{H}^{\odot}} & m = n \text{ for eigenfunctions} \end{cases} \tag{7.3}$$

where $\mathcal{H}^{\odot} = \frac{p^2}{2} + \frac{x^2}{2}$ and $L_m^{(n-m)}$ are the Laguerre polynomials, defined as

$$L_m^{(\alpha)}(x) = \frac{x^{-\alpha}e^x}{m!}\frac{d^m}{dx^m}\left(e^{-x}x^{m+\alpha}\right) \,. \tag{7.4}$$

Thus, the Wigner transform (see Section 4.1) maps the Hermite polynomials of the eigenfunctions of the quantum harmonic oscillator in Eq. (7.2), to the Laguerre polynomials of its associated Wigner functions in Eq. (7.3).

The Wigner functions of the eigenfunctions of the quantum harmonic oscillator in Eq. (7.3), have the shape of concentric fringes of alternating polarity (ripples in phase-space) centred on the origin of phase-space, see Fig. 7.1. Their zero lines thus form concentric circles [11] (n circles for the Wigner function of the nth excited state, which also has n nodes), with the exception of the Wigner function of the ground state which does not go to zero, as it is a Gaussian [64]. The radii of these concentric circles of the Wigner functions $W^{\odot}_{nn}$ in Eq. (7.3), for the first, second and third excited states, are indicated in Table 7.1. The trend of these radii including the radii of higher excited states, is illustrated together with the trend of the nodes of the corresponding eigenfunctions, for the first ten excited states, in Fig. 7.1.

	$k=1$	$k=2$	$k=3$
$W^{\odot}_{33}$	$\sqrt{\frac{3}{2}+\sqrt{3}\cos\left(\frac{1}{3}\arctan(\sqrt{2})-\frac{4\pi}{3}\right)}$	$\sqrt{\frac{3}{2}+\sqrt{3}\cos\left(\frac{1}{3}\arctan(\sqrt{2})-\frac{2\pi}{3}\right)}$	$\sqrt{\frac{3}{2}+\sqrt{3}\cos\left(\frac{1}{3}\arctan(\sqrt{2})\right)}$
$W^{\odot}_{22}$	$\sqrt{1-\frac{1}{\sqrt{2}}}$	$\sqrt{1+\frac{1}{\sqrt{2}}}$	-
$W^{\odot}_{11}$	$\frac{1}{\sqrt{2}}$	-	-

Table 7.1 Radii of the kth zero circle (where $k=1$ represents the first zero circle from the origin) of the quantum harmonic oscillator's Wigner functions for the first, second and third excited states. These are effectively the roots of the Laguerre polynomials $L_n^{(0)}\left(2x^2\right)$ in Eq. (7.4), for which a general closed form expression is not known [73].

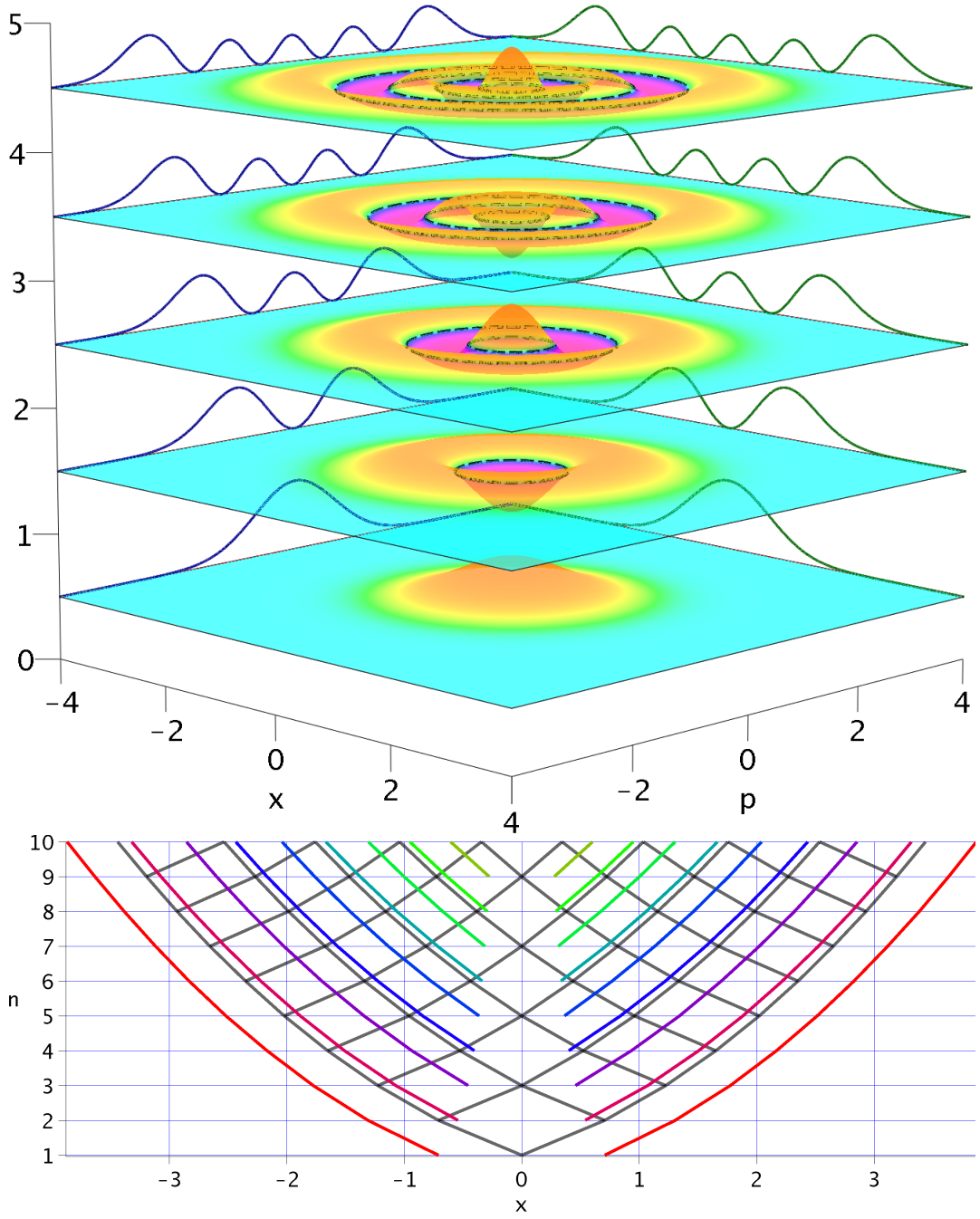

Figure 7.1 **Top panel:** Wigner functions for $n = 0, 1, 2, 3, 4$ in Eq (7.3), shifted upwards according their energy eigenvalue. Green and blue lines are their projections onto (probability distributions) the x and p axes, see Eqs. (3.22) and (3.23). Dashed black lines indicate the zero circles of the Wigner functions.
Bottom panel: Coloured lines represent the trend of the numerically determined roots of the Laguerre polynomials $L_n^{(0)}\left(2x^2\right)$ in Eq. (7.4) (compare with Table. 7.1), and grey lines represent the roots of the Hermite polynomials $H_n(x)$ in Eq. (7.2), for $n = 1, 2, 3, \ldots, 10$ (vertical axis). Note that the roots are only true for non-negative integer values of n; solid lines only depict the trend.

For the superposition of the ground and first excited state $\Psi_{0,1}$ in Eq. (3.8) the corresponding Wigner function in Eq. (4.9) takes the form

$$W_{0,1}^{\odot} = \frac{e^{-p^2-x^2}}{\pi}\left[\cos(2\theta) + \sin^2(\theta)\left(2p^2+2x^2\right) + \sin(2\theta)\sqrt{2}\left(x\cos(t) - p\sin(t)\right)\right] . \tag{7.5}$$

It has a circular zero line with radius $\frac{1}{\sqrt{2}}$ and centre $\left(-\frac{1}{\sqrt{2}}\cos(t)\cot(\theta), \frac{1}{\sqrt{2}}\sin(t)\cot(\theta)\right)$, which is further displaced from the origin the larger the ground state contribution ($\theta \to 0$, see top row of Fig. 7.2), and rotates around the origin with period $T = 2\pi$. During a full rotation, the Wigner function remains unchanged, since its total derivative is zero. It is also exhibits a rigid-body rotation since its associated velocity field is of the form in Eq. (7.7) implying that every value of $W_{0,1}^{\odot}$ in phase-space rotates with the same period, see Sections 7.3. This is also true for any superposition of the quantum harmonic oscillator.

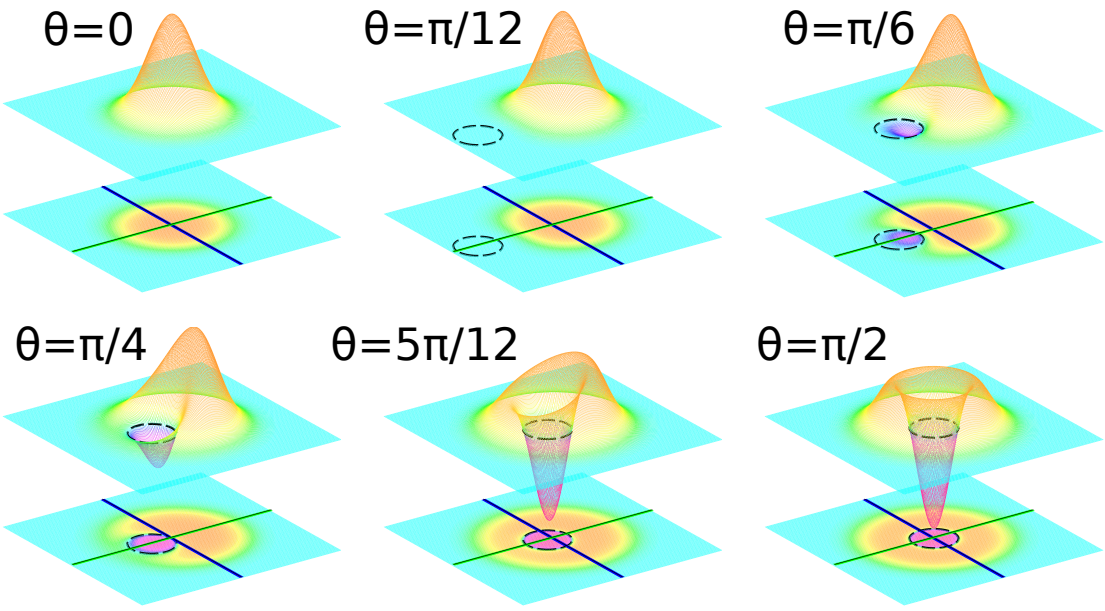

Figure 7.2 Wigner functions of the superposition of the ground and first excited state $W_{0,1}^{\odot}$ in Eq. (8.3) for a weighting angle θ. Green and blue lines indicate the x- and p-axes, respectively. Dashed black lines indicate the zero circles of the Wigner functions. By increasing the weighting angle θ, the zero circle of the Wigner function propagates from infinity towards the origin of phase-space. In the case of a superposition of two states, other than the superposition of the ground and first excited state, the corresponding Wigner functions do not generally form zeros *circles* but other zero lines of non-trivial shapes in phase-space.

7.3 The Quantum Harmonic Oscillator's Dynamics in Phase-Space

The Wigner functions of the quantum harmonic oscillator fulfil the equation

$$\partial_t W^{\odot} + p\partial_x W^{\odot} - x\partial_p W^{\odot} = \partial_t W^{\odot} + \boldsymbol{\nabla} \bullet \boldsymbol{J} = \partial_t W^{\odot} + \boldsymbol{w} \bullet \boldsymbol{\nabla} W^{\odot} \tag{7.6}$$

which has a classical form as it governed by Hamilton's equations of motion (see Chapter 2). Eq. (7.6) is derived by substituting $\mathcal{H}^{\odot} = \frac{p^2}{2} + \frac{x^2}{2}$ (the Cartesian form of the Hamiltonian in Eq. (7.1), with spring constant $k = M\Omega^2 = 1$ and angular frequency $\Omega = 1$), into Eq. (4.13).

The dynamics in phase-space of the quantum harmonic oscillator are governed by Hamilton's equations of motion, since it contains terms up to the second order in position [11], and therefore the quantum Liouville equation assumes the form in Eq. (6.7), featuring the degenerate Wigner current and its associated divergence-free velocity field in Eq. (6.6), discussed in Section 6.1. This behaviour of the quantum harmonic oscillator's dynamics, following Hamilton's equations of motion, is not obvious from Schrödinger's equation [62].

For the quantum harmonic oscillator in its reference form described in Section 7.1, the Wigner current and its associated velocity field in Eq. (6.6), take the form

$$\boldsymbol{J}^{\odot} = \begin{pmatrix} J_x \\ J_p \end{pmatrix} = W^{\odot} \begin{pmatrix} p \\ -x \end{pmatrix} \text{ and } \boldsymbol{w}^{\odot} = \begin{pmatrix} p \\ -x \end{pmatrix} = \begin{pmatrix} \partial_p \mathcal{H}^{\odot} \\ -\partial_x \mathcal{H}^{\odot} \end{pmatrix} , \tag{7.7}$$

where $\mathcal{H}^{\odot} = \frac{p^2}{2} + \frac{x^2}{2}$ is the quantum harmonic oscillator's classical Hamiltonian in this reference form. The Wigner current $\boldsymbol{J}^{\odot}$ and its velocity field $\boldsymbol{w}^{\odot}$ in Eq. (7.7), feature circular field lines and streamlines, respectively, in both classical and quantum phase portraits (see Figs. 9.1 and 7.3), thus the use of the symbol '$\odot$' in Eq. (7.7). The zero lines of the Wigner function $W^{\odot}$ in Eq. (7.7), discussed in Section 7.2, are lines of zero for both components of its associated Wigner current, giving rise to lines of stagnation of the current, see Fig. 7.3. This degeneracy is lifted for superpositions *only* of the Kerr-type oscillator discussed in Chapter 8 due to the presence of higher order terms in $\boldsymbol{J}$. The same applies and it is generally true (i.e. not limited to superpositions), for anharmonic potentials discussed in Chapter 9. Using trajectories, which in this case follow the classical equations of motion, is in fact simpler and, in this sense, even superior to Schrödinger wave function propagators, see [15] p. 352.

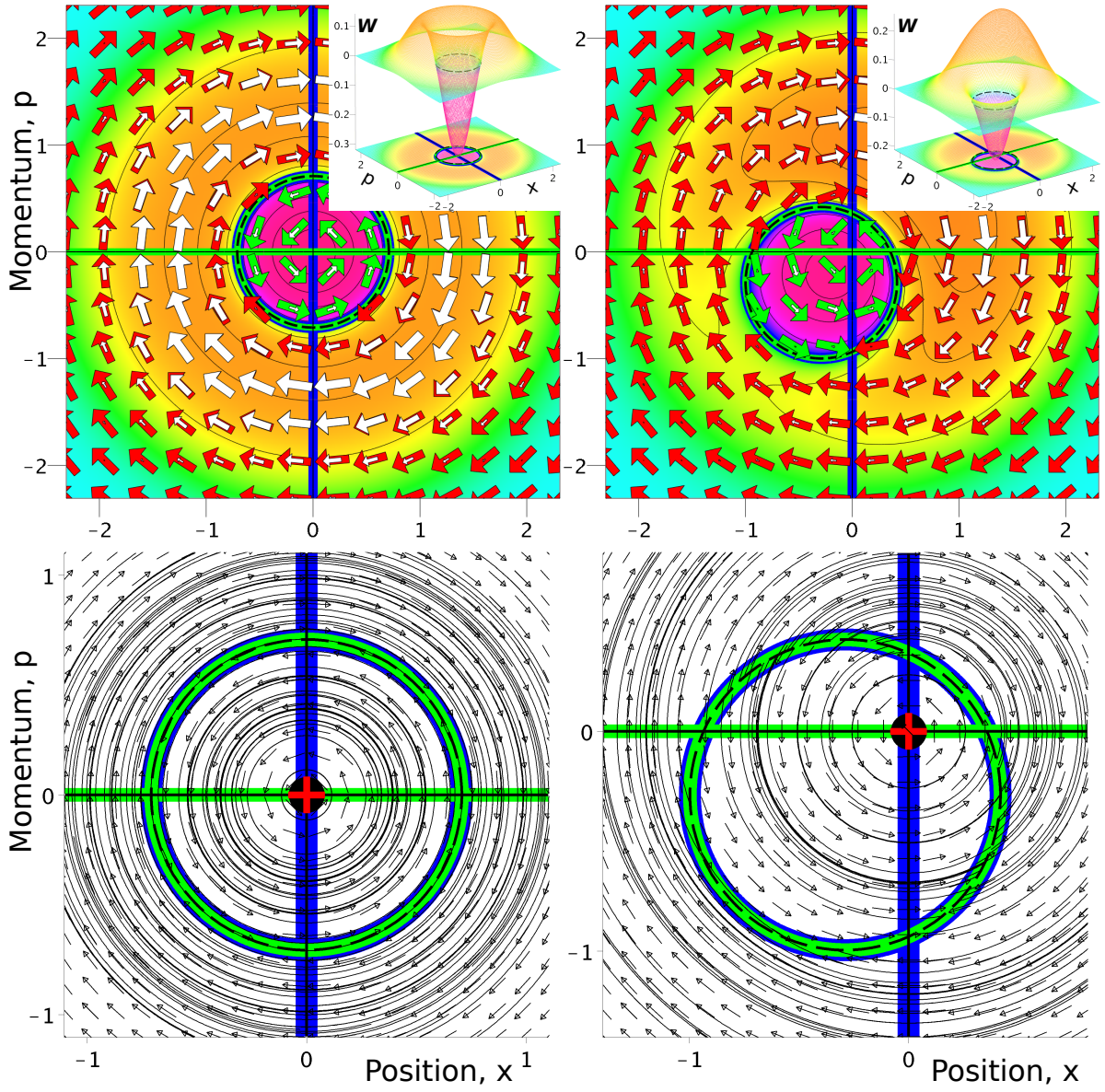

Figure 7.3 **Top row:** Wigner current and Wigner functions for the quantum harmonic oscillator's (in its reference form, discussed in Section 7.1) first excited state ψ_1 (left) and superposition state $\Psi^{\odot}_{0,1}(\frac{7T}{8};\frac{\pi}{3})$ (right). Background colouring refers to the respective Wigner functions' values (compare insets). The normalised Wigner current $\boldsymbol{J}/|\boldsymbol{J}|$ is depicted with red arrows if the Wigner function values are positive. For negative Wigner function values green arrows are used, demonstrating *current reversal* [4]. White arrows on top of $\boldsymbol{J}/|\boldsymbol{J}|$ depict $\boldsymbol{J}$.
Bottom row: Corresponding field lines of the Wigner current $\boldsymbol{J}^{\odot}$ in Eq. (7.7) at a fixed time t. The initial points of the field lines are the randomly picked, small black dots. At these initial points the local magnitude of the Wigner current is determined and the field line it lies on gets coloured accordingly: we chose the colours of the rainbow; red represents relatively strong current ("hot") over yellow, green to blue representing weak current ("cold"). The stagnation point at the origin carries an orientation winding number $\omega = +1$ and is labelled as in Fig. 2.2. Dashed black circles show the locations of $W^{\odot} = 0$ which implies that, there $J_x = 0$ and $J_p = 0$ in Eq. (7.7). These dashed black lines constitute circular *current stagnation lines* with constant radius of $\frac{1}{\sqrt{2}}$ and centred on $\left(-\frac{1}{\sqrt{2}}\cos(t)\cot(\theta), \frac{1}{\sqrt{2}}\sin(t)\cot(\theta)\right)$.

8 Semi-Degenerate Wigner Current

In Chapter 7 we discussed one of the cases of a degenerate Wigner current, of the quantum harmonic oscillator. For conservative systems, the quantum harmonic oscillator will exhibit this degeneracy for eigenfunctions and superposition states. In this Chapter we discuss the case of a semi-degenerate Wigner current of the non-linear Kerr oscillator. For eigenfunctions, due to the symmetry of the non-linear Kerr oscillator, the quantum correction terms vanish, and its Wigner current and associated velocity field assume the form in Eq. (6.6), whereas for a superposition state this degeneracy is lifted as the quantum correction terms remain.

8.1 The Non-Linear Kerr Oscillator

The dynamics of the non-linear Kerr oscillator are described by the time-independent Schrödinger equation of the form (with $\hbar = 1$ and state index $n = 0, 1, 2, \ldots$),

$$\hat{\mathcal{H}}^{\mathcal{K}}\psi_n = \left[-\frac{1}{2}\frac{d^2}{dx^2} + \frac{\hat{x}^2}{2} + \Lambda^2\left(-\frac{1}{2}\frac{d^2}{dx^2} + \frac{\hat{x}^2}{2}\right)^2\right]\psi_n = E_n^{\mathcal{K}}\psi_n \,, \tag{8.1}$$

where $\hat{\mathcal{H}}^{\mathcal{K}}$ is the Kerr oscillator's Hamiltonian, whose wave function solutions are the quantum harmonic oscillator's eigenfunctions ψ_n given in Eq. (7.2), with eigenenergies of the form

$$E_n^{\mathcal{K}} = E_n + \Lambda^2 E_n^2 = \left(n + \frac{1}{2}\right) + \Lambda^2\left(n + \frac{1}{2}\right)^2 \,. \tag{8.2}$$

In Eq. (8.1), Λ^2 is proportional to $\chi^{(3)}$, which is the third-order nonlinear susceptibility [55, 74]. Note that we have also set $M = 1$ and $k = 1$ in Eq. (8.1), as with the reference form of the quantum harmonic oscillator in Chapter 7.

8.2 The Non-Linear Kerr Oscillator in Phase-Space

In phase-space the Kerr oscillator is described by the Wigner functions given in Eq. (7.3), which are also the quantum harmonic oscillator's Wigner functions, but for the two-state superposition in Eq. (8.3), the Kerr oscillator's Wigner functions take the form

$$W_{0,1}^{\mathcal{K}} = \frac{e^{-p^2-x^2}}{\pi}\left[\cos(2\theta) + \sin^2(\theta)\left(2p^2 + 2x^2\right) + \sin(2\theta)\sqrt{2}\left(x\cos(t + 2\Lambda^2 t) - p\sin(t + 2\Lambda^2 t)\right)\right] \,. \tag{8.3}$$

$$\frac{\hat{p}^2}{2M} + \frac{k}{2}\hat{x}^2 + \Lambda^2\left(\frac{\hat{p}^2}{2M} + \frac{k}{2}\hat{x}^2\right)^2 = \frac{\hat{p}^2}{2} + \frac{\hat{x}^2}{2} + \Lambda^2\left(\frac{\hat{p}^2}{2} + \frac{\hat{x}^2}{2}\right)^2 \,, \tag{8.4}$$

8.3 The Non-Linear Kerr Oscillator's Dynamics in Phase Space

The continuity equation Eq. (4.15) for the non-linear Kerr-type oscillator can be derived by substituting its Hamiltonian $\hat{\mathcal{H}}^{\mathcal{K}}$ in Eq. (8.4), into Eq. (4.13), to take the form (with $\hbar = 1$) [1],

$$\partial_t W + p\left[1 + \Lambda^2\left(p^2 + x^2 - \frac{1}{4}\boldsymbol{\Delta}\right)\right]\partial_x W - x\left[1 + \Lambda^2\left(p^2 + x^2 - \frac{1}{4}\boldsymbol{\Delta}\right)\right]\partial_p W = 0\,. \tag{8.5}$$

Comparing Eqs. (4.15) and (8.5), the corresponding Wigner current $\boldsymbol{J}$ takes the form,

$$\boldsymbol{J} = \begin{pmatrix} J_x = p\left[1 + \Lambda^2\left(p^2 + x^2 - \frac{1}{4}\boldsymbol{\Delta}\right)\right]W \\ J_p = -x\left[1 + \Lambda^2\left(p^2 + x^2 - \frac{1}{4}\boldsymbol{\Delta}\right)\right]W \end{pmatrix} = \begin{pmatrix} p \\ -x \end{pmatrix}\left[1 + \Lambda^2\left(p^2 + x^2 - \frac{1}{4}\boldsymbol{\Delta}\right)\right]W\,, \tag{8.6}$$

The quantum harmonic oscillator's Wigner functions are also solutions to the non-linear Kerr oscillator Hamiltonian $\hat{\mathcal{H}}^{\mathcal{K}}$ in Eq. (8.4), and so for eigenfunctions, due to their symmetry, Eq. (8.7) becomes

$$\boldsymbol{J} = \begin{pmatrix} J_x = p\left[1 + \Lambda^2(2n+1)\right]W_{nn} \\ J_p = -x\left[1 + \Lambda^2(2n+1)\right]W_{nn} \end{pmatrix} = \begin{pmatrix} p \\ -x \end{pmatrix}\left[1 + \Lambda^2(2n+1)\right]W_{nn}\,. \tag{8.7}$$

Therefore, the corresponding velocity field takes the form,

$$\boldsymbol{w} = \begin{pmatrix} w_x = p\left[1 + \Lambda^2\right] \\ w_p = -x\left[1 + \Lambda^2\right] \end{pmatrix} = \begin{pmatrix} p \\ -x \end{pmatrix}\left[1 + \Lambda^2(2n+1)\right]\,, \tag{8.8}$$

which is divergence-less ($\boldsymbol{\nabla} \bullet \boldsymbol{w} = 0$). For superposition state the $\boldsymbol{\nabla} \bullet \boldsymbol{w}$ is typically non-zero, see Fig. 8.1.

[1] $\boldsymbol{\Delta} = \boldsymbol{\nabla} \bullet \boldsymbol{\nabla} = \partial_x^2 + \partial_p^2$ is the Laplace operator in phase-space

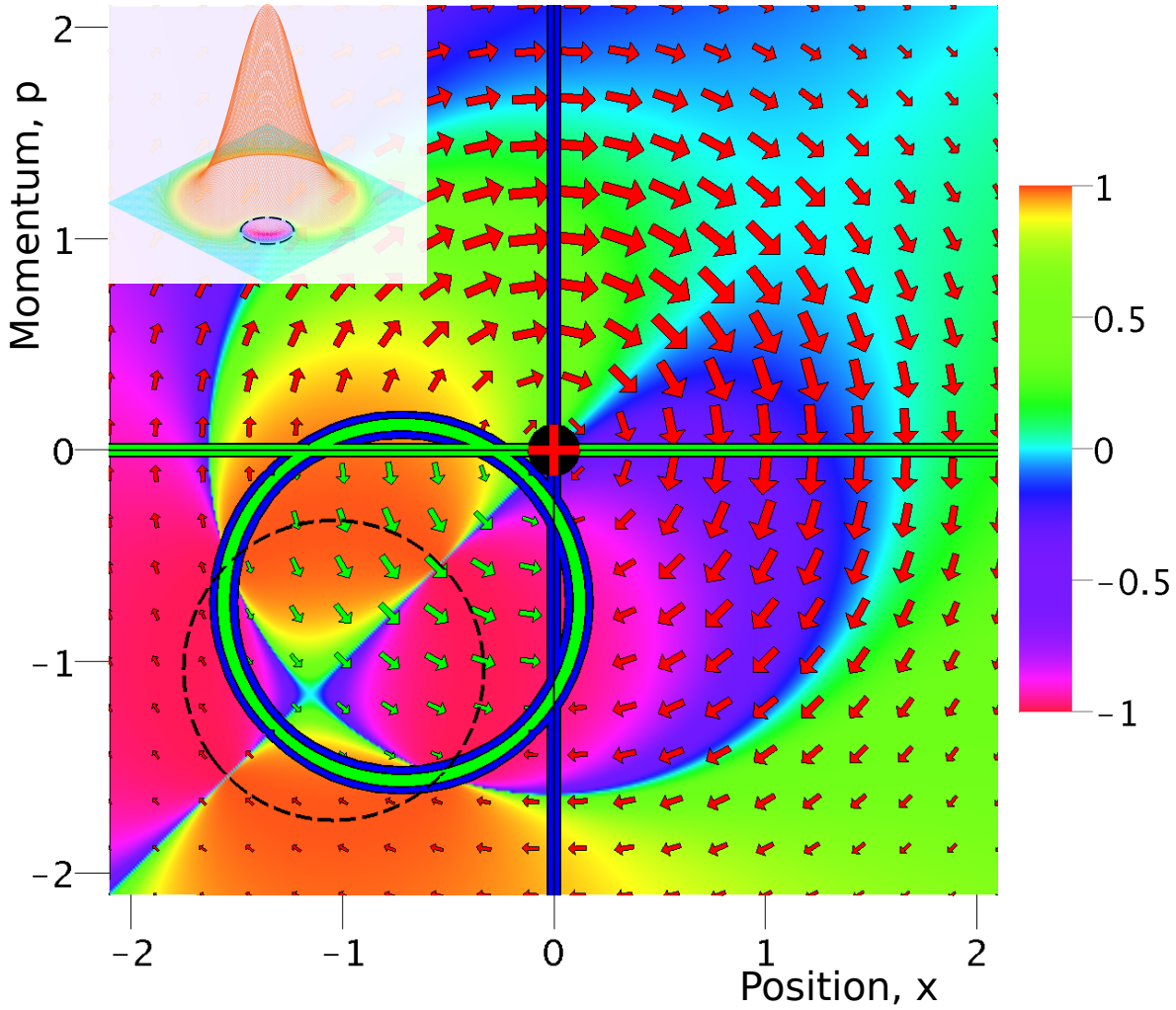

Figure 8.1 Wigner current $\boldsymbol{J}$, depicted by arrows (red for clockwise and green for inverted current), together with the zeros of the J_x and J_p components (green and blue lines, respectively), is superimposed on top of a colourplot of $\frac{2}{\pi}\arctan(\boldsymbol{\nabla}\bullet\boldsymbol{w})$. Parameters: $\hbar = 1$, $M = 1$, and $k = 1$. Superposition state $\Psi = \cos(\frac{\pi}{7})\psi_0 + \sin(\frac{\pi}{7})e^{-i\frac{7}{4}\pi}\psi_1$, for the Kerr oscillator with $\Lambda = 2$, features blue and green lines lying on top of each other. The zeros of the J_x and J_p components form degenerate lines of vanishing current.

9 Non-Degenerate Wigner Current

So far, in terms of the Wigner current, we discussed the degenerate case of the quantum harmonic oscillator (see Chapter 7), and the semi-degenerate case of the non-linear Kerr oscillator (see Chapter 8). In this Chapter, we discuss the quantum-mechanical case of weakly-anharmonic potentials, featuring a non-degenerate Wigner current. We only consider their bound weakly-excited eigenfunctions (see Section 9.3) and their pure two-state superpositions (Section 9.4).

Specifically, we investigate the features of $\boldsymbol{J}$'s fieldline portraits that are in common for the three classes of weakly-anharmonic potentials, defined here as *hard*, *soft* and *odd*, and find that odd potentials are hybrids of hard and soft potentials (see Sections 9.3 and 9.4). We particularly stress an intuitive understanding of the existence of their Wigner current fieldline portraits, which we subsequently formalise in a perturbation analysis (see Section 9.4 and 9.3). Because of weak anharmonicities, these three classes can partly be understood from the vantage point of the quantum harmonic oscillator (see Chapter 7), and partly through the perturbation analysis. This perturbation analysis is different to the usual perturbation analysis in quantum mechanics. Namely, here we perturb the potentials only, *not* their eigenfunctions. The eigenfunctions of the potential are the exact solutions of the full potential.

To demonstrate the conceptual power of the use of $\boldsymbol{J}$, and collections of its fieldlines, we show that in the limit of vanishing anharmonicity the fieldlines of $\boldsymbol{J}$ do not converge pointwise (see Sections 9.3 and 9.4) to those of the quantum harmonic oscillator. This implies that even for weakly anharmonic potentials, quantum and classical phase-space behaviour are qualitatively very different from each other (see Section 6.1 and also [5, 27]); this finding is at variance with common assumptions found in the literature

9.1 Three Classes of Weakly Anharmonic Potentials

Weakly anharmonic potentials $V^{\mathcal{A}}$ that can be Taylor expanded, are characterised by their leading anharmonicity coefficient $\alpha_\nu^{\mathcal{A}}$ in what we will refer to as their *truncation* $V_\nu^{\mathcal{A}}$ of order ν and representative $\mathcal{A}$, namely,

$$V^{\mathcal{A}}(x) \approx V_\nu^{\mathcal{A}}(x) = \frac{x^2}{2} + \alpha_\nu^{\mathcal{A}} x^\nu \,, \tag{9.1}$$

We equate the curvature of all weakly anharmonic potentials, at their minimum point (set for all potentials at $x = 0$), to the curvature (spring constant $k = 1$) of the quantum harmonic oscillator in its reference form in Chapter 7, $\partial_x^2 \left(V^{\mathcal{A}}(x)\right)\big|_{x=0} = k = 1$, see Table 9.1. As it was discussed in Section 7.1, this helps comparing the phase-space trajectories of the quantum harmonic oscillator with the trajectories of weakly anharmonic potentials, see Fig. 9.1.

The precise order ν of a truncation's leading anharmonic coefficient $\alpha_\nu^{\mathcal{A}}$ in Eq. (9.1), is quite unimportant, as it is the qualitative class of the potential that determines its qualitative dynamic features. With respect to Wigner current's qualitative features for weakly-anharmonic bound-state potentials, just as for the associated phase portraits in the classical case (see Fig. 9.1), only three classes of weakly anharmonic potentials exist. For each class a representative exists for which all bound eigenfunctions and eigenenergies are known in simple closed form, derived using supersymmetric quantum mechanics, see Section 3.6. As

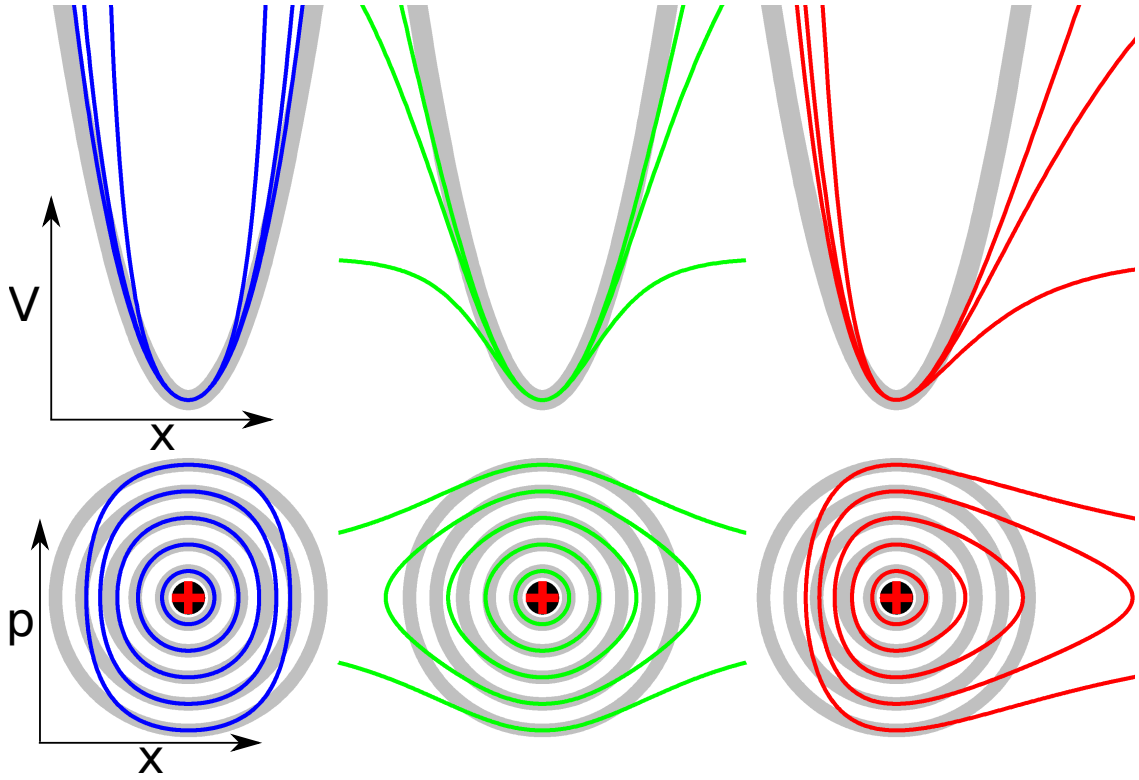

Figure 9.1 **Top row:** Representatives of the three classes of weakly-anharmonic potentials displayed side by side: Eckart potentials ($V^{\mathcal{E}}$, left, in blue) are hard, Rosen-Morse potentials ($V^{\mathcal{R}}$, centre, in green) are soft and Morse potentials ($V^{\mathcal{M}}$, right, in red) are odd, see Table 9.1. The potentials feature differing amounts of anharmonicity, $\alpha_\nu^{\mathcal{A}}$ in Eq. (9.1), while they are all rescaled to have the same curvature at their minimum point as the quantum harmonic oscillator potential in its reference form (see Chapter 7), displayed behind each class as a thick grey line. **Bottom row:** Associated classical phase portraits (for one fixed potential strength in each column), superimposed on quantum harmonic oscillator's phase portraits (thick grey lines). The stagnation point at the origin of each phase portrait carries a flow orientation winding number $\omega = +1$ and is labelled as in Fig. 2.2.

such representatives, denoted by their respective superscripts ($\mathcal{A}$) in Eq. (9.1), we chose the *hard* Eckart ($V^{\mathcal{E}}$) potential, representing all potentials with a *positive* leading anharmonic coefficient $\alpha_\nu^{\mathcal{A}}$ of even order ν, the *soft* Rosen-Morse ($V^{\mathcal{R}}$) potential, representing all potentials with a *negative* leading anharmonic coefficient of even order, and the *odd* Morse ($V^{\mathcal{M}}$) potential, representing all potentials with a leading anharmonic coefficient of odd order, see Table 9.1.

Each class has, qualitatively, similar phase portraits, (see Fig. 9.1). The hard and soft classes correspond to springs harder and softer (in terms of their spring constant), than the quantum harmonic oscillator in its reference form in Eq. (7.1), see left and middle columns of Fig. 9.1, respectively. For odd potentials we always set the leading coefficient $\alpha_\nu^{\mathcal{M}} < 0$, making the odd potentials soft for $x > 0$ and hard for $x < 0$, see right column of Fig. 9.1.

Potentials $V^{\mathcal{A}}$, which, based on their truncation $V_\nu^{\mathcal{A}}$, are classed as even or odd, can contain higher order Taylor terms which are not necessarily only even or odd. The influence of such higher terms can be neglected since we limit our investigation to weakly excited systems. If

Potential	Harmonic Oscillator	hard Eckart	soft Rosen-Morse	odd Morse
$V^{\mathcal{A}}(x)$	$\frac{x^2}{2}$	$V^{\mathcal{E}} = D\tan^2\left(\frac{x}{\sqrt{2D}}\right)$	$V^{\mathcal{R}} = D\tanh^2\left(\frac{x}{\sqrt{2D}}\right)$	$V^{\mathcal{M}} = D\left(1-e^{-\frac{x}{\sqrt{2D}}}\right)^2$
$V^{\mathcal{A}}_\nu = \frac{x^2}{2} + \alpha^{\mathcal{A}}_\nu x^\nu$	$\frac{x^2}{2}$	$V^{\mathcal{E}}_4 = \frac{x^2}{2} + \frac{x^4}{6D}$	$V^{\mathcal{R}}_4 = \frac{x^2}{2} - \frac{x^4}{6D}$	$V^{\mathcal{M}}_3 = \frac{x^2}{2} - \frac{x^3}{2\sqrt{2D}}$
Eigenenergies	$n+\frac{1}{2}$	$D\left[\left(\frac{\sqrt{1+16D^2}+2n+1}{4D}\right)^2 - 1\right]$	$D\left[1-\left(\frac{\sqrt{1+16D^2}-2n-1}{4D}\right)^2\right]$	$D\left[1-\left(\frac{4D-2n-1}{4D}\right)^2\right]$
Groundstate (unnormalized)	$e^{-\frac{x^2}{2}}$	$\cos\left(\frac{x}{\sqrt{2D}}\right)^{\left[\frac{\sqrt{1+16D^2}+1}{2}\right]}$	$\operatorname{sech}\left(\frac{x}{\sqrt{2D}}\right)^{\left[\frac{\sqrt{1+16D^2}-1}{2}\right]}$	$e^{-\left[x\left(\frac{4D-1}{2\sqrt{2D}}\right)+2De^{-\frac{x}{\sqrt{2D}}}\right]}$
D-parameter	-	$D>0$	$D>\sqrt{\left(\frac{2N-1}{4}\right)^2-\frac{1}{16}}$	$D>\frac{2N-1}{4}$
N-bound states	-	-	$N(D)=\left\lfloor\frac{\sqrt{1+16D^2}+1}{2}\right\rfloor$	$N(D)=\left\lfloor\frac{4D+1}{2}\right\rfloor$
A	-	$\frac{\sqrt{1+16D^2}+1}{4\sqrt{D}}$	$\frac{\sqrt{1+16D^2}-1}{4\sqrt{D}}$	$\frac{4D-1}{4\sqrt{D}}$
B	0	0	0	$\sqrt{D}$
α	-	$\frac{1}{\sqrt{2D}}$	$\frac{1}{\sqrt{2D}}$	$\frac{1}{\sqrt{2D}}$

Table 9.1 Revised version of Table 3.1 presenting the quantum harmonic oscillator and the three classes of weakly anharmonic potentials with their corresponding eigenenergies and groundstate ($n=0$). The inverse anharmonicity parameter D, for which $\lim_{D\to\infty} V^{\mathcal{E},\mathcal{R},\mathcal{M}} = \frac{x^2}{2}$, is also the depth of the two open potentials, Rosen-Morse and Morse. The number of bound sates N is given in terms of D, where $\lfloor\ldots\rfloor$ denotes floor rounding. Excited eigenfunctions ($n=1,2,\ldots,N-1$) for each potential are created using supersymmetric quantum mechanics (see Section 3.6), using their respective parameters given in the last three rows. The potentials here are shifted upwards, compared to Table 3.1, by an amount equal to the groundstate eigenenergy so that their minimum point is located on the x-axis.

we were to regard the truncated right hand side of Eq. (9.1), as the full potential, soft and odd potentials would obviously be *entirely* open (i.e. not only open above a certain potential energy, like the Rosen-Morse and Morse potentials, see Fig. 9.1), without any bound eigenfunctions; we exclude such cases. With these provisions, studying one representative of each class allows us to cover qualitative features of the Wigner current of the bound eigenfunctions of *all* weakly-excited weakly-anharmonic potentials.

We only consider two-state superpositions $\Psi^{\mathcal{A}}_{m,n}$ of the form in Eq. (3.8), where the associated revolution time describing the periodic movement in phase-space is given by Eq. (3.6).

9.2 The Wigner Functions of the Morse Potential

The Morse potential is one of the few bound-state systems for which an analytical expression of the Wigner function in Eq. (4.1), is known. Others include the quantum harmonic oscillator in Eq. (7.3), the infinite square well (and other similar piecewise constant potentials).

The eigenfunctions of the Morse potential [65], are

$$\psi^{\mathcal{M}}_n(x) = \frac{1}{\sqrt[4]{2D}}\mathcal{N}(D,n)\xi^{2D-n-1/2}e^{-\xi/2}L_n^{(4D-2n-1)}(\xi) \text{ for } \xi = 4De^{-x/\sqrt{2D}}\,, \tag{9.2}$$

where $L_n^{(\alpha)}$ are the Laguerre polynomials in Eq. (7.4), and $\mathcal{N}$ is normalisation constant

$$\mathcal{N}(D,n) = \sqrt{\frac{(4D-2n-1)\,\Gamma(n+1)}{\Gamma(4D-n)}}\,. \tag{9.3}$$

The corresponding Wigner functions (for all diagonal and off-diagonal density matrix entries), also derived in [65], are

$$W_{mn}(x,p;D) = \frac{2}{\pi}\mathcal{N}(D,m)\mathcal{N}(D,n)\xi^{4D-m-n-1} \times \sum_{r=0}^{m}\sum_{s=0}^{n} b(D,m;r)b(D,n;s)\xi^{r+s}K_{m-n-r+s+2ip\sqrt{2D}}(\xi) \tag{9.4}$$

where the b coefficient is of the form,

$$b(D,n;j) = \frac{(-1)^j}{j!}\frac{\Gamma(4D-n)}{\Gamma(4D-2n+j)\,\Gamma(n-j+1)}\,, \tag{9.5}$$

and K_ν is the modified Bessel function of the second kind [75] (formerly known as the modified Bessel function of the third kind [65]),

$$K_\nu(\xi) = \int_0^\infty \frac{\tau^{\nu-1}}{2} e^{-\frac{\xi}{2}\left(\tau+\frac{1}{\tau}\right)} d\tau\,, \tag{9.6}$$

which renders analytical calculations not much easier than numerical calculations [65], and we only used them to check some of the numerical results, see Chapter 5.

9.3 Wigner Current Fieldine Portraits for Eigenfunctions

Heisenberg's uncertainty principle $\Delta x \cdot \Delta p_x \geq \hbar/2$ implies constancy of the size of an uncertainty domain in phase-space [25] (note that this argument must not be taken too far [6]). For the Wigner current fieldline portraits for eigenfunctions, hard potentials squash phase-space fieldlines in position, thus, elliptically expanding them in momentum, see bottom row of Fig. 9.3. This observation can be applied to the shape of zero lines (see Section 7.2) as well: compare the green lines in Fig. 9.2 and in the top row of Fig. 9.3. Soft potentials invert this scenario; expansion in x leads to an elliptical squeeze in p, see middle row of Fig. 9.3. Odd potentials are effectively hard on the left and soft on the right side. This leads to a growth in position spread and reduction in momentum spread, similar to the case of soft potentials, but, additionally, phase-space features tend to be moved to the right, towards the side where the potential is open, see bottom row of Fig. 9.3.

Existence of Distinct Stagnation Points

In the limit of vanishing anharmonicity ($D \to \infty$), the potential expressions in Table 9.1, all reduce to the quantum harmonic oscillator in reference form, $\frac{x^2}{2}$ in Eq. (7.1). This implies that their respective eigenfunctions, eigenenergies and Wigner functions converge pointwise towards those of the quantum harmonic oscillator. The discussion below shows that pointwise convergence does not occur for the associated Wigner current fieldline portraits.

The *degeneracy* of the quantum harmonic oscillator Wigner functions in Eq. (7.3), leads to formation of lines of stagnation, see Section 7.2. The presence of the quantum corrections terms ($l \geq 1$ in Eq. (4.16)), lifts this degeneracy for anharmonic potentials. As can be seen in Figs. 9.3 and 9.2, the quantum correction terms deform the zero lines of the momentum component of the current ($J_p = 0$, thick blue lines) differently compared to the position component ($J_x = 0$, thick green lines). Therefore the zero lines of the components cross each other at discrete points in phase-space forming separate stagnation points at their intersections. The x-axis is also coloured green since J_x in Eq. (4.16) also vanishes at $p = 0$, yielding two stagnation points for all blue ($J_p = 0$) lines intersecting it. Similarly, the p-axis is a blue line of zero of J_p in the harmonic case (see Fig. 7.3), and, for symmetry reasons, also for even potentials. For odd potentials these J_p zeros do not lie on the p-axis but are displaced to the right. In section 9.3 we confirm these statements through a mathematical analysis.

Can an alternative to the break-up of the J_p zero lines in the bottom row of Fig. 9.3 exist for odd potentials? The answer is – it cannot; to the left of the p-axis an odd potential is hard and therefore has to yield the characteristic pattern displayed in the top row; to the right it is soft, yielding the middle row pattern. Near the p-axis both portraits meet but cannot be connected due to the continuity of J_x and J_p as functions of x and p. The only option, respecting continuity, is the cut-and-reconnect pattern we see realised in the bottom row of Fig. 9.3.

The elliptic squashing and expansion of the zero lines of J_x and J_p, leads to deformation of their common zero line in the harmonic case (see Fig. 7.3), into two ellipses of different eccentricities, common centres, and equal area, which are aligned with the coordinate axes of phase-space. In the limit of vanishing anharmonicity, these ellipses intersect at odd multiples of 45 degrees (counted from the positive x-axis), forming the *diagonal stagnation points* we observe in Figs. 9.3 and 9.2.

This qualitative discussion has shown that for weakly-anharmonic even potentials $8n + 1$ stagnation points are to be expected for all low lying eigenstates ψ_n: one at the origin, two on the x-axis and two on the p-axis, and four diagonal stagnation points. For weakly-anharmonic odd potentials there are $6n+1$ stagnation points per eigenfunction, since the p-axis stagnation points are all avoided by the cut-and-reconnect mechanism, mentioned above.

In short, weakly anharmonic potentials are fundamentally non-classical [5, 27]. The Wigner functions for eigenfunctions of a weakly anharmonic potentials converge pointwise towards those of the quantum harmonic oscillator, but the collections of fieldlines do not. In this sense there cannot be a smooth transition from quantum to classical case in either the limit of $\hbar \to 0$ or vanishing non-linearity in the potential. This is at variance with published statement such as — *"Trajectory methods [...] are not reliable in general, being restricted to interaction potentials which do not deviate too much from an harmonic potential."* [41], or: *"the first step toward a systematic and general Wigner description is to consider a system whose potential differs only slightly from a harmonic potential"* [70].

Displacement on the x-axis of $J_x = 0$ vs $J_p = 0$

Numerically, we see that the zero lines of J_x and J_p shift differently. We now confirm this analytically.

Similarly to equation (9.10), we determine the displacement δx_{J_p} of the zero of J_p on the x-axis using the Newton gradient method at $(x, p) = (\tilde{X}, 0)$, here $\tilde{X}$ denotes the point where

the Wigner distribution is zero, i.e., where $J_x = 0$.

$$\delta x_{J_p}\Big|_{(\tilde{X},0)} \approx \frac{\hbar^2\nu(\nu-1)(\nu-2)}{24} \cdot \alpha_\nu x^{\nu-4} \frac{\partial_p^2 W^\odot}{\partial_x W^\odot}\Big|_{(\tilde{X},0)} . \tag{9.7}$$

Now, the Mexican hat profiles of the harmonic oscillator's Wigner distributions (see insets Fig. 7.3) imply that $\partial_p^2 W^\odot_{n,n}/\partial_x W^\odot_{n,n}|_{(\tilde{X},0)} > 0$ for $\tilde{X} > 0$ and is negative for $\tilde{X} < 0$.

For example, if the potential is stiff and symmetric ($\alpha_4 > 0$) we know that the contours of W are squeezed inward on the x-axis, in other words the magnitude of the zeros of the Wigner distributions on the x-axis obey $|\tilde{X}_W| < |\tilde{X}^\odot_W|$. In this case $\delta x_{J_p}\Big|_{(\tilde{X},0)} > 0$, this counteracts the inward movement of the zeros of J_x, the zero line of J_p is less deformed than that of J_x.

The same logic can be applied to stiff and odd, weakly-anharmonic potentials. This discussion in particular confirms that an odd potential's behaviour constitutes a hybrid of stiff and soft potentials' behaviour, see Fig. 9.3.

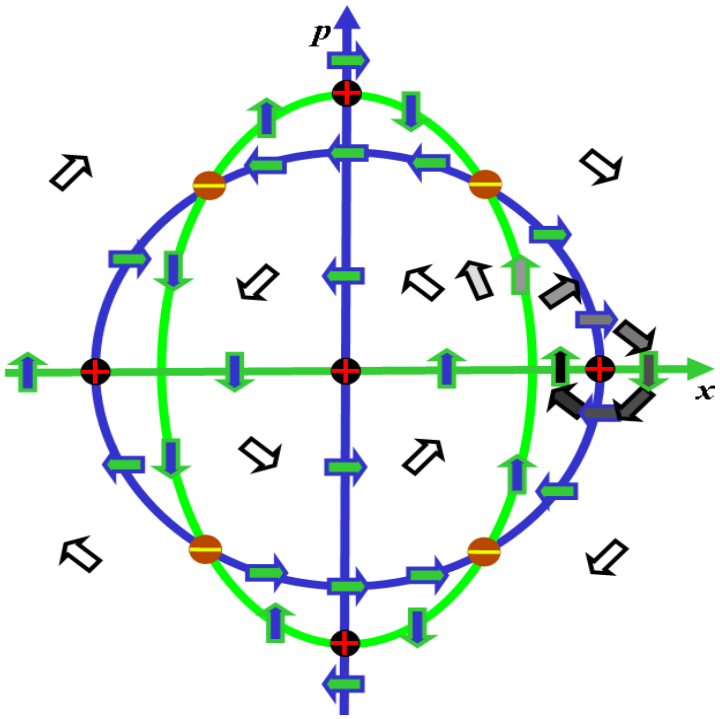

Figure 9.2 Qualitative discussion of the emergence (type and positioning) of the Wigner current stagnation points for the first excited state of a hard potential. White arrows represent normalised Wigner current as observed in the quantum harmonic oscillator; clockwise, far from the origin, and anti-clockwise (inverted current) very close to the origin (compare left panels of Fig. 7.3). Green and blue delineated ellipses represent the zero lines, see Section 7.2, deformed by the anharmonicity of the potential. They are coloured green when J_x changes sign and blue when J_p does; this also applies to x and p-axis. We track the orientation of the current while moving across phase-space along the sequence of arrows with ever darker shades of grey which eventually wraps around the rightmost '+1' stagnation point. Whenever this sequence crosses a zero line ($J_x = 0$ or $J_p = 0$), the arrows are framed green or blue, respectively. We can similarly track the current's orientation around the boundaries of the deformed zero lines and along the x and p-axis. Green arrows with blue fringe are orientated horizontally ($J_p = 0$) and invert direction whenever the blue line they are pinned to crosses a green line. Blue arrows with green fringe are tied to green lines, are vertically aligned, and behave analogously. At every crossing of a green with a blue line, a stagnation point exists, but nowhere else. Using this method we can work out the topological charge of the stagnation points, labelled as the symbols of Fig. 2.2. The quantitative plots in the top row of Fig. 9.3 confirm this qualitative analysis.

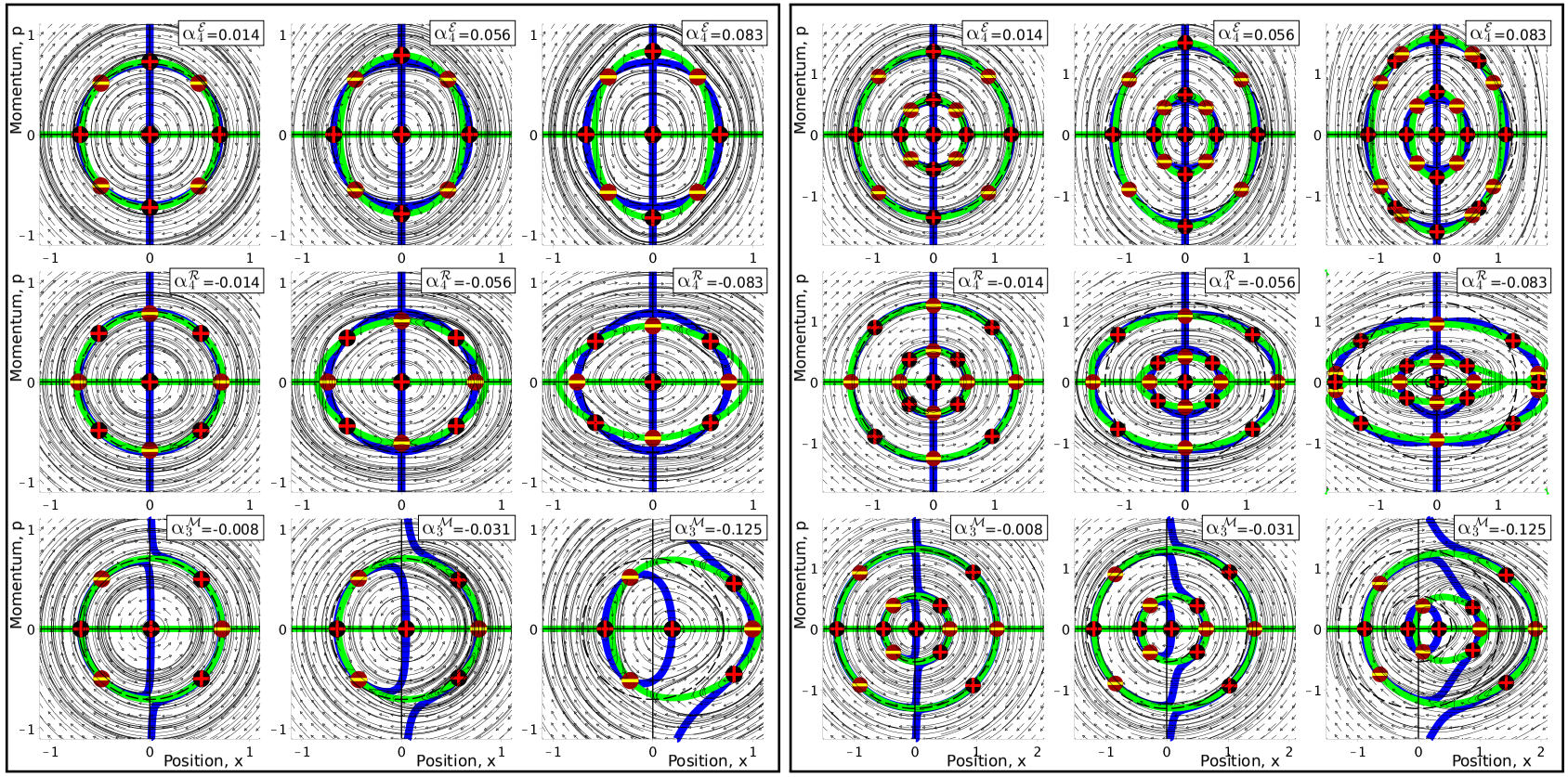

Figure 9.3 Wigner current fieldline portraits of the first and second excited states (left and right frame, respectively), for the three classes of weakly anharmonic potentials: hard Eckart (top row), soft Rosen-Morse (middle row), and odd Morse (bottom row). Note that the Wigner current fieldline portraits of odd potentials feature shapes of the hard (for $x < 0$) and the soft (for $x > 0$). The respective values of the anharmonicity coefficient $\alpha_\nu^{\mathcal{A}}$ in Eq. (9.1) are quoted in each panel, increasing from left to right in each frame (note that identical values of $\alpha_\nu^{\mathcal{A}}$ were used for both the first and second excited states), corresponding to the values of $D = (12, 3, 2)$ (top row), $D = (12, 5, 4)$ (middle row), and $D = (2048, 128, 8)$ (bottom row). Wigner current fieldlines and their colouring have been adopted from Fig. 7.3. Thick blue and green lines refer to the zero lines of $J_p = 0$ and $J_x = 0$, respectively. The stagnation points at their crossings are labelled as in Fig. 2.2.

9.4 Wigner Current Fieldine Portraits for Two-State Superpositions

We now consider superpositions of eigenfunctions. Fieldline plots present a momentary snapshot in time but poorly represent the behaviour over long times.

Vortex Displacement near Potential's Minimum

A full analysis of the displacement of the vortex near the minimum of a potential would entail determination of the Wigner function of the anharmonic system. For our qualitative study we use the quantum harmonic oscillator's Wigner functions $W^{\odot}$ (see Section 7.2), and investigate the shift to lowest order in $\hbar$: $\boldsymbol{J} \simeq \boldsymbol{J}_{[1]}$ in Eq. (4.17), Taylor-expanded in x.

At the position ($X = 0$) of the potential's minimum $\partial_x V = 0$, $\partial_x^2 V = 1$, and $\partial_x W \approx \partial_x W^{\odot} = 0$. Therefore, approximations of $J_{p,[1]}$ and $\partial_x J_{p,[1]}$, up to first order in $\delta x = x - X$ (evaluated at phase-space position $(x = X, p = P)$, and referred to as $\partial_x J_p|_{(X,P)}$, etc.), are

$$\begin{aligned} J_{p,[1]}\Big|_{(X,P)} &\approx -W\partial_x V + \frac{\hbar^2}{24}\partial_p^2 W \partial_x^3 V_\nu\Big|_{(X,P)} \\ &= -xW + \frac{\hbar^2\nu(\nu-1)(\nu-2)}{24}\cdot\alpha_\nu x^{\nu-3}\cdot\partial_p^2 W\Big|_{(X,P)} \qquad (9.8) \\ \text{and } \partial_x J_{p,[1]}\Big|_{(X,P)} &\approx \partial_x\left(-W\partial_x V + \frac{\hbar^2}{24}\partial_p^2 W\partial_x^3 V_\nu\right)\Big|_{(X,P)} \\ &\approx -W - x\partial_x W + \partial_x \frac{\hbar^2\nu!}{24(\nu-3)!}\cdot\alpha_\nu x^{\nu-3}\cdot\partial_p^2 W\Big|_{(X,P)} . \qquad (9.9) \end{aligned}$$

With the Newton gradient approximation for the x-shift of the zero of J_p at the origin $\delta x_{J_p}|_{(0,0)} \approx -J_p|_{(0,0)}/\partial_x J_p|_{(0,0)}$, and with $\alpha_\nu \ll 1$, implying $W \approx W^{\odot}$, the minimum vortex' shift is

$$\delta x_{J_p}\Big|_{(0,0)} \approx \frac{\hbar^2\nu(\nu-1)(\nu-2)}{24}\cdot\alpha_\nu x^{\nu-3}\cdot\frac{\partial_p^2 W^{\odot}}{W^{\odot}}\Big|_{(0,0)} . \qquad (9.10)$$

The stagnation point of $\boldsymbol{J}$ near the minimum of even potentials, $\partial_x^{(2l+1)}V|_{(0)} = 0$, does not shift at all: $\delta x_{J_p}|_{(0,0)} = 0$. This result conforms with our expectation that, for symmetry reasons, the vortex at the origin of eigenstates of even potentials does not shift. This can be confirmed, to all orders in α, using Eq. (4.17). The stagnation point of $\boldsymbol{J}$ near the minimum of the potential only shifts for odd potentials. If the potential is anharmonic in higher than third order, a higher order expansion has to be performed. With a third order anharmonicity, we assume that $\alpha_3 < 0$. The Mexican hat profiles of the harmonic oscillator's Wigner distributions (see insets Fig. 7.3) imply that $\partial_p^2 W^{\odot}_{n,n}/W^{\odot}_{n,n}|_{(0,0)} < 0$. Therefore, according to Eq. (9.10), with $\nu = 3$, $\delta x_{J_p}|_{(0,0)} > 0$. This confirms the shift to the right, in the direction of the potential's opening, and is visible in the bottom row of Fig. 9.3.

For a superposition state's time-dependent displacement of the vortex near the minimum of the potential, $\delta x_{J_p}(t)$, Eq. (9.10) provides a reasonably good approximation. This is depicted in Fig. 9.4.

Note that in the classical case the vortex at the potential's minimum is not displaced at all, see Fig. 9.1. In general, vortex displacement over time is a pure quantum effect.

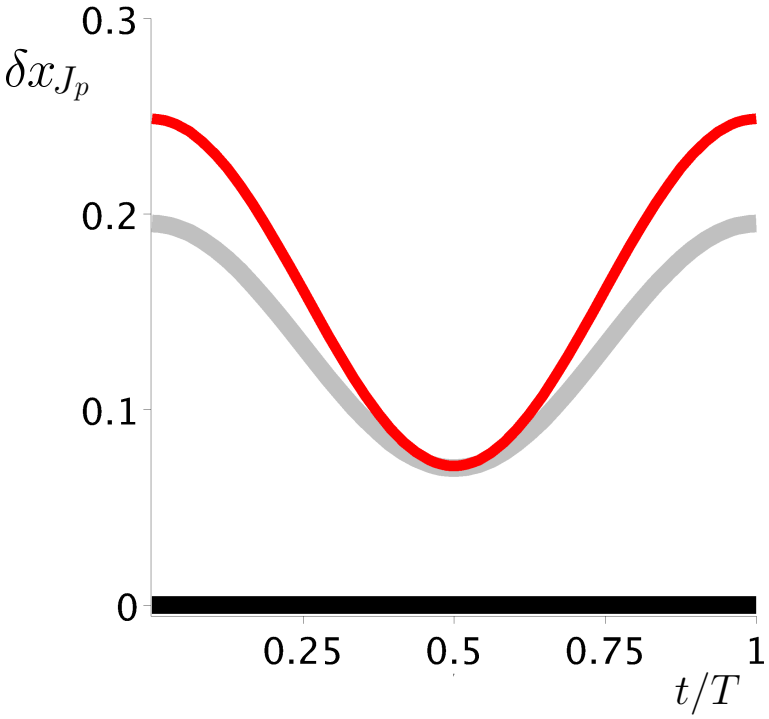

Figure 9.4 Time-dependent quantum displacement δx_{J_p} in Eq. (9.10) of the Morse potential minimum's stagnation point along the x-axis versus time for superposition state $\Psi_{0,2}(x,t;\frac{\pi}{4})$, with anharmonicity value, Table 9.1, $\alpha_3^{\mathcal{M}} = -0.088$ ($D = 16$, $N = 32$). Black curve: position of minimum of potential. Red curve: numerically determined displacement using $\boldsymbol{J}_{[10]}$ of Eq. (4.17). Grey curve: first order approximation Eq. (9.10), namely: $\delta x_{J_p} = \frac{\sqrt{2}\cos\left(2t-\frac{3t}{2D}\right)+3}{4\sqrt{2D}}$.

The Ferris Wheel Effect – alignment with x and p-axes

According to the discussion in Section 9.3, four diagonal stagnation points form per zero-circle of every eigenstate. If we 'perturb' an eigenstate by, say, mixing in a little bit of groundstate ($\Psi_{m,0}(\theta)$ of Eq. (3.8) with $\theta \ll 1$), the zero-circles get displaced from the origin (see Eq. (8.3)). Yet, for small values of θ the four diagonal stagnation points remain pinned to the zero-circle while it rotates around the origin as time progresses. They do this in such a way that they keep their relative orientation with respect to the axes of phase-space as seen from the zero-circle's centre. In other words, while they travel through phase-space they behave somewhat like markers on a Ferris wheel cabin, where the zero-line, $J_x = 0$, depicts the cabin's outline, see Figs. 9.6, 9.7 and 9.8.

The remaining stagnation points are pinned to the intersections of the zero circles with x- or p-axes. When the off-centre displacement becomes larger, the diagonal stagnation points start to interact with stagnation points on the axes leading to repulsion or coalescence. Such interactions are constrained by the topological charge associated with the stagnation points' flow winding number. If the magnitude of the sum of their charges is not greater than one, they can merge, otherwise they are topologically protected and repel each other, this is illustrated in Figs. 9.6, 9.7, 9.8, and 9.9.

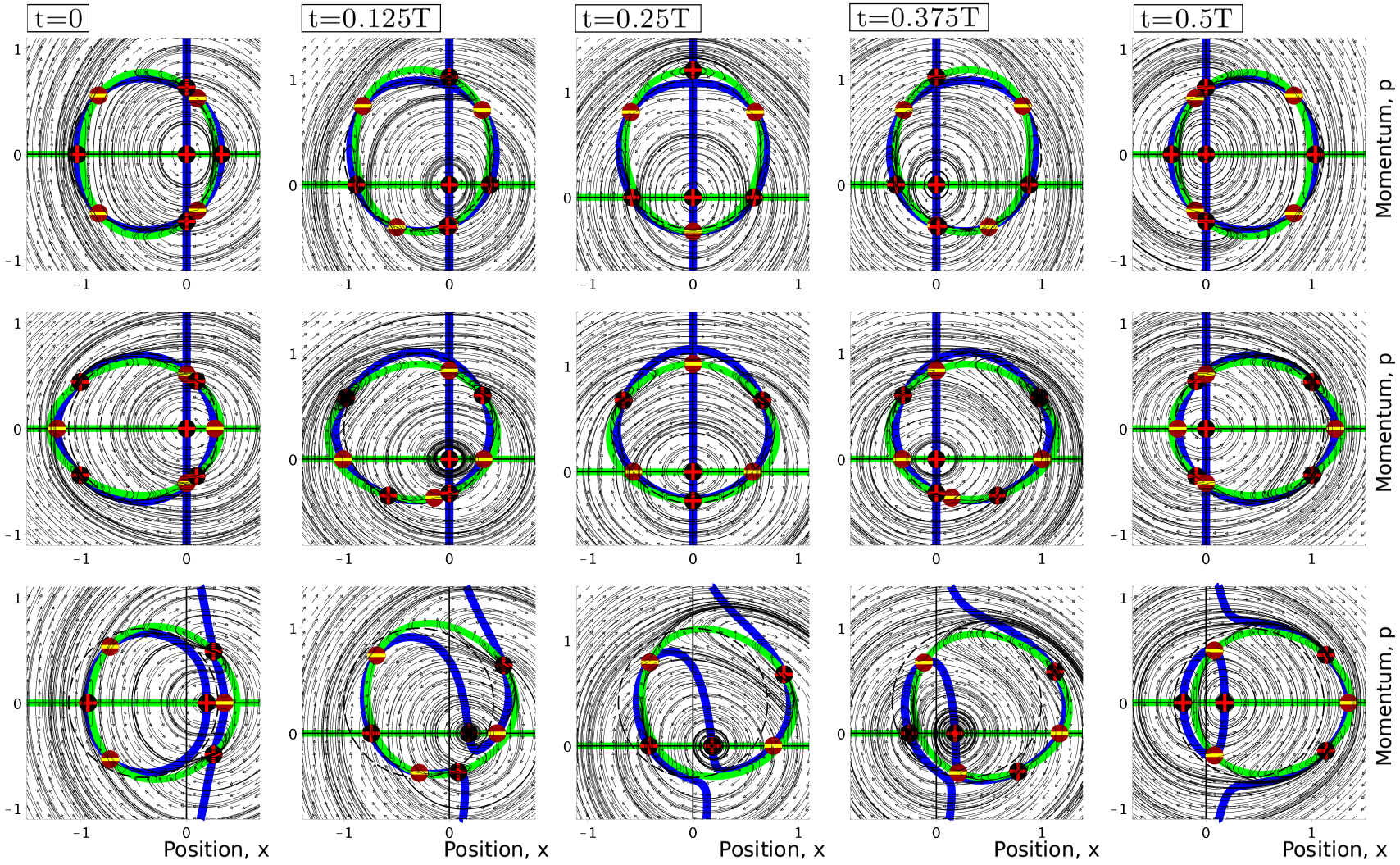

Figure 9.5 Wigner current fieldline portraits $\boldsymbol{J}_{[10]}$ (4.17) for the superposition state $\Psi_{0,1}(t;\frac{\pi}{3})$ for times $t/[T^{\mathcal{A}}_{0,1}] = 0$, 1/8, 1/4, 3/8, 1/2. The same symbols as in Fig. 9.3 are used. The potentials are (see Table 9.1) Eckart potential, with $\alpha^{\mathcal{E}}_4 = 0.042$ ($D = 4$) (top row), Rosen-Morse potential, with $\alpha^{\mathcal{R}}_4 = -0.042$ ($D = 4$, $N = 8$), and Morse potential, with $\alpha^{\mathcal{M}}_3 = -0.088$ ($D = 16$, $N = 32$). Note that the Morse potential is odd, i.e. it is hard on the left ($x < 0$) and soft on the right side ($x > 0$); accordingly, the fieldline portraits on the left resemble those of the Eckart potential depicted (top row) and those on the right resemble those for the Rosen-Morse potential (middle row).

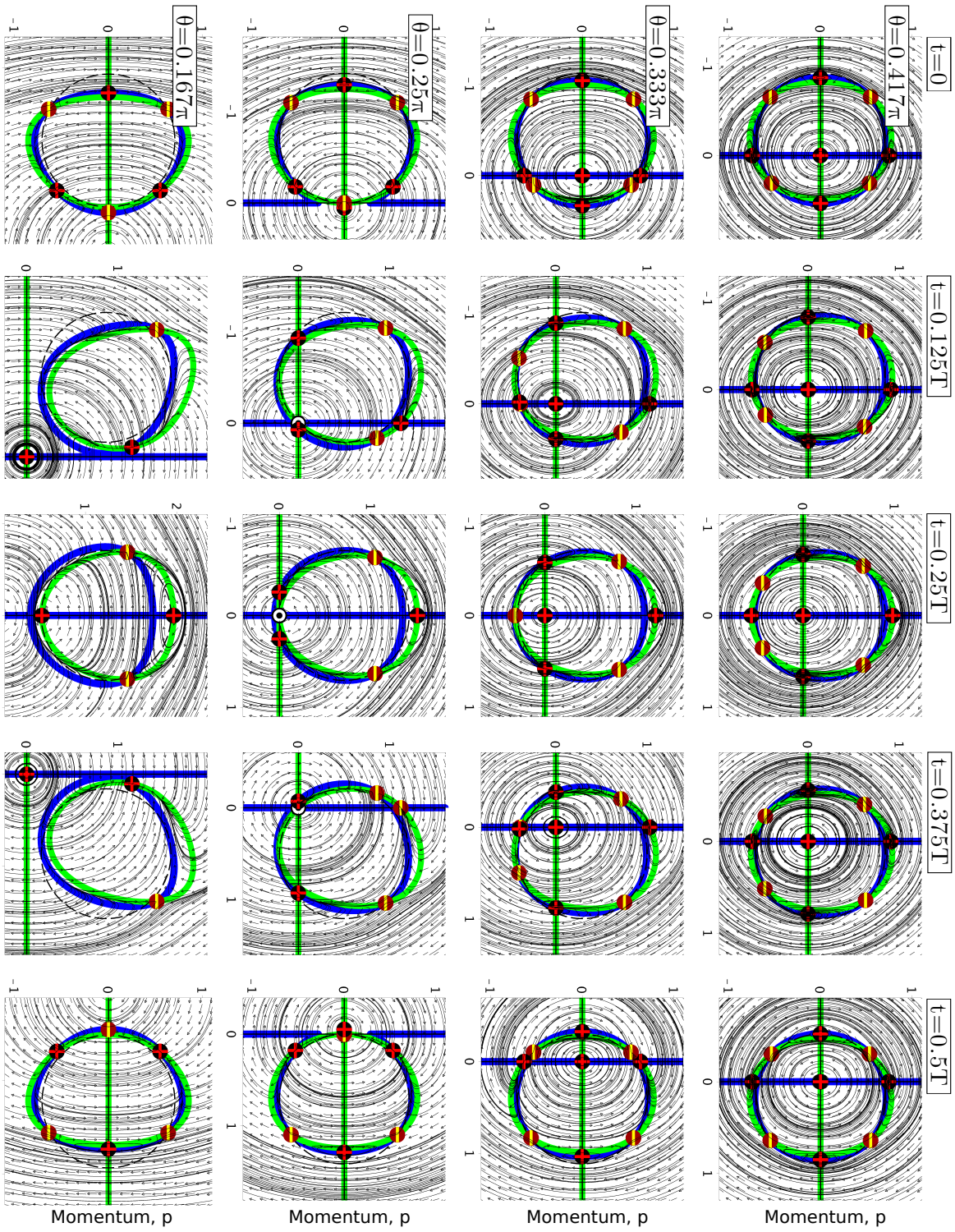

Figure 9.6 Wigner current fieldline portraits $\boldsymbol{J}_{[10]}$ Eq. (4.17) for the superposition state $\Psi_{0,1}(t;\theta)$ of the Eckart potential, Table 9.1, with anharmonicity value $\alpha_4^{\mathcal{E}} = 0.042$ ($D = 4$). The same symbols as in Fig. 9.3 are used. For saddle points ($\omega = 0$) a stylised 'zero' symbol is used, compare Fig. 2.2.
From top to bottom, the weighting angle θ in $\Psi_{0,1}(t;\theta)$ of Eq. (3.8) is decreased from $5\pi/12$ over $\pi/3$, $\pi/4$ to $\pi/6$.
From left to right time $t/[T_{0,1}^{\mathcal{E}}]$ increases from 0 over 1/8, 1/4, 3/8 to 1/2.

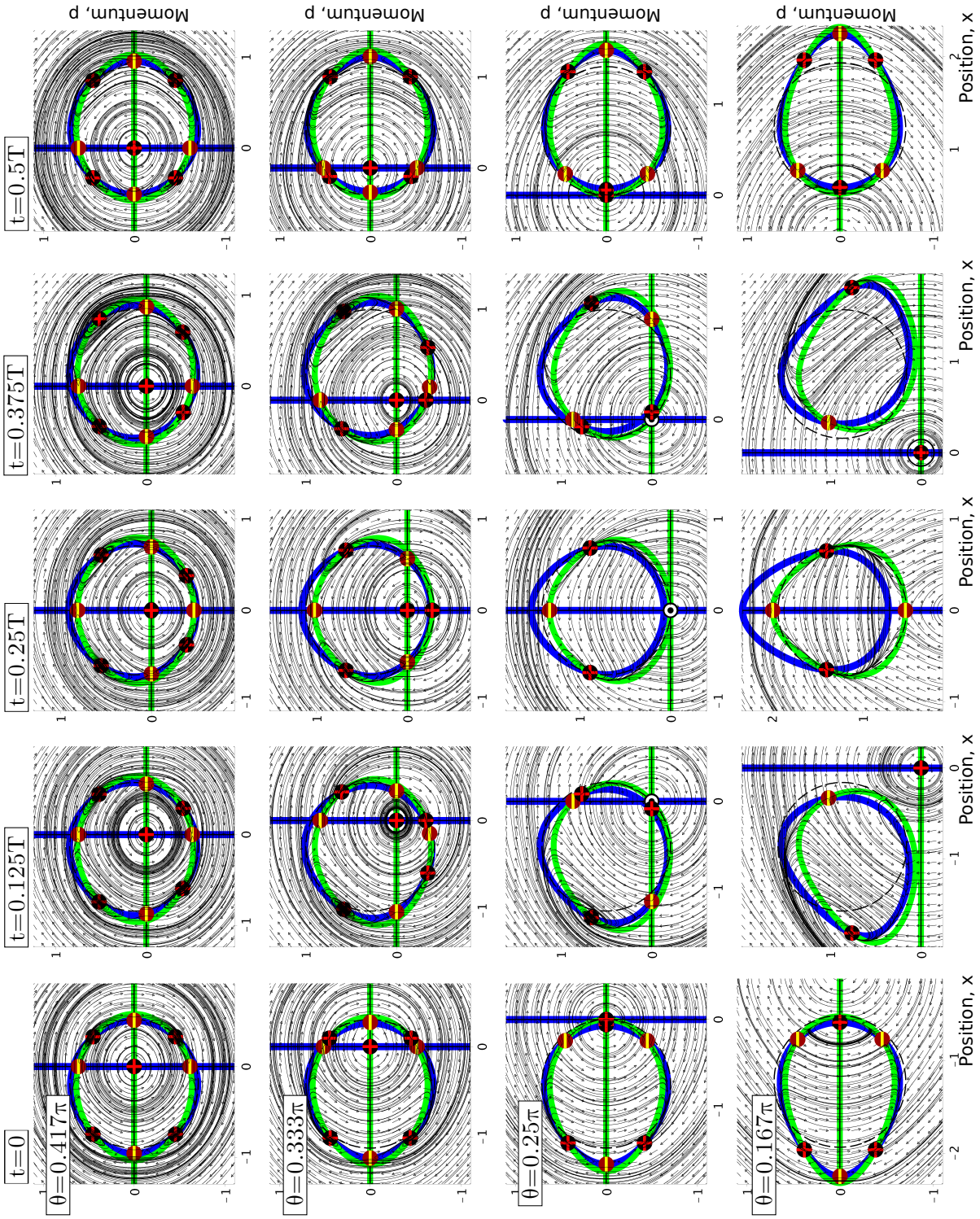

Figure 9.7 Wigner current fieldline portraits $\boldsymbol{J}_{[5]}$ Eq. (4.17), as in Fig. 9.6, for the Rosen-Morse potential, Table 9.1, with anharmonicity value $\alpha_4^{\mathcal{R}} = -0.042$ ($D = 4$, $N = 8$).

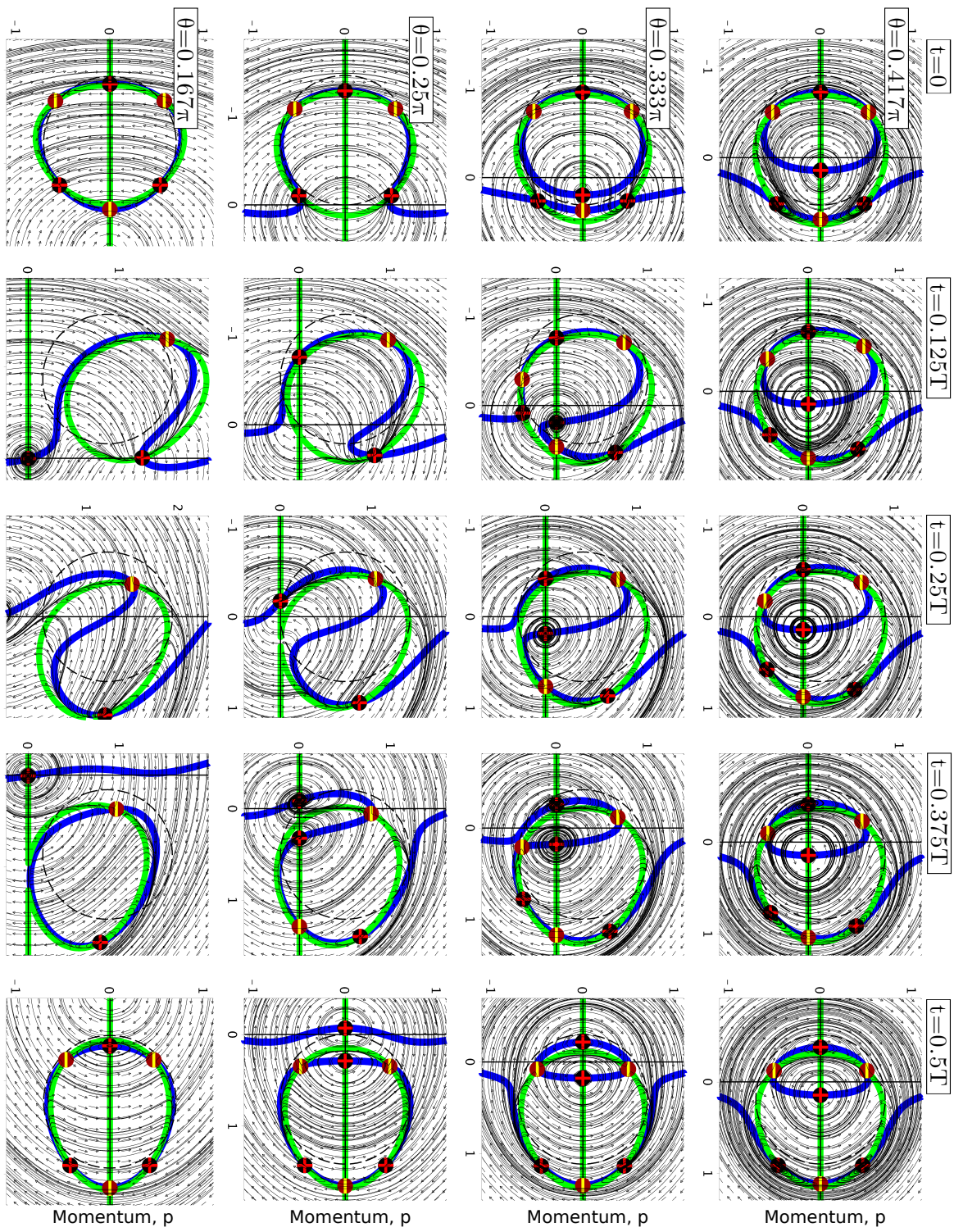

Figure 9.8 Wigner current fieldline portraits, as in Figs. 9.6 and 9.7, for the Morse potential, Table 9.1, with anharmonicity value $\alpha_3^{\mathcal{M}} = -0.088$ ($D = 16$, $N = 32$). Note that the Morse potential is odd, i.e. it is hard on the left ($x < 0$) and soft on the right side ($x > 0$). Accordingly, the current fieldline portraits on the left resemble those of the (hard) Eckart potential depicted in Fig. 9.6 and those on the right resemble those for the (soft) Rosen-Morse potential depicted in Fig. 9.7.

Wigner Current Dynamics of the Rabi Cycle

To investigate a simple system in which the weighting angle θ of the superposition state (3.8) changes considerably while the dynamics progresses, we study a resonantly driven Rabi system (see Section 3.5). Its solution for a superposition of ground and first excited state is

$$\Psi^R_{0,1}(x,t;\theta(t)) = \Psi_{0,1}(x,t;\frac{\Omega_R}{2}t+\frac{\pi}{2}) \,, \tag{9.11}$$

where Ω_R is the Rabi frequency [55, 74] and the rotating wave approximation has been used. In accord with this approximation we assume that the perturbation is so small that we can neglect the time-dependence of the Hamiltonian when determining the fieldlines of $\boldsymbol{J}$.

The Rabi state (9.11) displays Wigner current fieldline portraits associated with the system's (fast) intrinsic dynamics while (slowly) shifting the weighting of the superposition state: for the ratio of these two system frequencies we choose $\frac{\Omega_R}{\Omega^\odot} = 1/8$ in Fig. 9.10.

Fig. 9.10 shows plots with zero-circles of Eq. (8.3) tied to a spiral centred on $t = 0$ (since $\Psi^R_{0,1}(t=0) = \psi_1$) which expands outward as more of the groundstate gets mixed in with increasing values of $|t|$. We notice that the Ferris wheel-effect tends to keep the orientation of the stagnation points on the zero circle aligned with x- and p-axes. With our choice of $\frac{\Omega_R}{\Omega^\odot} = \frac{1}{8}$, around $|t| = 2T$ the mixing angle is roughly $|\theta| = \pi/4$. At this stage the zero-circle gets displaced by its radius and stagnation points on the circle interact with those on x- and p-axes. In the corresponding Sections of Fig. 9.10 repulsion, attraction, coalescence and splitting of stagnation points can be seen– all constrained by conservation of topological charge.

Other Wigner Current Fieldline Portraits

In the Rabi-scenario, depicted in Fig. 9.10, the weighting angle changes dynamically. We can also monitor the changes that arise when we change it 'by hand'. The topological nature of the stagnation points conserves the current winding number in this case as well, see Fig. 9.11.

Other superposition states, such as $\Psi_{1,2}$, can show symmetric flower petal arrangements, see insets in Fig. 9.12, which have recently been observed experimentally [76]. Fig. 9.12 shows how the three different types of weakly-anharmonic potentials give rise to current portraits.

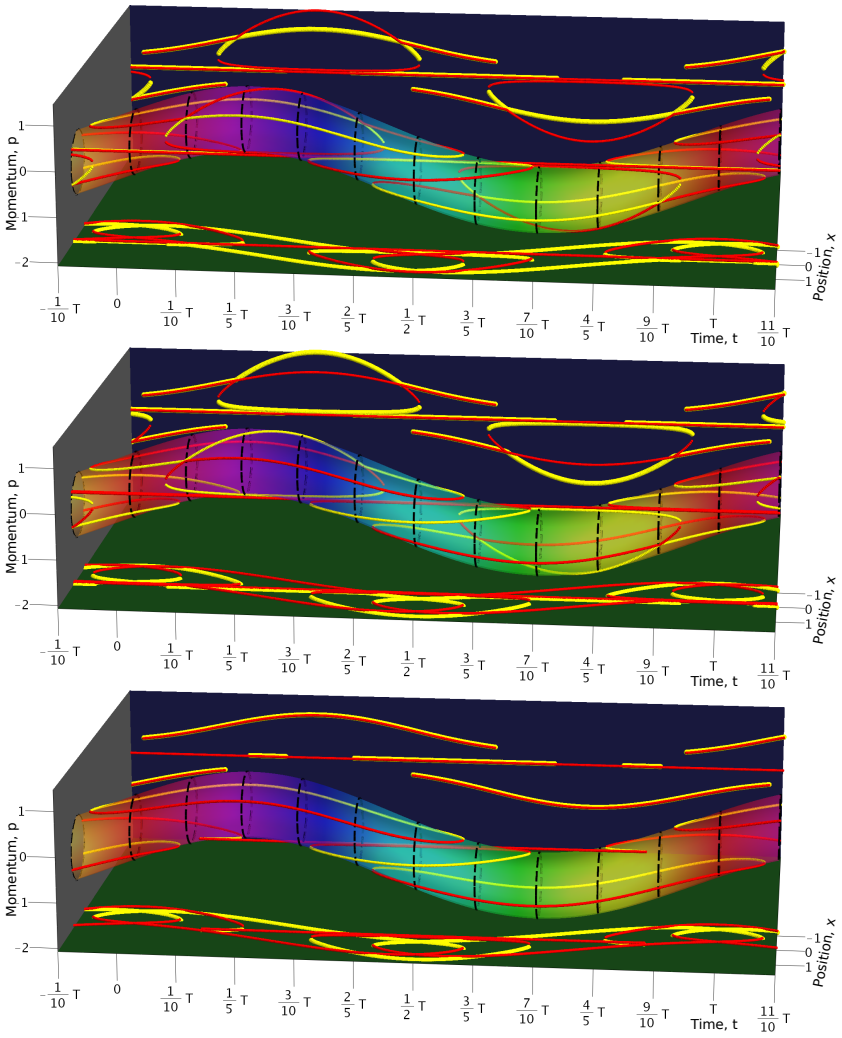

Figure 9.9 Time evolution of the Wigner current stagnation points $\boldsymbol{J}_{[1]}$ Eq. (4.17) for the superposition state $\Psi_{0,1}(0.95\frac{\pi}{4})$ in Eq. (3.8), with probability 0.54 for ground and 0.46 for first excited state. The panels feature, from top to bottom, a (hard) Eckart, (soft) Rosen-Morse and (odd) Morse potential, Table 9.1, with respective anharmonicity values, $\alpha_4^{\mathcal{E}} = 0.002$ ($D = 100$), $\alpha_4^{\mathcal{R}} = -0.002$ ($D = 100$, $N = 200$) and $\alpha_3^{\mathcal{M}} = -0.004$ ($D = 10000$, $N = 20000$). The helical tube depicting the position of the zero circle of Eq. (8.3), nearly touches the origin. To guide the eye, every tenth of the full period is denoted by a dashed black zero circle painted onto the tube which is rainbow-coloured to display the flow of time, one period Eq. (3.6) per rainbow. The position of stagnation points is depicted by red lines if they carry charge $\omega = +1$ and yellow if $\omega = -1$, see Fig. 2.2. The stagnation point positions are additionally projected along the x-axis onto the blue wall in the back and along the p-axis downward onto the green floor.
Winding number conservation implies that positively and negatively charged stagnation points originate and annihilate together, this is seen as red and yellow lines forming loops which are reminiscent of the formation of the torus reported in Fig. 4 of reference [4]. As mentioned in the caption of Fig. 9.3 plots for the odd Morse potential (bottom panel), contain features of the soft Rosen-Morse potential (middle panel) for $x > 0$ and of the hard Eckart potential (top panel) for $x < 0$.

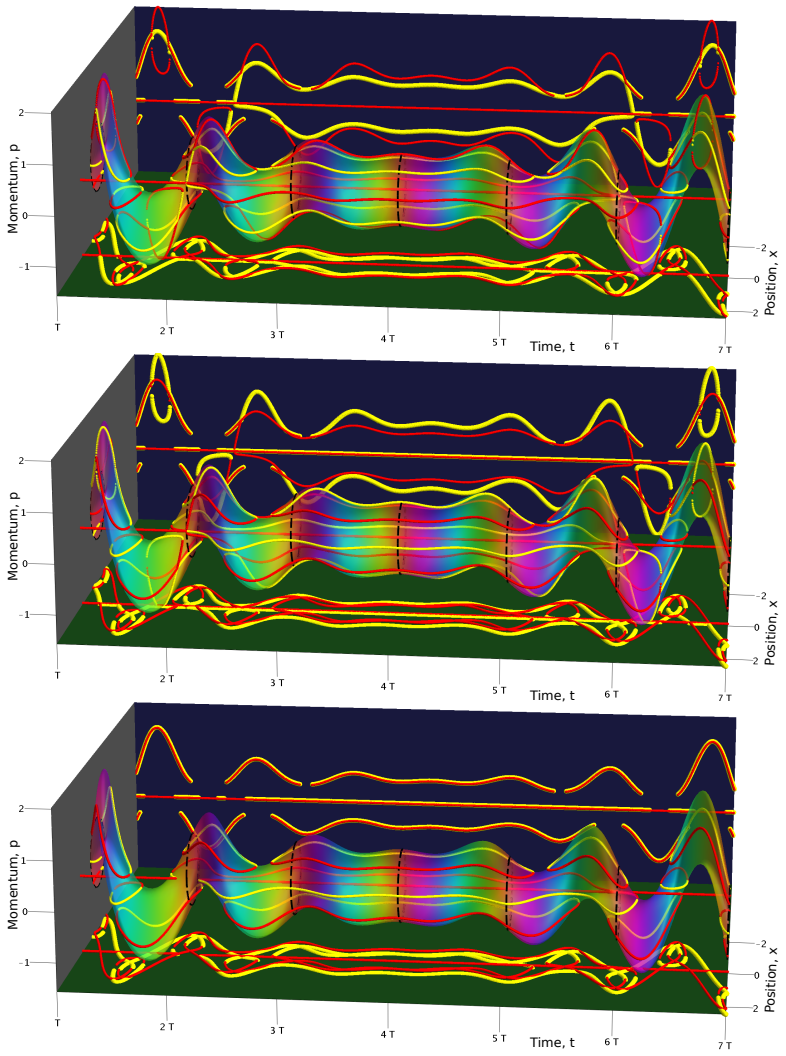

Figure 9.10 Rabi cycle for state (9.11) with frequency ratio $\Omega_R/\Omega^{\odot} = 1/8$. The panels feature, from top to bottom, a soft, hard and odd potential, Table 9.1, with respective anharmonicity values, $\alpha_4^{\mathcal{E}} = 0.002$, $\alpha_4^{\mathcal{R}} = -0.002$ and $\alpha_3^{\mathcal{M}} = -0.004$. At time $t = 0$ the system is in the first excited state; at other times the zero-circle's center (8.3) is displaced from the origin such that, over time, it sweeps out a helix with varying width. This is displayed as a helical tube whose rainbow coloring depicts the flow of time. Every full period ($T^{\odot} = 1$) is denoted by a dashed black zero-circle. Stagnation points are depicted by red lines when carrying charge $\omega = +1$ and yellow if $\omega = -1$, see Fig. 2.2. The stagnation point positions are additionally projected along the x-axis onto the blue wall in the back and along the p-axis downward onto the green floor. Winding number conservation implies that positively and negatively charged stagnation points originate and annihilate together, this is seen as red and yellow lines forming loops which are reminiscent of the formation of the torus reported in Fig. 4 of reference [4]. As mentioned in Figs. 9.3 above, the bottom panel, for the odd Morse potential, inherits features of Rosen-Morse potential and Eckart Potential.

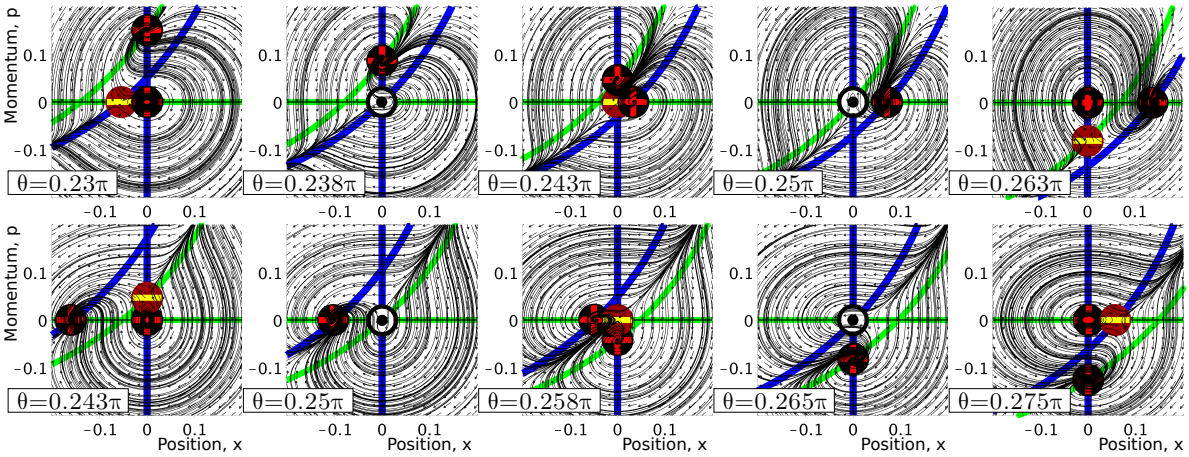

Figure 9.11 Conservation of the Wigner current winding number for fixed time $t = T/8$ but varying weighting angle θ of the superposition state $\Psi_{0,1}(x, \frac{T}{8}; \theta)$. We observe movements of stagnation points leading to their merger and splitting. The top row refers to the hard Eckart and bottom row to the soft Rosen-Morse potential with identical parameters as in Figs. 9.6 and 9.7, respectively. Note the non-Liouvillian nature of the flow featuring regions of pronounced flow expansion and compression.

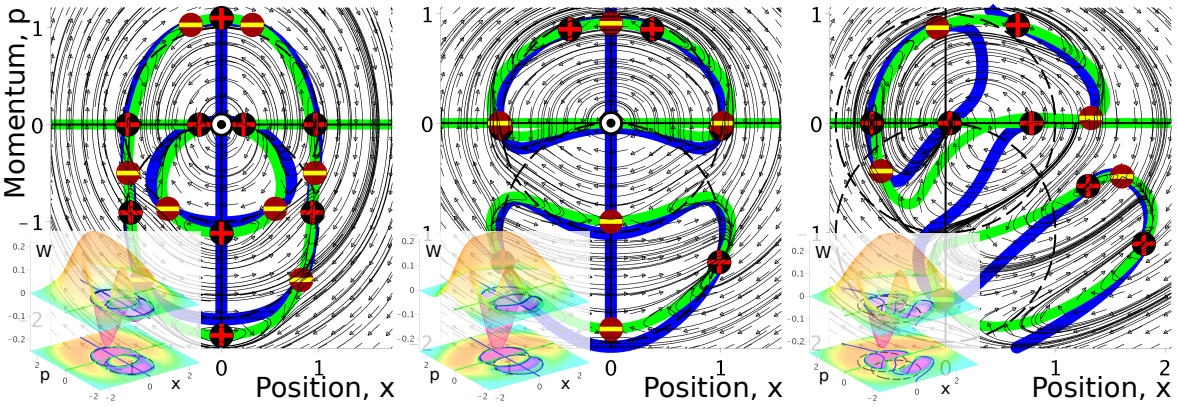

Figure 9.12 Wigner current fieldline portraits for state $\Psi_{1,2}\left(x, \frac{3T}{4}; \frac{\pi}{4}\right)$ in Eq. (3.8) for, from left to right, Eckart, Rosen-Morse and Morse potentials Table 9.1, with respective anharmonicity values $\alpha_4^{\mathcal{E}} = 0.042$ ($D = 4$), $\alpha_4^{\mathcal{R}} = 0.033$ ($D = 5$, $N = 10$), and $\alpha_3^{\mathcal{M}} = 0.125$ ($D = 8$, $N = 16$). The same symbols as in Fig. 9.3 are used. Zeros of the Wigner function (thick green lines) intersect with zeros of the momentum component of Wigner current (thick blue line) yielding fairly intricate arrangements of stagnation points of Wigner current. Similarly to Figs. 9.3, 9.9 and 3.1, the Morse potential's case inherits features of a soft Rosen-Morse potential for $x > 0$ and of a hard Eckart potential for $x < 0$.

10 Conclusions and Future Work

In this Chapter we provide an overview of what has been achieved in this research project as a list of contributions to knowledge and also provide some brief discussions on how to extend the research on quantum dynamics in phase-space.

10.1 Contributions to knowledge

The following list provides an overall contribution to knowledge presented in this thesis. Note that these were not the aims of this research project but rather the final result of our attempt to investigate quantum dynamics in phase-space with the use of the Wigner current:

- In this thesis we have introduced the study of quantum dynamics with the use of the Wigner current and its collections of fieldlines. Collections of Wigner current fieldlines provide the following new insights into the nature of quantum dynamics phase-space:
  - They are quantum analogs of classical phase-space trajectories
  - They represent quantum dynamics of a specific quantum state in phase-space
  - They provide visualisation at-a-glance and thus characterise quantum phase-space dynamics
  - They reveal subtle patterns in phase-space, such as contracting and expanding regions of phase-space, and stagnation points (vortices, separatrices and saddles); similar to classical phase portraits [45, 46]. Therefore, they can be characterised by their stagnation points' distribution and Poincaré-Hopf-indeces.
- In Chapter 3, we introduced the well-known Schrödinger's representation of quantum mechanics which is widely taught during the first year of an undergraduate Physics degree. Here we discussed the position and momentum Schrödinger's representations in parallel using Fourier transforms and it was shown how these representations can be used to naturally introduce Wigner's phase-space representation of quantum mechanics (see Chapter 4). This included the introduction to the Wigner function and Wigner current, naturally arising, with the use of Fourier transforms, from the probability distributions and currents of position and momentum Schrödinger's representations.
- In Chapter 4 we introduced the Wigner function, its continuity equation, and the Wigner current and discussed some of their mathematical properties. These included the projections of the Wigner current components and the derivation of Ehrenfest's theorem as an average over phase-space of the Wigner current components.
- In Chapter 5 it was shown that the use of the infinite-sum form of the Wigner current's momentum component, can lead to incorrect numerical results due to bad convergence. As an alternative, the integral form of the Wigner current's momentum component should be used.
- In Chapter 6, a fundamental proof was presented which shows that the Wigner current of quantum-mechanical systems obeys Liouville's theorem only when the dynamics of the system are governed by Hamilton's equations of motion, i.e., when the quantum

corrections terms of the quantum Liouville equation, vanish. This was used to dismiss concepts such as *Wigner trajectories* and *quantal force* in phase-space.

- In Chapters 7 and 8, the Wigner current's degenerate and semi-degenerate cases featured in the quantum harmonic oscillator and Kerr oscillator, respectively, was discussed. Their difference, lies in the fact that for a degenerate case the zeros of the Wigner function and the zeros of the Wigner current's components coincide in phase-space (apart from the x- and p-axis), but for the semi-degenerate case only the zeros of the Wigner current components coincide.

- In Chapter 9 we show that there are three types of weakly-anharmonic weakly-excited one-dimensional quantum-mechanical systems, which feature, soft, hard and odd potentials. The overall distortions of phase-space in the case of soft potentials (expansion in the x-direction together with compression in the p-direction) and the reversed distortion in the case of hard potentials (compressed in x, expanded in p), allows us to qualitatively consider the emergence of stagnation points of Wigner current and the associated fieldline portraits for eigenfunctions of such potentials. Odd potentials turn out to conform with the established fieldline portraits for soft and hard potentials, in that they are a hybrid of these and behave as such. We also investigated superpositions and find that the position of stagnation points, like in the case of eigenfunctions, tend to align with x- and p-axis in phase-space. This Ferris wheel-effect tends to apply to various superpositions, where we again see that fieldline portraits for odd potentials are hybrids of those of hard and soft potentials.

10.2 Future Work

It would be interesting to investigate the following ideas:

- The only known closed-form expressions of the Wigner function are the ones of harmonic systems and the Morse oscillator [65]. We believe it is possible to also derive closed-form expressions of at least a family of Wigner functions for the Eckart and Rosen-Morse potentials.

- Construct the continuity equation and Wigner current for the case of dissipation (or decoherence, for example when the system is coupled to the environment), and for the Rabi Cycle case, which was briefly mentioned in this thesis.

- In this thesis it was proven that for quantum mechanical systems, in order for the Wigner current to obey Liouville's theorem on volume preservation, the Wigner current must be governed by Hamilton's equations of motion. This occurs when the zeros of the Wigner function and Wigner current's components coincide in phase-space. But is also the reverse true? i.e., when do the zeros of the Wigner function and Wigner current's components coincide? Is it only for the quantum harmonic oscillator?

- In Chapter 7, it was shown the roots of the Laguerre polynomials follow a certain trend, similar to the Hermite polynomials. It might be possible therefore to obtain the exact roots of these polynomials.

- At the end of Chapter 6, we introduced the idea of the Wigner force, inspired by the De Broglie-Bohm theory. Could this result be used to construct quantum trajectories in phase-space?

It would be interesting to see whether investigations of Wigner current might lead to new insights on the nature of 'chaologic' systems [77] and quantum-classical correspondences [78–81]. Here we did *not attempt* to treat either. We would like to emphasise that collections of Wigner current's fieldlines are *an* analog of classical phase-space trajectories. We are aware of the fact that it depends on the details of how the correspondence is made and that other approaches [80] yield other analogies.

A Functions

The functions below were used in the derivation of some of the formulae in the main text. For information see Refs. [82, 83].

1. The Dirac δ function

$$\delta(x-x_0) = \frac{1}{2\pi\hbar}\int_{-\infty}^{\infty} dp\, e^{\frac{i}{\hbar}p(x-x_0)} = \frac{1}{\pi\hbar}\int_{-\infty}^{\infty} dp\, e^{\frac{2i}{\hbar}p(x-x_0)}$$

   Some of its properties used in this thesis:

$$\delta(x-x_0) = \delta(x_0-x) \tag{A.1}$$

$$\frac{d\delta(x-x_0)}{dx} = \frac{2i}{\pi\hbar^2}\int_{-\infty}^{\infty} dp\, p e^{\frac{2i}{\hbar}p(x-x_0)} \tag{A.2}$$

$$\int_{-\infty}^{\infty} dx\, f(x)\frac{d\delta(x)}{dx} = -\int_{-\infty}^{\infty} \delta(x)\frac{df(x)}{dx}\, dx \tag{A.3}$$

$$\int_{-\infty}^{\infty} dx\, f(x)\delta(x-x_0) = f(x_0) \tag{A.4}$$

2. A Hermitian function $f(x)$, satisfies the identity, $f(x) = f^*(-x)$. Thus, $\mathrm{Re}\,(f(x))$ is even in x and $\mathrm{Im}\,(f(x))$ is odd in x.

3. The Kronecker delta $\delta_{mn} = 1$ when $m = n$ and $\delta_{mn} = 0$ when $m \neq n$.

4. Performing a change of variables, $(y_1 \dots y_n) \to (x_1 \dots x_n)$, in a multiple-integral,

$$\int\cdots\int dy_1 \dots dy_n\, f(y_1 \dots y_n) = \int\cdots\int dx_1 \dots dx_n\, f(x_1 \dots x_n)\left|\frac{\partial(y_1 \dots y_n)}{\partial(x_1 \dots x_n)}\right| , \tag{A.5}$$

   makes use of the Jacobian $\mathcal{J}$, defined as

$$\mathcal{J} = \frac{\partial(y_1 \dots y_n)}{\partial(x_1 \dots x_n)} = \det\begin{bmatrix} \frac{\partial y_1}{\partial x_1} & \cdots & \frac{\partial y_1}{\partial x_n} \\ \vdots & \ddots & \vdots \\ \frac{\partial y_n}{\partial x_1} & \cdots & \frac{\partial y_n}{\partial x_n} \end{bmatrix} \tag{A.6}$$

5. The convolution of two functions, f_1 and f_2, is denoted by

$$(f_1 * f_2)(x) = \int_{-\infty}^{\infty} du\, f_1(u) f_2(x-u) = \int_{-\infty}^{\infty} du\, f_1(x-u) f_2(u) = (f_2 * f_1)(x) \tag{A.7}$$

In terms of	$\boldsymbol{J}(x,p)$	$W(x,p)$	$\boldsymbol{\nabla} W$	$\boldsymbol{\nabla} \times \boldsymbol{J}$
Grad: $\boldsymbol{\nabla}$	–	$\boldsymbol{\nabla} W = \begin{pmatrix} \partial_x W \\ \partial_p W \end{pmatrix}$	–	–
Div: $\boldsymbol{\nabla}\bullet$	$\boldsymbol{\nabla} \bullet \boldsymbol{J} = \boldsymbol{\nabla} \bullet (\boldsymbol{w} W)$ $= W \boldsymbol{\nabla} \bullet \boldsymbol{w} + \boldsymbol{w} \bullet \boldsymbol{\nabla} W$ $= \partial_x J_x + \partial_p J_p = -\partial_t W$	–	$\boldsymbol{\nabla} \bullet (\boldsymbol{\nabla} W) = \boldsymbol{\nabla}^2 W$ $= \partial_x^2 W + \partial_p^2 W$	$\boldsymbol{\nabla} \bullet (\boldsymbol{\nabla} \times \boldsymbol{J}) = 0$
Curl: $\boldsymbol{\nabla}\times$	$\boldsymbol{\nabla} \times \boldsymbol{J} = \boldsymbol{\nabla} \times (\boldsymbol{w} W)$ $= W \boldsymbol{\nabla} \times \boldsymbol{w} - \boldsymbol{w} \times \boldsymbol{\nabla} W$ $= W \boldsymbol{\nabla} \times \boldsymbol{w} + \boldsymbol{\nabla} W \times \boldsymbol{w}$ $= \begin{pmatrix} 0 \\ 0 \\ \partial_x J_p - \partial_p J_x \end{pmatrix}$	–	$\boldsymbol{\nabla} \times (\boldsymbol{\nabla} W) = 0$	$\boldsymbol{\nabla} \times (\boldsymbol{\nabla} \times \boldsymbol{J})$ $= \boldsymbol{\nabla}(\boldsymbol{\nabla} \bullet \boldsymbol{J}) - \boldsymbol{\nabla}^2 \boldsymbol{J}$ $= \begin{pmatrix} \partial_p \partial_x J_p - \partial_p^2 J_x \\ \partial_x \partial_p J_x - \partial_x^2 J_p \\ 0 \end{pmatrix}$

Table A.1 Vector calculus identities in 2D phase space, where $W(x,p)$ is a scalar field, and $\boldsymbol{J}(x,p)$ and $\boldsymbol{w}(x,p)$ are vector fields, referred to in this thesis as the Wigner function, and Wigner current and its associated velocity field (see Chapter 4), respectively.

B Published Work

Wigner Flow Reveals Topological Order in Quantum Phase Space Dynamics [4]
Abstract: The behavior of classical mechanical systems is characterized by their phase portraits, the collections of their trajectories. Heisenberg's uncertainty principle precludes the existence of sharply defined trajectories, which is why traditionally only the time evolution of wave functions is studied in quantum dynamics. These studies are quite insensitive to the underlying structure of quantum phase space dynamics. We identify the flow that is the quantum analog of classical particle flow along phase portrait lines. It reveals hidden features of quantum dynamics and extra complexity. Being constrained by conserved flow winding numbers, it also reveals fundamental topological order in quantum dynamics that has so far gone unnoticed.

Wigner's representation of quantum mechanics in integral form and its applications [5]
Abstract: We consider quantum phase space dynamics using the Wigner representation of quantum mechanics. We stress the usefulness of the integral form for the description of Wigner's phase space current $\boldsymbol{J}$ as an alternative to the popular Moyal bracket. The integral form brings out the symmetries between momentum and position representations of quantum mechanics, is numerically stable, and allows us to perform some calculations using elementary integrals instead of Groenewold star-products. Our central result is an explicit, elementary proof which shows that only systems up to quadratic in their potential fulfil Liouville's theorem of volume preservation in quantum mechanics. Contrary to a recent suggestion, our proof shows that the non-Liouvillian character of quantum phase space dynamics cannot be transformed away.

Wigner's quantum phase space current in weakly-anharmonic weakly-excited two-state systems [16]
Abstract: There are no phase space trajectories for anharmonic quantum systems, but Wigner's phase space representation of quantum mechanics features Wigner's phase current $\boldsymbol{J}$. It reveals fine details of quantum dynamics – finer than is ordinarily thought possible according to quantum folklore invoking Heisenberg's uncertainty principle. Here, we focus on the simplest, most intuitive, and analytically accessible aspects of $\boldsymbol{J}$. We investigate features of $\boldsymbol{J}$ for bound states of time-reversible, weakly-anharmonic one-dimensional quantum-mechanical systems which are weakly-excited. We establish that weakly-anharmonic potentials can be grouped into three distinct classes: hard, soft, and odd potentials. We stress connections between each other and the harmonic case. We show that their Wigner current fieldline patterns can be characterised by $\boldsymbol{J}$'s discrete stagnation points, how these arise and how a quantum system's dynamics is constrained by the stagnation points' topological charge conservation. We additionally demonstrate the conceptual power of $\boldsymbol{J}$ by addressing some confusion found in the literature.

Anharmonic quantum mechanical systems do not feature phase space trajectories [27]

Abstract: Phase space dynamics in classical mechanics is described by transport along trajectories. Anharmonic quantum mechanical systems do not allow for a trajectory-based description of their phase space dynamics. This invalidates some approaches to quantum phase space studies. We first demonstrate the absence of trajectories in general terms. We then give an explicit proof for all quantum phase space distributions with negative values: we show that the generation of coherences in anharmonic quantum mechanical systems is responsible for the occurrence of singularities in their phase space velocity fields, and vice versa. This explains numerical problems repeatedly reported in the literature, and provides deeper insight into the nature of quantum phase space dynamics.

Bibliography

[1] E. Wigner, Phys. Rev. **40**, 749 (1932).

[2] R. T. Skodje, H. W. Rohrs, and J. Vanbuskirk, Phys. Rev. A **40**, 2894 (1989).

[3] H. Bauke and N. R. Itzhak, ArXiv e-prints (2011), arXiv:1101.2683 [quant-ph] .

[4] O. Steuernagel, D. Kakofengitis, and G. Ritter, Phys. Rev. Lett. **110**, 030401 (2013).

[5] D. Kakofengitis, M. Oliva, and O. Steuernagel, Phys. Rev. A **95**, 022127 (2017).

[6] W. H. Zurek, Nature **412**, 712 (2001).

[7] A. Moyal, *Maverick Mathematician: The Life and Science of J.E. Moyal* (ANU Press, 2006).

[8] T. L. Curtright and e. a. , *A Concise Treatise on Quantum Mechanics in Phase Space* (World Scientific Publishing Co, 2013).

[9] C. Zachos, Int. J. Mod. Phys. A **17**, 297 (2002).

[10] A. C. Hirshfeld and P. Henselder, Am. J. Phys. **70**, 537 (2002).

[11] W. P. Schleich, *Quantum Optics in Phase Space* (WILEY-VCH Verlag GmbH, 2001).

[12] J. E. Moyal and M. S. Bartlett, Math. Proc. Camb. Philos. Soc. **45**, 99 (1949).

[13] G. A. Baker, Phys. Rev. **109**, 2198 (1958).

[14] O. Steuernagel, Eur. Phys. J. Plus **129**, 114 (2014).

[15] T. Takabayasi, Progr. Theor. Phys. **11**, 341 (1954).

[16] D. Kakofengitis and O. Steuernagel, Eur. Phys. J. Plus **132**, 381 (2017).

[17] L. De Broglie, J. Phys. Radium **8**, 225 (1927).

[18] R. E. Wyatt, *Quantum Dynamics with Trajectories: Introduction to Quantum Hydrodynamics*, Interdisciplinary Applied Mathematics, Vol. 28 (Springer New York, 2005).

[19] E. Madelung, Zeit. f. Phys. **40**, 322 (1927).

[20] D. Bohm, Phys. Rev. **85**, 166 (1952).

[21] D. Bohm, Phys. Rev. **85**, 180 (1952).

[22] B. G. Englert, M. O. Scully, *et al.*, Z. Naturforsch. A **47**, 1175 (1992).

[23] M. V. Berry, Eur. J. Phys. **34**, 1337 (2013).

[24] S. Kocsis, B. Braverman, *et al.*, Science **332**, 1170 (2011).

[25] W. Heisenberg, Zeitschrift fur Physik **43**, 172 (1927).

[26] F. McLafferty, J. Chem. Phys. **83**, 5043 (1985).

[27] M. Oliva, D. Kakofengitis, and O. Steuernagel, Phys. A (2017), 10.1016/j.physa.2017.10.047.

[28] E. J. Heller, J. Chem. Phys. **65**, 1289 (1976).

[29] E. J. Heller, J. Chem. Phys. **94**, 2723 (1991).

[30] A. Donoso and C. C. Martens, Phys. Rev. Lett. **87**, 223202 (2001).

[31] C. J. Trahan and R. E. Wyatt, J. Chem. Phys. **119**, 7017 (2003).

[32] T. Dittrich, E. A. Gómez, and L. A. Pachón, J. Chem. Phys. **132**, 214102 (2010).

[33] W. H. Miller, J. Chem. Phys. **136**, 210901 (2012).

[34] V. S. Filinov, G. Schubert, P. Levashov, M. Bonitz, H. Fehske, V. E. Fortov, and A. V. Filinov, Phys. Lett. A **372**, 5064 (2008).

[35] H. Fehske, J. Schleede, G. Schubert, G. Wellein, V. S. Filinov, and A. R. Bishop, Phys. Lett. A **373**, 2182 (2009).

[36] L. Huaqing, J. Poulsen, and G. Nyman, J. Phys. Chem. Lett. **4**, 3013 (2013).

[37] H. López, C. C. Martens, and A. Donoso, J. Chem. Phys. **125**, 154111 (2006).

[38] D. Kakofengitis and O. Steuernagel, ArXiv e-prints (2011), arXiv:1108.2214 [quant-ph] .

[39] R. Dutt, A. Khare, and U. P. Sukhatme, AJP **56**, 163 (1988).

[40] H. J. Groenewold, Physica **12**, 405 (1946).

[41] J. Daligault, Phys. Rev. A **68**, 010501 (2003).

[42] M. V. Berry, AIP Conf. Proc. **46**, 16 (1978).

[43] L. É. Gendenshteïn, J. Exp. Theor. Phys. Lett. **38**, 356 (1983).

[44] F. Cooper, A. Khare, and U. Sukhatme, *Supersymmetry in quantum mechanics* (World Scientific, 2001).

[45] D. D. Nolte, Physics Today **63**, 33 (2010).

[46] P. Cvitanović, R. Artuso, R. Mainieri, G. Tanner, and G. Vattay, *Chaos: Classical and Quantum* (Niels Bohr Institute, Copenhagen, 2012).

[47] R. Aris, *Vectors, Tensors and the Basic Equations of Fluid Mechanics* (Dover Publications, 2012).

[48] H. Goldstein, C. P. Poole, and J. L. Safko, *Classical Mechanics* (Addison Wesley, 2002).

[49] M. R. Dennis, K. O'Holleran, and M. J. Padgett, in *Progress in Optics*, Vol. 53, edited by E. Wolf (Elsevier, 2009) pp. 293–363.

[50] A. I. M. Rae, *Quantum mechanics* (Taylor & Francis Group, 2008).

[51] M. Belloni, M. A. Doncheski, and R. W. Robinett, Am. J. Phys. **72**, 1183 (2004).

[52] C. V. Sukumar, Journal of Physics A: Mathematical and General **12**, 1715 (1979).

[53] H. N. Núñez-Yépez, E. Guillaumín-España, *et al.*, Rev. Mex. Fis. **47**, 98 (2001).

[54] I. I. Rabi, Phys. Rev. **51**, 652 (1937).

[55] C. Gerry and P. Knight, *Introductory Quantum Optics* (Cambridge University Press, 2004) p. 332.

[56] M. Hillery, R. F. O'Connell, M. O. Scully, and E. P. Wigner, Phys. Rep. **106**, 121 (1984).

[57] D. I. Bondar, R. Cabrera, *et al.*, Phys. Rev. A **88**, 052108 (2013).

[58] S.-i. Koda, J. Chem. Phys. **143**, 244110 (2015).

[59] A. Royer, Found. Phys. **22**, 727 (1992).

[60] L. E. Ballentine, Y. Yang, and J. P. Zibin, Phys. Rev. A **50**, 2854 (1994).

[61] H. Weyl, Zeitschrift fur Physik **46**, 1 (1927).

[62] W. B. Case, Am. J. Phys. **76**, 937 (2008).

[63] T. L. Curtright and C. K. Zachos, ArXiv e-prints (2011), arXiv:1104.5269 .

[64] R. Hudson, Rep. Math. Phys. **6**, 249 (1974).

[65] J. P. Dahl and M. Springborg, J. Chem. Phys. **88**, 4535 (1988).

[66] C. E. Shannon, Proc. IEEE **86**, 447 (1998).

[67] E. Hairer, S. P. Nørsett, and G. Wanner, *Solving Ordinary Differential Equations I: Nonstiff Problems* (Springer Berlin Heidelberg, 2008).

[68] S. Tomsovic and E. J. Heller, Phys. Rev. Lett. **67**, 664 (1991).

[69] M. V. Berry, Journal of Physics A: Mathematical and General **12**, 625 (1979).

[70] H. Lee and M. O. Scully, J. Chem. Phys. **77**, 4604 (1982).

[71] M. Razavy, Phys. Lett. A **212**, 119 (1996).

[72] M. Razavy, *Quantum Theory of Tunneling* (World Scientific, 2003).

[73] F. Hajir, Journal de Théorie des Nombres de Bordeaux **17**, 517 (2005).

[74] D. F. Walls and G. J. Milburn, *Quantum Optics* (Springer, 1994).

[75] I. S. Gradshteyn, I. M. Ryzhik, A. Jeffrey, and D. Zwillinger, *Table of Integrals, Series, and Products*, Table of Integrals, Series, and Products Series (Elsevier Science, 2007).

[76] M. Hofheinz, H. Wang, *et al.*, Nature **459**, 546 (2009).

[77] M. V. Berry, Proceedings of the Royal Society of London Series A **413**, 183 (1987).

[78] C. Jaffé and P. Brumer, J. Phys. Chem. **88**, 4829 (1984).

[79] C. Jaffé and P. Brumer, J. Chem. Phys. **82**, 2330 (1985).

[80] C. Jaffé, S. Kanfer, and P. Brumer, Phys. Rev. Lett. **54**, 8 (1985).

[81] J. Wilkie and P. Brumer, Phys. Rev. A **55**, 27 (1997).

[82] T. L. Chow, *Mathematical Methods for Physicists* (Cambridge University Press, 2000).

[83] M. L. Boas, *Mathematical methods in the physical sciences* (Wiley, 1983).

Index

Anharmonic potential, 51
    Inverse anharmonicity Parameter, 53
    Truncated, 51

Classical phase-space
    Current, 7
    Velocity field, 6
Classical probability distribution, 6

Dirac delta function, 72

Eckart potential, 52
Eigenenergy, 12

Hamiltonian
    Classical, 7
    Operator, 13
Hermite polynomials, 42

Jacobian, 72

Kerr Hamiltonian, 48
Kronecker delta, 72

Laguerre polynomials, 42

Momentum space potential, 14
Morse potential, 52

Normalisation constant, 20

Particle mass, 7
Phase shift, 12
Phase-space
    Closed loop, 10
    Momentum axis, 6
    Position axis, 6
Planck's constant, 11
    Rescaled, 11
Position space potential, 14
Probability current
    Momentum space, 16
    Position space, 15
Probability distribution
    Momentum, 11
    Position, 11

Quantum harmonic oscillator
    Hamiltonian, 42
    Wigner function, 42

Rabi cycle
    Hamiltonian, 17
    Period, 18
    State, 17
Rosen-Morse potential, 52

State indices, 12
Superposition
    Energy difference, 12
    Two-state, 12
      Time period, 12
      Weighting angle, 12
    Wigner distribution, 27
    Wigner distribution terms, 27
Supersymmetric quantum mechanics
    Annihilation operator, 20
    Creation operator, 20
    Superpotential, 20

Vector potential, 7

Wave function
    Momentum space, 11
    Position space, 11
Wigner current, 29
    Velocity field, 36
Wigner distribution, 24